LIU. MENGXIN Ph.D. Tuning the Core-Shell Ratio in Heterojunction Nanostructured $CuS@In_2S_3$ Nanoparticles and Photo/Electro-Catalytic Activity Evaluation. (2023)
Directed by Dr. Jianjun Wei. 133 pp.

Nanosized materials have been utilized in the areas of energy conversion and storage, heterogeneous catalysis, biomedicine, textile and more due to their advantages of tunable structures and properties. With the adoption of novel synthetic and fabrication methods, the properties of the nanoscale materials can be varied and improved by controlling the morphology (shape and size), heterojunction structures and/or crystallization, and so on. In this dissertation work, P-type copper sulfide (CuS) and N-type indium sulfide (In_2S_3) were selected to construct a hybrid heterojunction, nanostructured core-shell $CuS@In_2S_3$ nanoparticles (NPs). The hypothesis of this study is that the energy band gap can be tuned by the core-shell ratio in the synthesis, thus leading to the manipulation of the photo- and electro-catalytic activity. We used the microwave-assisted solvothermal method for the core-shell NPs fabrication. Compared with traditional chemical or electrochemical strategy, the microwave method can directly and homogeneously provide the reaction energy on the formation of particles from precursors. Basically, CuS and In_2S_3 are the members of the family of metal chalcogenide semiconductors, which have proven photo-activity and electrocatalytic activity. Different ratios of the core-shell $CuS@In_2S_3$ NPs were obtained for the photodegradation of two dye species, methylene blue (MB) and methyl orange (MO). The structural and morphological studies combining the optical bandgap analysis suggest that the CuS amount used in the synthesis plays an essential role in forming the efficient heterojunction interfaces for charge carrier separation to inhibit the recombination of excited electron and hole pairs and the resultant different optical bandgap of the NPs. The 10 wt% $CuS@In_2S_3$ core-shell NPs demonstrate a lower optical band for a wide range visible light absorption and higher photocatalytic activity than that of the CuS NPs, In_2S_3 NPs, and the 5 wt%

CuS, or 15 wt% CuS NPs. In the electrocatalytic study, electrochemistry of oxygen evolution reaction (OER) and oxygen reduction reaction (ORR) was performed using the core-shell NPs of different wt% CuS and compared to the CuS NPs and In_2S_3 NPs. The 10wt% CuS@In_2S_3 NPs demonstrated the best efficiency and kinetics in the OER and ORR process. Electrochemical impedance and Tafel analysis indicate that the 10wt% CuS@In_2S_3 NPs offer less resistance and a smaller overpotential for the reactions than any other types of NPs in this study. The mechanism analysis suggests the low energy band gap due to the optimal ratio for the heterojunction interface accounted for the improved electrocatalytic activity.

TUNING THE CORE-SHELL RATIO IN HETEROJUNCTION NANOSTRUCTURED $CuS@In_2S_3$ NANOPARTICLES AND PHOTO/ELECTRO-CATALYTIC ACTIVITY EVALUATION

by

Mengxin Liu

A Dissertation
Submitted to
the Faculty of The Graduate School at
The University of North Carolina at Greensboro
in Partial Fulfillment
of the Requirements for the Degree
Doctor of Philosophy

Greensboro

2023

Approved by

Dr. Jianjun Wei
Committee Chair

APPROVAL PAGE

This dissertation written by Mengxin Liu has been approved by the following committee of the Faculty of The Graduate School at The University of North Carolina at Greensboro.

Committee Chair

Dr. Jianjun Wei

Committee Members

Dr. Tetyana Ignatova

Dr. Eric Josephs

Dr. Lifeng Zhang

March 13, 2023

Date of Acceptance by Committee

March 13, 2023

Date of Final Oral Examination

ACKNOWLEDGEMENTS

This paper is the summarization of my Ph.D. research based on the data accumulation and analyzation in many years. Firstly, I would like to express the sincerely gratitude to my advisor Dr. Jianjun Wei for the constant and patient instruction on my study career. Most importantly, he gives me the wonderful opportunity to improve myself in the academy of Joint of Nanoscience and Nanoengineering (JSNN). In here, I received the highest motivation on my research and paper writing from him.

Besides of my advisor, I also would like to express the sincerely appreciation to my committee members, Drs. Tetyana Ignatova, Eric Josephs, and Lifeng Zhang, for their precious advice on my research. They use immense knowledge and patient help to expand my research area. My work cannot be completed without the support from them and other JSNN faculties.

During my study, I also received the best help from the lab managers Drs. Kyle Nowlin Olubunmi Ayodele, Steven Crawford, and Klinton Davis. The problems on experimental design and data collection can be solved so quickly. I also would like to appreciate Drs. Zheng Zeng, Alex Sheardy, Kokougan Allado, Wendi Zhang, Zuowei Ji, Ziyu Yin, Anitha Jayapalan, Frank Tukur, Matthew Hawkins, and many others, for their valued guidance.

TABLE OF CONTENTS

LIST OF TABLES

LIST OF FIGURES

CHAPTER I: INTRODUCTION

Our environmental are facing serious problems such as air, soil, noise, and light pollution. The primary contaminant resource can be categorized into over combustion of traditional fossil fuel, excessive wastewater discharging, and improper consumption of natural resources (Tainio et al., 2021) (Ibrahim et al., 2020). According to recent report, millions of people are impacted by the over exhausting of nitric monoxide, nitric dioxide, carbon dioxide, and sulfur oxide etc.; and most of the pollution is conducted by the daily utilized transportation tools such as automobiles and planes (S. Khan et al., 2021). In that case, the traditional transportation carriers have been being gradually replaced by the electrical or hybrid vehicles. Simultaneously, the amount of utilization on renewable energy storage system, such as battery and supercapacitor, has been increased since last two decades (X. Zeng et al., 2019) (L. Zhang et al., 2018). For the aqueous system around our living circumstance, pollution is also serious. For example, over 10000 types of artificial dyes are fabricated, and more than 0.2 million tons of the untreated dyes waste are released into the environment every year (Al-Mamun et al., 2019). The pollutions have already render tons of negative effects to human beings, other animals, and plants. Especially, the pollutants can direct cause body issues such as coughing, skin infection, irritation, irreversible heart/lungs damages, and serious cancer etc. (González-Martín et al., 2021). To solve the problem, several types of nanosized materials have been advocated for energy conversion/storage, dyes' photodegradation, sensing, and photothermal therapy.

In this research, CuS, In_2S_3, and their 'core-shell' assembled NPs have been studied based on their photocatalytic and electrocatalytic performance. The fabricated materials belong to the family of metal chalcogenide.

Basically, Metal chalcogenide NPs have been regarded as promising candidate on photocatalyst based indirect chemical organic/inorganic contaminant elimination because of the outstanding properties of superior light sensitivity, high chemical/physical stability, environmentally friendly, and low cost (Gupta et al., 2012) (W. Li et al., 2018). The most commonly used NPs under the research area of photocatalysis, photothermal therapy, rechargeable battery, and supercapacitor are the CdS, ZnS, WS_2, MoS_2, CuS, and In_2S_3 (Hao & Lang, 2019).

In the last decade, CuS has been well studied in the area of photocatalytic degradation (Gupta et al., 2012) (Chaki et al., 2014). CuS has relatively lower bandgap energy, approximately 2.5 eV, which gives the material excellent solar spectrum sensitivity and high capacity on visible light harvesting (Nwaji & Akinoglu, 2021). Furthermore, nanostructured CuS has an unique size and morphology dependent quantum structure; so, its optical performance can be tuned based on the diversity of fabrication method and synthetic parameters (H. T. Zhang et al., 2006).

As similar as In_2S_3, it also has the characteristics of low toxicity, low cost, but high chemical stability (Alhammadi et al., 2021) (Huoshuai Huang et al., 2021). Compared to CuS, The bandgap energy (~2.0 eV) give the material relatively higher solar energy sensitivity (W. Gao et al., 2015). So, this material is also commonly utilized in photovoltaic and optoelectronic regions.

For the fabrication strategy of the metal chalcogenide NPs, hydrothermal and solvothermal are popular methods because of their low-cost, easy handling, and high producibility (Ndlwana et al., 2021). Basically, the most distinguishable character between the two strategies is whether purified water participate in the reaction or not (Devaraju & Honma, 2012). Under the fabrication time, precursors blend homogenously and react with each other in a regular beaker or 3-necks flask with relatively lower temperature (200°C, approximately) (F. Li et al., 2009). Size and morphology

are highly determined by the ratio of precursors, reaction time, and sintering temperature. The metal (Zn, Mo, Cu, or In, etc.) source normally derives from its regular salt or complex compounds. Metal chloride, nitride trihydrate, dithiooxamide, or salicylate etc. can be utilized as precursors under the reaction (Balakrishnan et al., 2021). Furthermore, thiourea, thioacetamide, hydrogen sulfide, sodium sulfide, and high purity sulfur powder can be used for S source (Balakrishnan et al., 2021). Besides of the two common fabrication strategies, aerosol and solution method have also been preferred by researchers (Shamraiz et al., 2016) (Meyer et al., 2019). For aerosol treatment, fine solid particles and gas phase sulfur contained precursor react with each other under high temperature (above 400°C). Because of the relative high temperature treatment, impurities and undesired byproducts can be gasified under the preheating treatment. On the contrary, solution method is usually implemented under relatively lower temperature, which is around 100°C (Varma et al., 2016). This method has been commonly used for the formation of metal oxides, sulfides, alloys, or multi-elements doped semiconductors. Besides of the traditional methods, microwave assisted hydrothermal/solvothermal treatment is one of the most straight-forward way for low-dimensional nanoparticles' fabrication (Sheardy et al., 2020a) (L. Wang, 2016). Similarly, critical factors, such as ratios of precursors, sintering temperature and annealing time, etc. determine the size and morphologies' distribution (Sheardy et al., 2020a).

For the utilization on indirect chemical defined photodegradation, both CuS and In_2S_3 can be confronted of the same challenges. For example, rapidly charge carriers' recombination, low light harvesting capacity, and photo-corrosion from self-oxidation of S anion. To solve these thorny problems, some tactics have been created by scholars, which include the formation of hieratical monologies, assemble of carbonaceous substrates, and hybridization of heterostructures, etc.

Some efforts had been completed to improve the photocatalytic efficiency and reusability of the metal sulfides based on the aforementioned method. For instance, visible light sensitivity of bare CuS can be enhanced after special chemical treatment. Ain et al. has provided the first report on visible light driven CuS NPs photocatalytic decomposition on congo red dye (Ain et al., 2020). In the publication, copper(II) dithiocarbamate had been formed initially for Cu and S source. After thermal decomposition into octylamine solution, nanoparticle formed with a hexagonal crystalline phase. In the optical behavior studies, the UV-visible spectra showed a 406 nm centered broad absorption peak. Simultaneously, bandgap energy of the CuS was approved around 2.1 eV by Tauc's theory. Under the test of dyes' photodecomposition, 100 mL, 100 mg/L different dye (azo, naphthalene, and phenyl) solution can be totally degraded by 50 mg synthesized photocatalyst in 40 mins.

Dopants' hybridization is a highly recommended strategy on photocatalytic activity enhancement. The smaller or bigger exotic atom can modify the original crystal lattice, which composition cause surface area expanding with increasing of the number of active sites (Gharaei et al., 2018). Kao et al. synthesized the CuO-CuS core-shell nanowire by an oxidization and sulfurization treatment on Cu foil (Kao et al., 2019). Firstly, CuO was formed by thermal oxidation of Cu under 550 °C, then the sulfurization was implemented by the S powder annealing under 300 °C. CuS covered on the CuO surface homogenously with the thickness of 10 nm, approximately. Under the synergetic effect of the CuS and CuO, the degradation activity was enhanced. In addition, Yoo et al. inserted the hierarchical CuS into the spherical CuO structure by a direct chemical conversion (Yoo et al., 2020). Firstly, $Cu(NO_3)_2 \bullet 3H_2O$ was chose as CuO precursor. The pyrolysis process was done under condensed O_2 environment to form a CuO configuration. Then, CuS facet interplanted into the CuO particle by a partial chemical conversion on the synthesized

CuO with the participation of thiourea (S precursor). In the paper, molar ratio of CuO to S precursor was set as 0.25:1, 0.50:1, and 0.75:1 for structural optimization. Basically, the chemical transition with thiourea did not destroy the original microstructure of CuO. Under the sample of 0.50:1 and 0.75:1, the homogeneous wrinkle structure was created after 12 hours; and the 0.50:1 has the most optimized hexagonal CuS and monoclinic CuO distribution. After 24 hours' chemical conversion, CuS facet structure was successfully located at the inside and outside of the CuO host. According to the photocatalysis test, 200 mL rhodamine B solution with the molarity of 2.0×10^{-5} M can be totally degraded under the optimized sample under 15 min, and the efficiency was as high as 95% after five cycles. The outstanding photocatalytic activity and reusability is contributed to the enlarged surface area by the introduction of hieratical heterostructure and the improved visible light driven ability from the refinement of the bandgap structure.

Other transition metal oxides, such as ZnO, WO_3, NiO, and Fe_2O_3 etc., have also been preferred and used as heterojunction dopants for photocatalytic performance improvement (Hong et al., 2016) (Basu et al., 2014) (C. Song et al., 2017) (Vempuluru et al., 2021) (Y. Huang et al., 2020). According to current study, crystal structures' differences between the dopants and host may cause the interphase mismatching, which often leads to quick recombination of charge carrier pairs (Isac et al., 2020). To solve the problem, Luminita et al. used spray pyrolysis deposition strategy to fabricate the CuS/ZnO/TiO_2 sandwiched configuration (Isac et al., 2020). Corresponding metal salts, such as $TiCl_4$, $ZnCl_2$, and $CuCl_2$, were selected as precursors. The stabilizing and annealing temperature for layers' deposition were set from 250 to 500 °C, which depends on the thermal energy's requirement of different panels. Especially, porous ZnO structure can be created by the utilization of acetilacetonate (AcAc). Based on the XRD patterns and AFM

images, AcAc can decrease the crystal growing rate, which create enough space for the propagation of porous structure.

Furthermore, metal element for dopants with higher or lower oxidation states can trap photon induced hole or electrons to inhibit the quickly charge carrier recombination rate as well as improve the electrical conductivity (Hengming Huang et al., 2017) (Saqib et al., 2016) (Khlyustova et al., 2020). Chen et al. introduced a Ca doped β-In_2S_3 through a facile one-pot hydrothermal strategy (Y. F. Chen et al., 2021). According to the synthesis method, $In(NO_3)_3 \cdot 4H_2O$ and thioacetamide were chose for In and S precursor, correspondingly. The heating process was completed with/without the addition of $Ca(NO_3)_2 \cdot 4H_2O$ which was used as Ca atoms' introduction. Comparing the photodegradation efficiency with undoped β-In_2S_3 particles, the decorated In_2S_3 displayed an obvious efficiency increment, in which almost 95% of 150 mL MO solution with density of 10 mg/L can be decomposed by 30 mg synthesized NPs, and the value of the undoped In_2S_3 is 80%, approximately. Moreover, the bandgap energy was narrowed by Ca decoration which increase the light sensitivity directly.

Noble metal can be promising candidate on interphases' insertion. Fermi level modification by nanosized noble metal retard the quick recombination of electron-hole pairs because charge carriers can transfer to the Fermi level of the metal rather than directly drop back to the valance band of metal sulfides (Zhan et al., 2014) (Byeon & Kim, 2014). On the other hand, noble metals, such as Au and Ag, have plasmonic scattering property under the irradiation of visible light (Byeon & Kim, 2014). In this case, noble metal can not only expand the visible light absorption range, but also accelerate the degradation rate by the injection of the scattered electron into adjacent metal sulfide particles (Zhan et al., 2014) (Q. Chen et al., 2016).

Additionally, graphene based heterojunction can also improve the visible light sensitivity and photocatalytic activity on CuS or other metal sulfides (H. B. Huang et al., 2018). Fundamentally, graphene has an atomic scaled single layer graphite structure, and the compound possess outstanding physical properties, such as high concentration of charge carriers (~10^{13} /cm), high electron mobility (around 3×10^5 $cm^2/V\bullet s$), electrical conductivity (~10^8 A/cm^2), and thermal conductivity (~5000 W/m•K, at room temperature) etc. (P. Singh et al., 2020) (Yu et al., 2019) (Hossain et al., 2020) (B. Wang et al., 2019). Due to the two-dimensional hexagonal crystallization, graphene based carbonaceous material also has larger surface area (~2600 m^2/g) than regular active carbon and carbon nanotube (Hossain et al., 2020). Moreover, functional groups, such as hydroxyl, carbonyl, and/or carboxyl etc., can be anchored on basal and edge panel by different additives during synthesis (Hossain et al., 2020) (B. Wang et al., 2019). The functional radicals create sufficient area for immobilization of exotic metal, metal oxide, or metal sulfide etc. However, without the participation of the metal sulfides or other types of photocatalyst, bare graphene does not have obvious photocatalytic activity. Chen and other colleges invented a graphene decorated In_2S_3 heterostructure via graphene induced phase transition hydrothermal method (L. Chen et al., 2022). Based on the unique strategy, active number of sites and surface area were increased after the transformation from 3-dimential heterojunction to a special 2-diemtnial configuration. The hybridized photocatalyst not only had high efficiency on the rhodamine B photodegradation, but also high capacity on benzene alcohol photodecomposition and Cr(VI) heavy metal transformation.

As it mentioned before, rechargeable battery systems have been widely utilized in different areas. In that case, the performance of electrocatalyst on OER and ORR can be essential factor on metal-air rechargeable battery (MABs) and fuel cells (FCs). As a promising energy

storage device, MABs has the specific capacity which can be 3 to 5 times' larger than traditional lithium-ion battery (LIBs) (Yanguang Li & Lu, 2017). Pure metal such as Li, Na, K, Zn, Fe, or Al etc. installed on anode side without serious microstructural deterioration. During the discharging or charging state of MABs, oxidation and reduction of metal anode is coupling with O_2 redox reaction (**Figure 1.1a**). And the cathode of the MABs is usually composed by the air diffusion membrane and a proper catalytic layer. Because of the sluggish charge transferring of OER and ORR, power density can cyclability of MABs are also unsatisfied. Similarly, FCs is a another type of 'green' energy conversion system because the byproduct is only H_2O with heat releasing after the reaction between H_2 'fuel' and O_2 (**Figure 1.1b**) (Kheirandish et al., 2014). Currently, the working efficiency is approximately 40% to 60%, which is obvious higher than performance of traditional gas and diesel engine (Kheirandish et al., 2014) (Kirubakaran et al., 2009). However, the electrocatalytic characteristics of the catalyst which used on cathode of FCs plays a crucial role in the performance of the renewable energy storage system (S. Wang et al., 2021).

In this research, we are trying to provide a novel solvothermal method for the fabrication of CuS, In_2S_3, and their core-shell configurations. Rather than the application of traditional heating source, microwave associated reduced energy and time consumption method was implemented on the NPs' formation. The synthesized core-shell structure not only effectively inhibited the quickly charge carrier pairs combination by the formed staggered quantum structure, but also obviously reduce the bandgap energy of single NPs. Furthermore, the homogenous cover shell structure can also protect the core NPs from deterioration under harsh environment to increase the recyclability of the photocatalyst. In Chapter II, CuS, In_2S_3, and the stable core-shell structure was synthesized and characterized. The crystal structure, morphology, elemental character, and optical behavior

was examinate by different microscopy and spectroscopy techniques. In Chapter III, the photodegradation performance of different types of NPs was tested under the MB and MO aqueous solution. Because of optimized bandgap energy and modified quantum structure, the 10 wt% CuS@In_2S_3 sample displayed a highest photocatalytic activity and kinetics, in which MB dye (20 mg/L) can be totally decomposed within 30 mins. In Chapter IV, electrocatalytic performance of the synthesized NPs was also detected on OER and ORR tests under a widely used 3-electrodes testing system with a utilization of rotating disk electrode (RDE) as working electrode. It was discovered that the optimized bandgap energy by the core-shell assembled configuration also had a determined effect on the electrocatalytic performances. However, stronger semiconductor behavior quenched the catalytic activity and electron transfer kinetics, which provided the large space for the improvement on activity. In Chapter V, a 2-electrode OER system was built to explore OER electrocatalytic performance of a α-MnO_2 electrodeposited super-aligned carbon nano fiber (MnO_2@SA-CNFs) with the influence of external magnetic field. We found that the super-aligned carbon nano fiber (SA-CNF) backbone can not only supply a high conductive intermediate but also be used as strong supporting substrate for the electrodeposition of α-MnO_2. Additionally, with the increment of electrodeposited time, more homogenous α-MnO_2 particles were anchored on the surface of SA-CNFs. Under the OER test, more obvious variation on current can be detected in longer time electrodeposited sample with the application of external magnetic field.

Figure 1.1. Schematic structure of MABs (a) and FCs (b).

a.

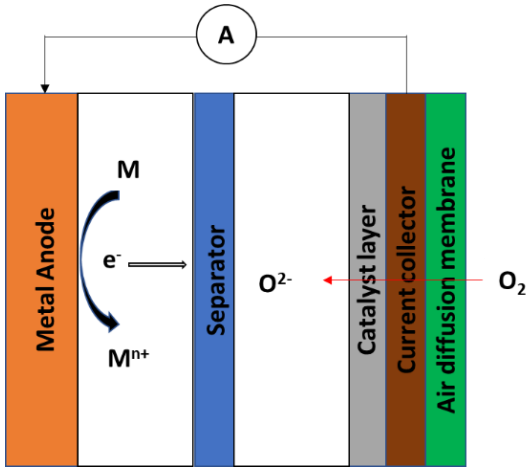

b.

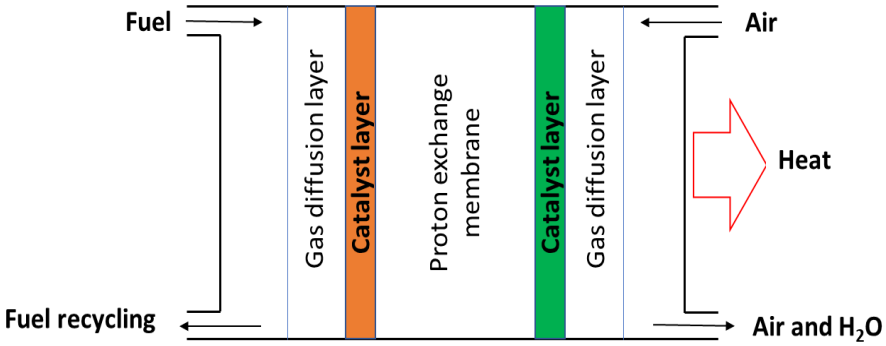

CHAPTER II CHARACTRIZATION OF THE MICROWAVE SYNTHESIZED COPPER SULFIDE, INDIUM SULFIDE AND THE CORE-SHELL INSTALLATION

This chapter has been published as M. Liu, A. Sheardy, G. Pathiraja, F. Tukur, A. Jayapalan, J. Wei. Tuning the Core-Shell Ratio in Nanostructured CuS@In_2S_3 Photocatalyst for Efficient Dye Degradation. Cleaner Chemical Engineering (2023).

Introduction

CuS is one of the members in the Cu_xS family, in which the x value can be 1, 1.39, 1.75, 1.8, or 2, corresponding with the crystal structure of covellite, spionkopite, anilite, digenite, and chalcocite (Morales-García et al., 2014). The atomic arrangement of covellite CuS belongs to P6_3/mmc space group which triangle CuS_3 and tetrahedron CuS_4 are connected by the sharing of S atom, and two adjacent CuS_4 structure are connected by S-S layer (see **Figure 2.1a**) (Gharaei et al., 2018). The material is widely utilized in supercapacitors, photovoltaic devices, biosensors, lithium-ion batteries, and photocatalysis. The covellite CuS has high morphology diversity. Common shapes are the nanorod, nanowire, nanodot, nanosphere, and nanoflake; and, optical behaviors, structural characters, even size distribution are morphology dependent. With the association of fabrication strategies, CuS has wide range of absorption spectrum which is from UV to NIR region. In addition, the material has an obvious red emission band at 460 nm (Sheardy et al., 2020b) (Shamraiz et al., 2016) (Iqbal, Bahadur, Anwer, Ali, et al., 2020).

For fabrication, the common strategies are based on hydrothermal and solvothermal treatment (Shamraiz et al., 2016). The primary difference of these two methods is whether H2O is participated into the reaction or not. Physical and chemical properties can be determined by concentration of precursors, annealing temperature, reaction time, and pressure. For example, in the research of Sandhya et al., the S precursor of CH_4N_2S and $Na_2S_2O_3$ are reacted with different

types of Cu source under hydrothermal treatment (Yadav et al., 2019). However, under the combination of $Cu(NO_3)_2•3H_2O$ - CH_4N_2S, $CuSO_4•5H_2O$ - CH_4N_2S, $Cu(NO_3)_2•3H2O$ - $Na_2S_2O_3$, and $CuSO_4•5H_2O$ - $Na_2S_2O_3$, the morphology of the particle displayed into nanorod, nanoflake, nanodot, and nanoball, respectively; in which the corresponding particle size are 11.90, 2.80, 19.45, and 20.10 nm with the bandgap energy of 1.81, 1.93, 2.10, and 1.88 eV.

However, bare CuS NPs has stacking phenomenon, and the aggregation behavior can directly decrease the number of active site and surface area (Qian et al., 2014) (El-Hout et al., 2020). Especially, S anion of CuS can be easily oxidized by the photon induced holes under the photodegradation process. In addition, like of other narrow bandgap metal sulfide, the rapid charge carriers' recombination rate decrements the photocatalytic efficiency also (J. Li et al., 2017). To solve the problem, surface modification by heterogenous hybridization is the most common way to compensate the shortcomings of single CuS (Iqbal, Bahadur, Anwer, Shoaib, et al., 2020). Other metal chalcogenide, metal oxides, and/or carbonaceous substrate can be used as heterojunctions. For example, Piu et al. fabricated a ZnS hybridized CuS photocatalyst with the decoration of graphene nanosheet (Das et al., 2021). For synthesis, $CuSO_4$, $ZnSO_4$, and green tea leaf were organized as Cu, Zn, and graphene precursor with the participation of solvothermal treatment. For the optimized sample, dye's degradation efficiency can reach to 90.21% after 100 minutes. After 5th cycle, the efficiency also was kept into 68.38%. According to the analysis, expanded surface of graphene sheet can effectively inhibit the agglomeration of the chalcogenide particles. In the research of Cui et al., a $CuWO_4$/CuS heterojunction was formed under different molar ratio (from 4:1 to 1:4) by one step hydrothermal method (Y. Cui et al., 2022). By the treatment of the 1:1 sample, 93.2 % of the 100 mL (15 mg/L) rhodamine B dye can be degraded under the visible light (420 nm) irradiation. The reinforced performance of the representative

catalyst was contributed to the increased surface area, enhanced electron-hole recombination time, and light absorbability.

Similarly, In_2S_3 is also a widely utilized photovoltaic and optoelectrical material (Pistor et al., 2016). The crystal structure of the β type In_2S_3 is displayed in **Figure 2.1b**. In general, In_2S_3 has the property of low toxicity but wide range of visible light absorption. The direct bandgap energy is 2.0 eV, approximately, which quantum property make the semiconductor a promising catalyst in visible light drive contamination degradation and photoelectrochemical water splitting reaction (Conesa, 2022) (J. Singh & Soni, 2021). The material also has various morphologies such as nanotube, nanorod, urchin like, or hollow sphere structure etc. based on synthesis methods (S. Yang et al., 2017). Compared with other metal sulfides, In_2S_3 has much higher photocorrosion resistance than CdS (L. Wei et al., 2021) (Yujie Li et al., 2017). As same as In_2S_3, ZnS also has a high photocorrosion resistance, but the bandgap is too wider to harvest energy from visible light (X. Liu et al., 2021). Even though MoS_2 is also considered as high performance photocatalyst for water purification or H_2 evolution, however, serious stacking of the NPs cannot be avoided (W. Sheng et al., 2018).

In this chapter, a CuS@In_2S_3 core-shell structure was fabricated. The core-shell installation can directly optimize the charge diffusion path, specific area, and the exposure active side of the NPs. Crystallinity, morphology, elemental distribution, oxidation state of elements, microstructure, and optical behaviors will be studied based on the influence of core material.

Figure 2.1a. Crystal structure of CuS (Gharaei et al., 2018); **b.** crystal structure of β-In_2S_3 (Z. Zhao et al., 2012).

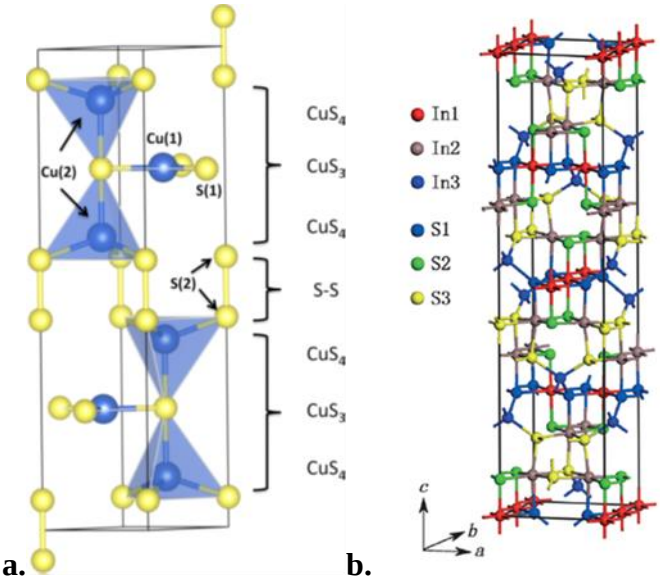

a. **b.**

Experimental

Material and agent

Copper acetylacetonate ($Cu(acac)_2$, Acros Organics, 99.9%), sulfur powder (S, Alfa Aesar, 99.9%), oleylamine (OLA, Aldrich, 70%), sodium dodecyl sulfate (SDS, Sigma-Aldrich, >98.5%), indium acetate (99.9%, Alfa Aesar), 1-octadecene (ODE, Alfa Aesar, >90%), tert-dodecanethiol (t-DDT, TGI, >98%), absolute ethanol (Sigma-Aldrich, 99.5%), toluene (Fisher scientific, 99.5%), methylene blue (MB, Fisher scientific, 85%) methyl orange (MO, sigma-Aldrich, 85%) were used without further purification.CuS NPs synthesis:

CuS NPs fabrication

The synthesis of CuS NPs was based on a method in our previous report (Sheardy et al., 2020b). In brief, 10 mL oleylamine (OLA, 70%) was added in a flask with pre-warming up at 40°C for 10 minutes. Then 33 mg (0.125mmol) $Cu(acac)_2$ and 4 mg (0.125mol) S were mixed

with the OLA. A microwave reactor (CEM Discover) was used as thermal energy source. Before the electromagnetic source turned on, a vacuum pump was running for 10 minutes before to purge N_2 stream for 2 minutes. This vacuum-N_2 purging operation was implemented to the grease sealed reactor 3 times. In the end, the reactor was filled with N_2. The blended precursors were under reaction for 5 minutes at the power 150 W and temperature 72 °C. The reactor was turned off and the reaction was stopped by adding 20 mL absolute ethanol. The obtained NP product was cleaned by a mixture of 10 mL absolute ethanol and 10 mL toluene for 3 times followed with centrifugation at 10000 rpm for 10 minutes. The final CuS NPs was dispersed into 5 mL toluene homogenously.

In_2S_3 NPs synthesis

The In_2S_3 NPs were synthesized in the same microwave reactor. The precursor solution was prepared by mixing 36.5 mg (0.125mmol) indium acetate with 5 mL OLA (70%), 5 mL ODE, and 2 mL t-DDT to get a homogeneous solution. The synthetic reaction was performed under N_2 circumstance at power 300 W, temperature 185 °C for 20 minutes then stopped. After the reactor flask cooled down to room temperature, the reaction was terminated by adding 20 mL absolute ethanol, followed by centrifugation at 10000 rpm for10 minutes. The obtained In_2S_3 NPs were dispersed and cleaned by a mixture of 10 mL absolute ethanol and 10 mL toluene, followed by the 10000 rpm 10 minutes' centrifugation. The cleaning process was operated 3 times. The final product (~80 mg) was dispersed and stored in 5 mL toluene.

Core-shell installation

In order to synthesize the core/shell NPs and improve their stability, functional radicals i.e., hydroxyl, carboxyl and/or carbonyl, were cultivated on the surface of CuS NPs as a high effective binder for the In_2S_3 shell formation (Hofmann et al., 2019). SDS was dissolved into

absolute ethanol at 10 mg/mL. Then a 2 mL of the SDS solution was added into the 5 mL CuS NPs-toluene solution and mixed. After 10 minutes, the cultivated CuS NPs were extracted by the rotary evaporator (IKA Rotary evaporator RV 8V) and re-dispersed into 5 mL toluene.

The same reaction condition of In_2S_3 NPs synthesis was used for shell formation at the surface CuS NPs. The cultivated CuS NPs were added into the same volume precursor solution for the In_2S_3 NPs. Three types of core-shell NPs were obtained with different dosages of 4 mg, 8 mg, and 12 mg of the cultivated CuS NPs in reaction, corresponding to 5%, 10% and 15% (wt.) of CuS to In_2S_3 NPs, respectively.

Materials' characterization

Optical properties of the NPs were detected by the UV-visible spectrometer (UV-vis spectroscopy, Varian Cary 6000i) and photoluminescence spectrometer (Horiba Fluoromax-4C). X-ray diffraction (XRD, Agilent Germini) was utilized to detect crystallinity of the materials. Field-emission scanning electron microscopy (FESEM, Carl Zeiss Auriga Microscope) was used for imaging morphology; Energy dispersive X-ray spectroscopy (EDX, Hitachi S-4800-I) and X-ray photoelectron spectroscopy (XPS, Thermo Scientific Escalab) were applied for structural analysis. Transmission electron microscopy (TEM, 2100 Plus, JEOL) and high-resolution TEM (HRTEM) with selected area electron diffraction (SAED) analysis were used for imaging the details of the synthesized NPs. The surface charge was evaluated by a zeta potential test station (Malvern ZEN3600 Zetasizer). Fourier transform infrared spectroscopy (FTIR, Shimadzu IRAffinity-1) was utilized for the dye degradation analysis study.

Result and Discussion

Microwave-assisted synthesis in this work provide a simple and effective approach to obtain heterojunction nanostructures. In **Table A. S2.1**, we compared the reported hydrothermal methods using In_2S_3 as one component for heterostructure nanomaterials. Mostly they need a few hours to a day to generate the products. As a contrast, we were able to generate the CuS@In_2S_3 hy-NPs less than 40 min according to the procedure described in experimental section. In this study, five NPs, i.e., the CuS or In_2S_3 NPs and the CuS@In_2S_3 core-shell Hy-NPs of 5wt%, 10wt, and 15wt% CuS were obtained. The structural, morphological, and optical properties were characterized by a variety of spectroscopic and microscopic means.

The XRD diffraction patterns of pristine In_2S_3, CuS, and 'core-shell' NPs are displayed in **Figure 2.2a**. According to the profile of somewhat broad diffraction peaks, it implies that these NPs are not well crystalized. The crystallization may be attributed to the relatively lower reaction temperature and sintering time (An et al., 2017) (H. T. Zhang et al., 2006) (Horani & Lifshitz, 2019). For the pure In_2S_3, XRD profile displays a mixture of β tetragonal and γ trigonal phases. Diffraction angles at the 2Θ of 27.64°, 28.44°, 33.28°, 41.08°, 43.38°, 47.97°, 85.32° and 98.41° represent the (109), (206), (00$\underline{1}$2), (20$\underline{1}$2), (309), (22$\underline{1}$2), (549), and (00$\underline{3}$2) crystal planes of tetragonal crystallization. The angles at 27.26° and 48.50° indicate the (110) and (300) planes of the γ phase respectively (Horani & Lifshitz, 2019). Additionally, the (22$\underline{1}$2) plane of the β-In_2S_3 has the highest crystallization level. The XRD spectrum of the CuS NPs shows diffraction peaks at 27.12°, 28.90°, 34.57°, 41.36°, 45.77°, 47.68°, 63.24°, 87.89°, and 98.50°, which match with the hexagonal phase dominated with (101), (102), (006), (105), (110), (107), (205), (2-1$\underline{1}$2), and (306) covellite CuS planes (An et al., 2017) (H. T. Zhang et al., 2006).

Figure 2.2b shows the XRD spectra of three core-shell NPs of different wt% CuS NPs in synthesis. Interface interaction between the core and the shell materials was detected. The (206) and (309) planes of β-In_2S_3 became more ambiguous with the higher wt% of CuS. While the intensity of the (107) plane for the hexagonal CuS phase tends to more profound with higher wt% core CuS.

Willimson-Hall (W-H) theory was utilized to calculate the average crystalline size of the NPs with equations as follows (Emil & Gürmen, 2018).

$$L = \frac{k\lambda}{(FWHM)\cos\theta} \quad (2.1)$$

$$n\lambda = 2d\sin\theta \quad (2.2)$$

where the k, λ, Θ, and L are sharp factor (0.94), wavelength of the X-ray source (1.5418Å), peak position, and the calculated crystalline size, respectively. The full width of half maximum (FWHM) of the highest crystallinity plane was fitted by Lorentzian function (Prabhu et al., 2014) (Scardi, 2020). The calculated average crystalline size of 10% (wt CuS), is 6.27 nm. The interplanar distances of the characteristic planes of the β-In_2S_3 (22$\underline{12}$) and CuS (107) were calculated by Braggs' law (Eq. 2.2), in which n, λ, Θ, and d are the diffraction order (at n=1), wavelength of the incident radiation (λ=1.5418 Å), angle of scattering, and the interplanar distance (Mayonado et al., 2015). The interplanar distance values are 1.89 and 1.91 Å for the featured β-In_2S_3 (22$\underline{12}$) and CuS (107), respectively. Additional interplanar distances of the identified planes were obtained and displayed in **Table A. S2.2.**

Figure 2.2a. XRD patterns of CuS and In_2S_3 NPs; **b.** core-shell CuS@In_2S_3 NPs with different dosage of CuS (wt%) in synthesis.

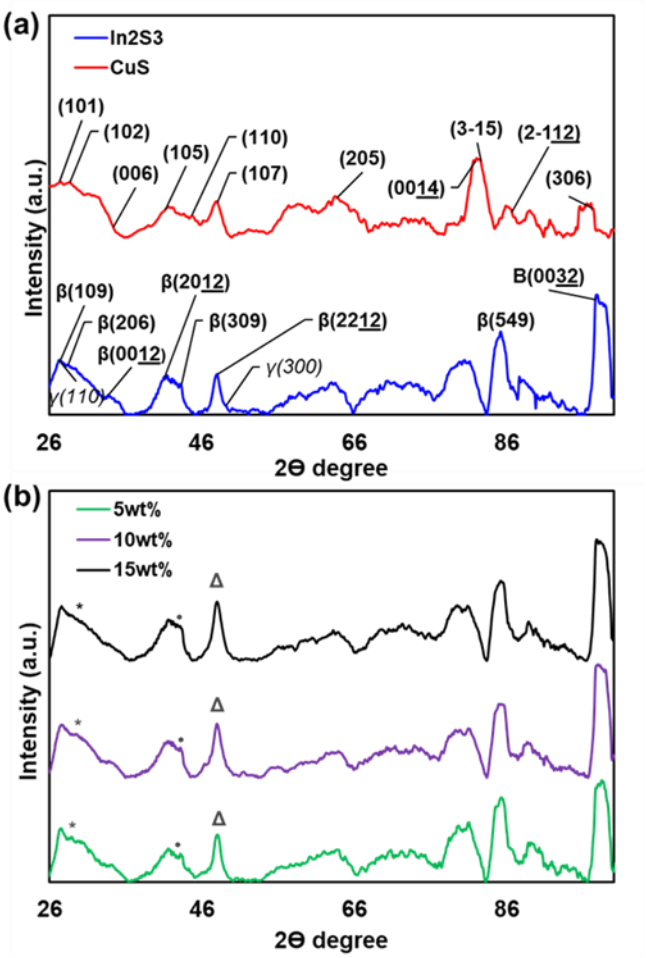

Figure 2.3 displays SEM images of the NPs at 30 kX magnification. The pristine In_2S_3 NPs show flower petal distribution and the CuS NPs display agglomerated dots. The shape of core-shell CuS@In_2S_3 NPs varies from scattered flower petal to loosen flake, with increasing of the wt% CuS. It is observed that more spherical particles randomly dispersed at the surface of the flakes with more wt% CuS in the synthesis.

Elementary analysis was implemented by EDX. Both the spectral and elemental mapping results are shown in **Figure A. S2.1**. Main atomic percentage of primary elements of the NPs

were summarized in **Table 2.1**. For the In_2S_3 NPs, the atomic ratio of In to S is approximately 2:3, confirming the expected stoichiometry composition. Similarly, atomic ratio of Cu to S in the CuS NPs almost equals to 1. In core-shell hybridization, the atomic percentage of Cu increases with more addition of CuS NPs in synthesis. The secondary elements, such as C, N, and O, were found presence in the EDX elementary spectra. This is expected due to the introduction of the surface capping agents, i.e., OLA, ODE, acetylacetonate, and their residues could attach to the NPs. The high intensity of the Si signal was contributed by the background of sample holders. The homogenous element mapping at the whole area of NPs demonstrates the uniform distribution of elements S, In, and/or Cu.

Table 2.1. Elemental composition of the NPs from EDX data (Atomic %).

Samples	**In at. %**	**Cu at. %**	**S at. %**
Pristine In_2S_3	6.45	-	10.29
5wt% CuS	5.97	0.81	9.46
10wt% CuS	6.42	1.44	10.46
15wt% CuS	6.04	1.71	10.12
Pristine CuS	-	4.54	4.78

Figure 2.3a. SEM image (30 kX) of In_2S_3 NPs; **b.** CuS NPs; **c.** 5wt% CuS@In_2S_3 NPs; **d.** 10wt% CuS@In_2S_3 NPs; **e.** 15wt% CuS@In_2S_3 NPs NPs.

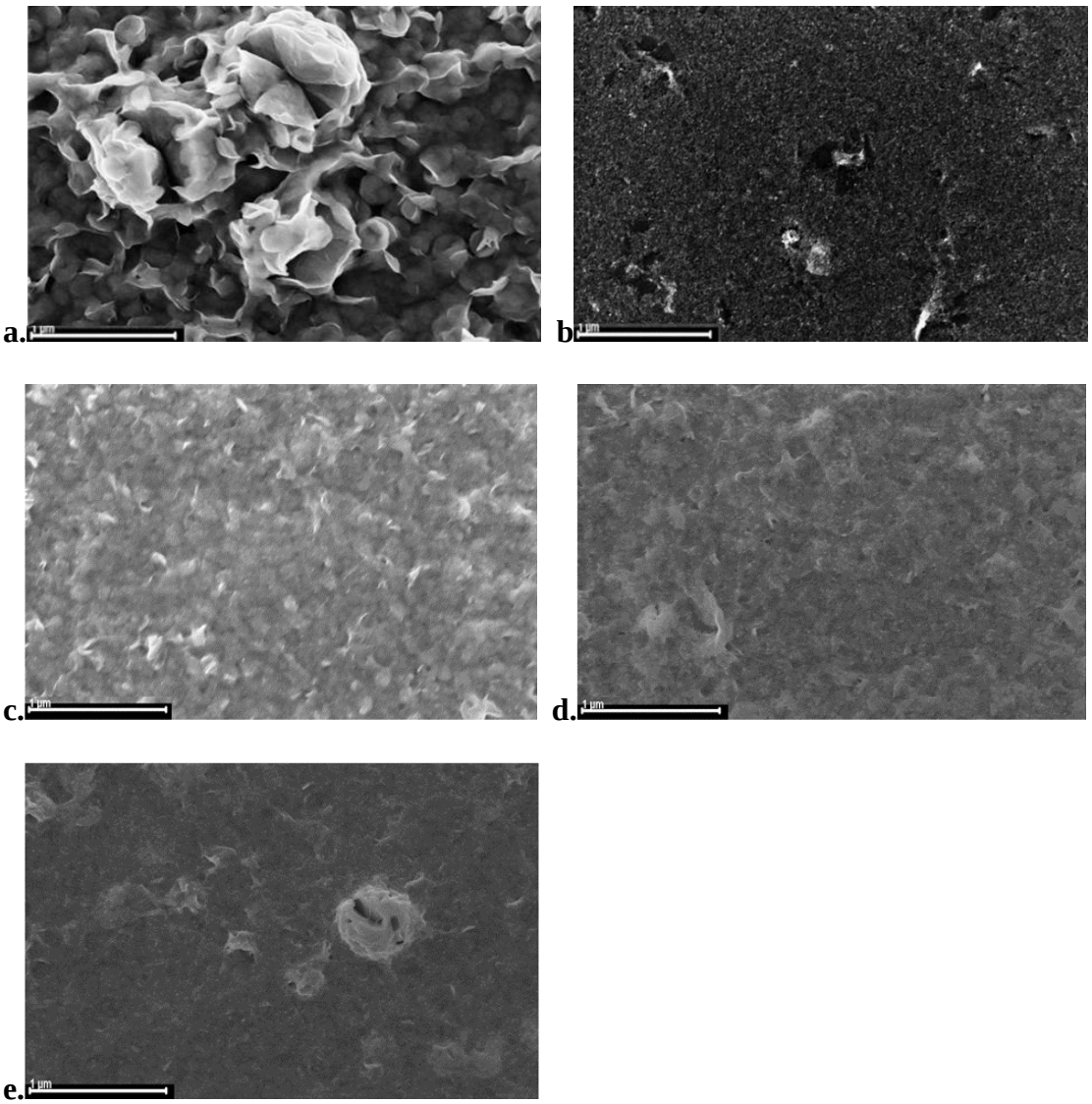

The compositions of NPs were further examined by XPS and the resultant XPS spectra are presented in **Figure A. S2.2** & **S2.3**. The representative deconvoluted XPS spectra of the 10wt% CuS core-shell NPs were shown in **Figure 2.4**. The deconvoluted spectra in **Figure 2.4a** and **Figure A. S2.3a** present clearly the In^{3+} $3d_{5/2}$ (444.17eV) and $In^{3+}3d_{3/2}$ (451.70eV) spin orbitals (B. Chen et al., 2015) (Perera et al., 2015). The spectra of CuS and the core-shell NPs

(see **Figure 2.4b** and **Figure A. S2.3b**) indicate Cu^{2+} $2p_{3/2}$ and Cu^{2+} $2p_{1/2}$ spin structures with corresponding binding energy at 934.68 and 954.30 eV. The CuS NPs alone show the highest intensity Cu 2P peaks with coexistence of the weak satellite peaks at 941.74 and 961.61 eV, while the Cu 2p signal in core-shell NPs becomes weaker because of the lower weight ratio of CuS and the coverage of In_2S_3 shell (Deng et al., 2017). **Figure 2.4c** and **Figure A. S2.3c** spectra exhibit the S 2p splitting orbitals of the $2p_{3/2}$ (161.19eV) and $2p_{1/2}$ (162.35eV) binding energies which indicate the presence of S^{2-} anions in sulfide compound (Jiqian Yang et al., 2017a). The deconvoluted peaks also display a S 2p splitting orbital at 168.06 and 169.31eV with lower intensity. These extra coupled peaks suggest the small amount of oxygen contained sulfonate and/or sulfinate by-products (Jiqian Yang et al., 2017b) (Amato et al., 2008). Furthermore, elements C, O, and N can be found in the XPS spectra, providing evidence of the formation of surface organic ligands. **Figure 2.4d** is the deconvoluted C1s peaks at 284.15, 284.69, and 285.85eV, matching with the characteristics of C in graphitic, aliphatic, and C-O-H configurations (S. Y. Lee & Mahajan, 2021) (El Habnouni et al., 2011). **Figure 2.4e** and **2.4f** present the binding spectra of O 1s and N 1s, respectively. The O 1s peak at 531.8eV represents the property of hydroxyl oxygen (Casalongue et al., 2013) (Hulicova-Jurcakova et al., 2009). The N 1s spectra demonstrate the existence of pyrrolic (399.25eV) and graphitic N (400.84-401.61eV) (Hou et al., 2015). The intensity of O 1s in CuS NPs (**Figure A. S2.3e**) is much higher than that in the core-shell NPs, suggesting the success of the SDS cultivation. Because of the influence of low intensity of graphitic N at peak around 400-401 eV for N 1s, the corresponding peak at 289.5 eV for C 1S of C–N/C=N bond in **Figure 2.4d** is insignificant in the deconvoluted spectra (Yuanjian Zhang et al., 2013).

Figure 2.4. Deconvoluted XPS spectra of (**a**) In 3d, (**b**) Cu 2p, (**c**) S 2p, (**d**) C 1s, (**e**) O 1s, and (**f**) N 1s for the 10% (wt) CuS@ In_2S_3 core-shell NPs. *Note* that the blue, red, and black curves represent the counts, envelop, and deconvoluted data line correspondingly.

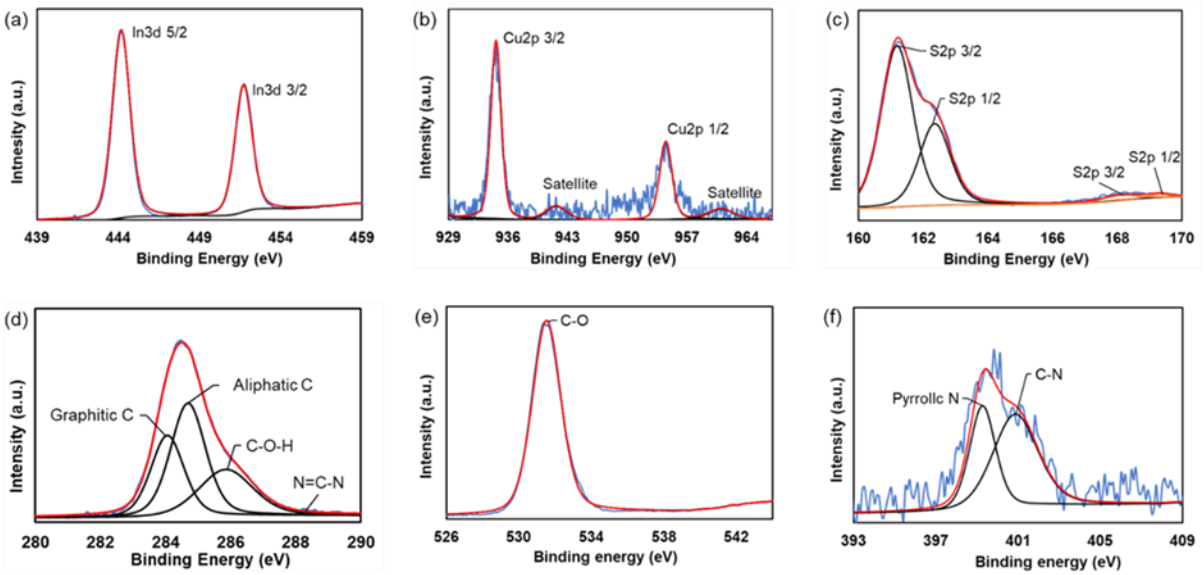

Figure 2.5 displays representative TEM images of the 10wt% CuS@In_2S_3 hybrid NPs and the CuS NPs for a comparison. The average size of the hybrid NPs is 6.34 ± 0.31 nm and 5.50 ± 0.21 nm for the CuS NPs (**Figure A. S2.4**). As aforementioned, the calculated crystalline size using W-H equation was 6.27 nm for the 10wt% CuS@In_2S_3 NPs, a good agreement with the TEM size range. **Figure 2.5A1** shows some extent aggregation of the hybrid NPs. A higher magnification TEM image of individual NPs (**Figure 2.5A2**) displays core-shell structure. The localized crystalized domains of β-In_2S_3 (2212) and CuS (107) were observed with measured interplanar distances around 1.9 Å and 2.0 Å, respectively, consistent with the calculated results from XRD spectra (**Table A. S2.2**). **Figure 2.5A3** displays the selected area electron diffraction (SAED) pattern of the 10wt% CuS@In_2S_3 NPs. The diffraction patterns show a polycrystalline structure with low crystallinity level. The property is caused by the amorphous lattice structure

of the NPs, and this feature was supported by the broad XRD patterns (**Figure 2.2**). On the other hand, the CuS NPs were dispersed very well from the low magnification TEM image (**Figure 2.5B1**). The high-resolution image (**Figure 2.5B2**) shows a localized crystal domain (107) which has the same interplanar distance as in the 10wt% CuS@In_2S_3 NPs, indicating the stability during the core-shell synthesis. A few spots in the SAED pattern of different radius (**Figure 2.5B3**) suggest some localized lattice structures, corroborating with the low level of crystallinity from the XRD results (**Table A. S2.2**).

Figure 2.6a shows typical UV-vis absorption spectra of the five different NPs. The CuS NPs have very low absorbance under visible light range. The NPs containing In_2S_3 have high intensity light absorbance than the bare CuS NPs. The 10wt% CuS@In_2S_3 NPs have the highest light absorbance compared to 5wt% or 15wt% CuS in the UV-vis range.

Tauc's law was used for estimating the optical bandgap energy of the synthesized NPs, as expressed in following equation (Makuła et al., 2018).

$$(\alpha h\upsilon)^2 = B(h\upsilon - E_g) \quad (2.3)$$

The parameters of α, h, υ, B, and E_g are the absorption coefficient, Planck's constant, frequency of the absorptive light, band tailing parameter, and bandgap energy respectively. According to the spectra in **Figure 2.6a**, the apparent optical bandgap energy can be obtained by linear portion extrapolating of the $(\alpha h\upsilon)^2$ versus hυ (**Figure 2.6b**). We got bandgap energy of 3.05 eV for the CuS NPs, 2.45 eV for In_2S_3, 2.40 eV for 5wt% CuS@In_2S_3, 2.32 eV for 10wt% CuS@In_2S_3, and 2.80 eV for 15wt% CuS@In_2S_3 NPs, respectively. The decrease of measured bandgap energy in hybrid NPs can be attribute to the formation of the heterojunction and increase of photoactivity (Do et al., 2018). The low bandgap of 10wt% CuS@In_2S_3 NPs suggests that a wide range of visible light could possibly be used to excite the NPs for photocatalysis.

Figure 2.5. The TEM images of the 10wt% CuS@In_2S_3 core-shell NPs (A1, A2, and A3) and CuS NPs (B1, B2, and B3). The A1 and B1 show NPs distribution in low magnification; The A2 and B2 present higher magnification images with inserted lattice images; and the A3 and B3 illustrate SAED patterns.

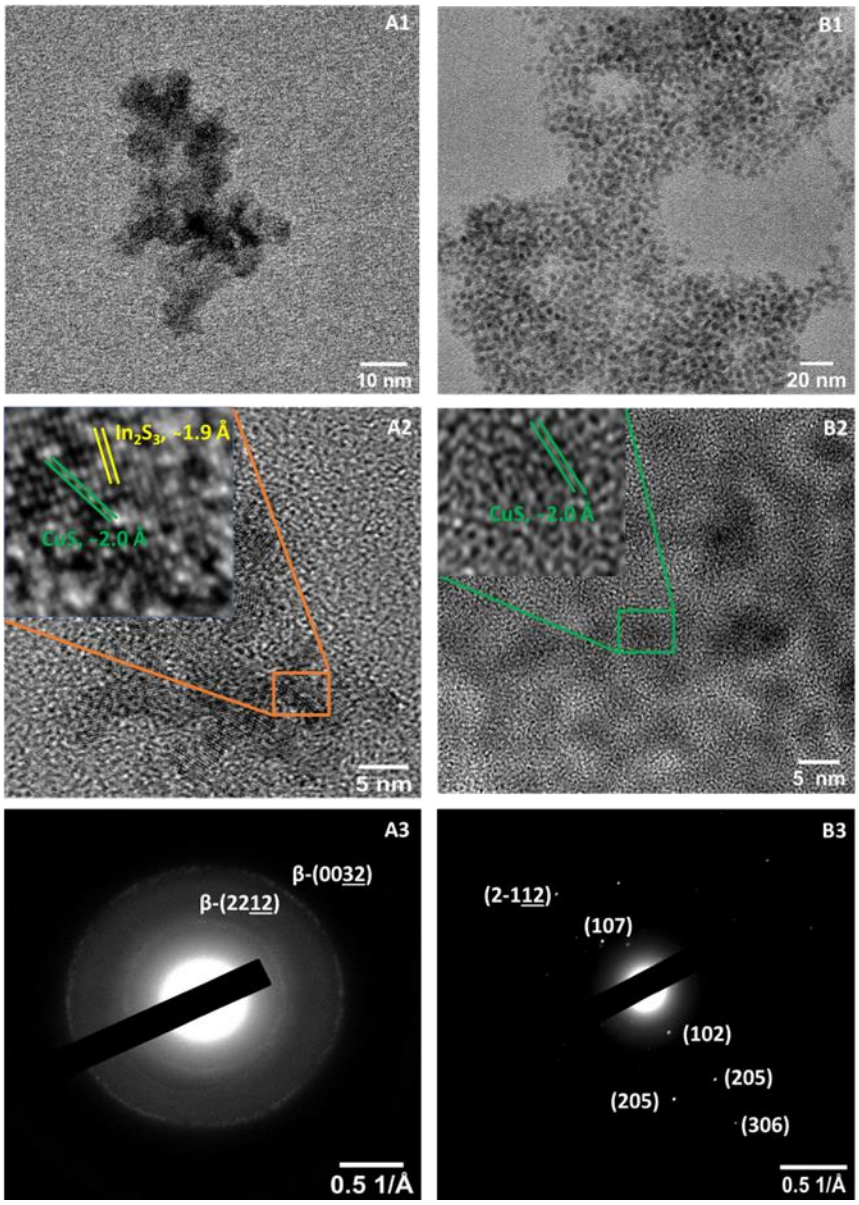

Figure 2.6a. UV-vis absorbance spectra of different NPs; **b.** Tauc's plots of the NPs obtained by the absorbance spectra; and **c.** Photoluminescence (PL) spectra of different NPs.

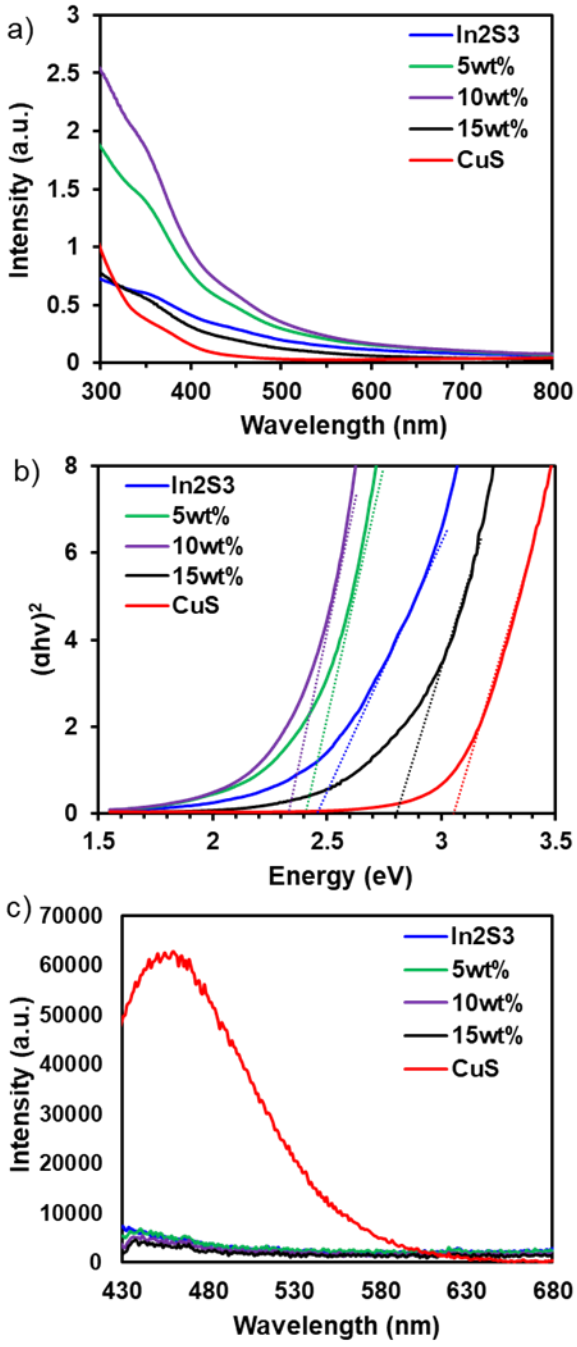

The photoluminescence (PL) spectra of the five NPs excited at 405 nm are shown in **Figure 2.6c**. It shows an obvious PL emissive peak ~460 nm for the CuS NPs, while emission of

hybrid NPs and In_2S_3 NPs is negligible. The low PL emission level from CuS@In_2S_3 NPs was caused by the core and shell heterojunction structures and charge transfer at the interfaces (Do et al., 2018). In addition, the sacrificial S^{2-} anions of In_2S_3 could trap and react with the positively charged holes. In this case, the excited charge carrier transportation between the shell to core interfaces may occur, which inhibits the direct recombination for PL (Pradhan & Uyar, 2017).

Conclusion

The pristine CuS, In_2S_3 and CuS@In_2S_3 core-shell hybridization was successfully fabricated based on a microwave associated solvothermal strategy. The In_2S_3 NPs possess both β and γ crystallization with relatively lower crystallinity. And CuS has a single covellite hexagonal crystal structure under low crystallization level also. For morphology variation, the pristine In_2S_3 has a flower petal shape; and the aggregation became more obvious with the higher addition of CuS. Besides of S, In, and Cu, other organic elements, such as C, O, and N, also can be detected, which organic elements may be introduced by the formation of organic ligand or the SDS cultivation. For the optical behavior, In_2S_3 has obvious higher visible light sensitivity than bare CuS. Because of the construction of the heterojunction and increasing of the photoactivity, 10wt% CuS core-shell hybridized sample displayed a highest intensity on light absorption. On the other hand, the PL emission level of core-shell structures are reduced because of the inhibited charge carrier's recombination.

CHAPTER III: PHOTOCATALYTIC PERFORMANCE OF THE MICROWAVE SYNTHESIZED COPPER SULFIDE, INDIUM SULFIDE, AND THE CORE-SHELL INSTALLATION

This chapter has been published as M. Liu, A. Sheardy, G. Pathiraja, F. Tukur, A. Jayapalan, J. Wei. Tuning the Core-Shell Ratio in Nanostructured CuS@In_2S_3 Photocatalyst for Efficient Dye Degradation. Cleaner Chemical Engineering (2023).

Introduction

Since the past few decades, over discharging of manufacturing waste has been caused serious environmental problem. Pollutants may exist in solid type such as harmful plastic waste or poisonous heavy metal/metal oxides particles (N. Shen et al., 2019) (Naqash et al., 2020) (Iqbal, Xu, et al., 2020) (X. C. Wang et al., 2019). Industrial waste gas, including CO_2, SO_2, and NO_x etc., had introduced significant badly effect on human beings and other animals. Toxicants may also be released from liquid waste, containing various types of dye, pesticide, herbicide, and antibiotic etc. As the aforementioned, artificial dyes have been regarded as one of serious contaminants; and at least 0.2 million tons of the untreated water is discharged per year into our environment (Al-Mamun et al., 2019). Usually, dyes were categorized based on their molecular structure, chemical composition, or constructing bonds, such as the azo, nitro, xanthene, indamine, sulfur, and ketone (Tkaczyk et al., 2020) (Prado et al., 2008) (Lachheb et al., 2002). Dyes can introduce seriously environmental and health issues. First, induces aesthetic problem due to coverage of colorful dyes on large surface of water. On the other hand, the photosynthesis process of aquatic plants can be affected directly. Furthermore, the aromatic ring and long chain structures commonly constructed organic dyes, hence, they are highly non-biodegraded and

carcinogenic in ecosystem (Rauf & Salman Ashraf, 2012) (Ferraz et al., 2011) (Ito et al., 2016) (Haq et al., 2018).

The common strategy for dyes' elimination in water system can be categorized into physical and chemical treatment (Bhatnagar & Jain, 2005) (Khatri et al., 2015). For physical adsorption or filtration, they are widely utilized (Khatri et al., 2015). The absorbents, such as wood chips, activate clay, cotton waste, bark, or activate carbon etc., can be directly absorb the contaminants in water. Relatively lower cost and easy handling for operation are the most obvious advantages. However, absorbents usually have porous structure which possesses high surface area, so frequent occlusion can decreases working efficiency.

Usually, traditional chemical treatment is a highly effective compared with physical method (Arslan et al., 1999) (Gül & Özcan-Yildirim, 2009). Under the treatment, dyes can be decomposed by high oxidative reagents such as H_2O_2, ozone, or chlorine, etc. For example, H_2O_2 is a common substance which release OH• radical into water system after activation by certain types of iron salt (Gül & Özcan-Yildirim, 2009). In that case, long chain dyes can be easily oxidized by the high oxidative radical into low hazardous and biodegradable compounds. Nevertheless, performance of the reagents is easily affected by environmental factors such as the variation of pH and temperature of aqueous system. Furthermore, chemical reactant may induce second contamination to the environment.

In date, the photocatalyst based indirect chemical method can compensate disadvantages of physical and traditional chemical treatment (Gautam et al., 2020) (Gusain et al., 2019). Based on the method, photocatalysts, such as CdS, ZnS, TiO_2, ZnO, CeO_2 and/or FeO, etc. participate into the degradation process, and contaminants are no longer directly degraded by the chemical reagents. According to the working mechanism in **Figure 3.1**, electrons migrate from valance

band to conduction band with holes' left after light irradiation (Gautam et al., 2020). Then, the electrons and holes react with the dissolved O_2 and H_2O; correspondingly, high oxidative O_2^- and OH• radicals are generated (K. M. Lee et al., 2016) (Raizada et al., 2020). Moreover, the O_2^- may also react with H^+ to form H_2O_2. The created radicals and composition have high sensitivity with organic dyes and can decompose them into CO_2, H_2O, N_2, and other non-toxic compounds.

Figure 3.1. Scheme of fundamental mechanism of the photocatalysis process.

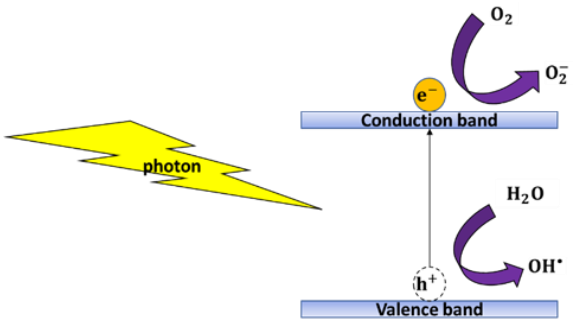

Recently, metal sulfides are regarded as one of the most promising photocatalyst because of the superior visible light sensitivity, environmentally friendly, and low cost (Gupta et al., 2012) (W. Li et al., 2018). However, rapid charge carriers recombination rate and the self-oxidation of S^{2-} influence the photocatalytic efficiency (L. Ma et al., 2015) (Iwase et al., 2016). To improve photocatalytic activity and durability of the catalyst, hybridization with noble/transition metals, metal oxides, other metal sulfides, and carbonaceous materials are the most widely utilized strategies (Ayodhya & Veerabhadram, 2018). Firstly, dopants with high electrical conductivity enhance charge transfer kinetics and conductivity of active sites (Guo et al., 2020). On the other hand, the created atomic defects also increase surface area and the number of active sites; furthermore, S^{2-} anion of metal sulfide is protected from the oxidation of photogenerated holes with the hybridization of hybridized structures (Y. Song et al., 2021).

Specially, the exotic particle creates straddling or staggered configurations between hybridized particles. Instead of quick recombination of photon induced e^- and h^+ pairs, charge carriers can obatin longer duration to stay at the excited level (Isac et al., 2019) (Bai et al., 2018). The theory of the quantum structure modification was explained by **Figure 3.2**.

In this Chapter, a simple and reliable photodegradation testing system was installed. Photocatalytic performance of the CuS, In_2S_3, and their core-shell hybridized NPs (fabricated in Chapter II) are evaluated. The Beer-Lambert's law was conducted the estimation of photodegradation level on MB and MO. Kinetics of photocatalytic degradation reaction was checked based on the Langmuir-Hinshelwood theory.

Figure 3.2a. Scheme of the charge carriers' recombination inhibition mechanism on straddling gap; **b.** the mechanism on staggered gap.

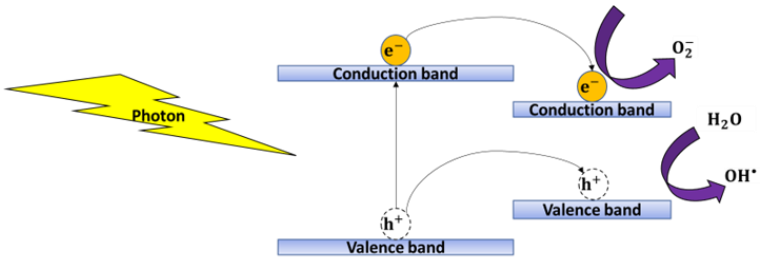

a.

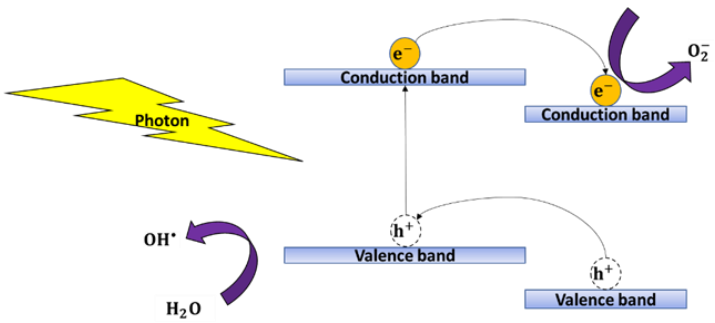

b.

Experimental

The photocatalytic performance of the NPs was tested using MB and MO dye solutions, respectively, at 20 mg/mL in deionized (DI) water. A glass testing tube containing 6 mL and 8 mg NPs as photocatalyst was used for light irradiation. Before adding NPs, UV-vis absorption spectrum was obtained using 100 μL original dye solution diluted to 1.5 mL by DI water and labelled "-30 min". Dye solution was stabilizing in dark for 30 min before light irradiation. A potable blue laser beam (447 nm, 500 mW, 5 mm diameter beam, Big Laser Co.) was used as light source. Before switch on the light, the photocatalyst-dye solution was magnetically stirred under 30 minutes with 1200 rpm in dark environment to reach the absorption/desorption equilibrium with the NPs; and an absorption spectrum was obtained and labeled as '0 min'. During light irradiation, a 100 μL dye solution of was extracted out from the glass testing tube and diluted to 1.5 mL using DI water at every 10 min interval for UV-vis absorption spectrum measurements. Note that all samples containing NPs were centrifuged at 10000rpm for 10 min to get rid of NPs before the spectrum measurement.

Result and Discussion

The photocatalyzed degradation of dye molecules using the NPs was evaluated by determining the decrease of dye concentration measured by UV-vis absorption of dye in solution according to Beer-Lambert's law (Swinehart, 1962). The calculation is expressed in Eq. 3.1 & 3.2. The parameters of A, ε, l, and c are the absorbance, molar absorptivity, length of light path, and concentration of the solute. The degradation efficiency can be obtained in using Eq. 3.2, where A_0 and C_0 represent the initial absorbance and concentration of the solute, respectively.

$$A = \varepsilon lc \quad (3.1)$$

$$\text{Degradation effciency } (\%) = \frac{C}{C_0} \times 100 = \frac{A}{A_0} \times 100 \quad (3.2)$$

The typical UV-vis absorption spectra of MB and MO vs. the reaction time with different NPs in this work are presented in **Figure B. S3.1** and **S3.2** up to 90 min irradiation. The spectra of -30 min are the initial absorption of the dye solutes followed with 30 min in dark before light irradiation, a duration for physical adsorption reaction between the NPs and dye molecules. The control experiments were performed for dye solutions with presence or absence of NPs without light irradiation up to 60 min and the spectra at every 30 min are shown in Figure **B. S3.3** and **S3.4**. It was observed that, after 30 min in dark, the concentration of MB and MO did not change with presence of the 10wt% NPs CuS@In_2S_3 for longer time in dark, suggesting only physical adsorption reaction occur in dark and achieved adsorption equilibrium after 30 min. The equilibrium concentration of MB and MO were respectively obtained at 63% and 80% of the original concentration. For each set of the experiments, minimum three trials were performed for reproducibility. **Figure 3.3** shows the relative concentration (normalized to originally prepared concentration) of dye solute vs. 30 min in dark followed with 30 min irradiation. The plots for up to 90 min are presented in **Figure S3.5**. In both MB and MO treatments, which show the complete of the degradation reaction to the equilibrium. In this study, the 10wt% hybrid NPs show the highest efficiency of dye removal. The best decolorization or degradation efficiency after 30 min irradiation for MB is nearly ~100% while for MO is ~58% (~72% after 90 min). The CuS NPs alone has the lowest efficiency for both MB and MO (10-15%). The In_2S_3 NPs show better performance in MB degradation (~72% efficiency) than that of MO (~20% efficiency) (see **Figure B. S3.5**).

Figure 3.3. Normalized concentration of dye solute **a**) MB and **b**) MO versus reaction time with NPs including a dark period (-30 min) and an irradiation period (+30 min).

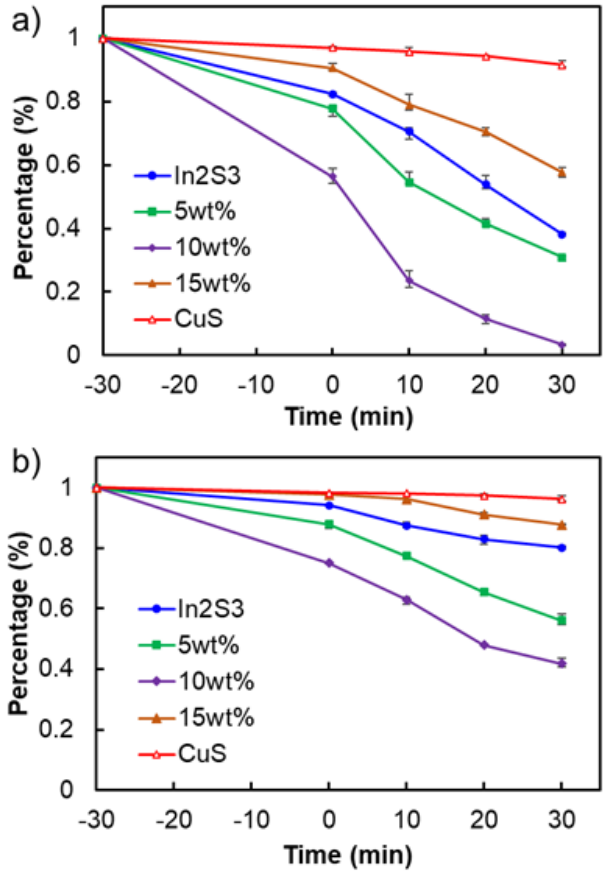

In addition to the photocatalytic activity of the NPs, the degradation difference may partially attribute to the more favorable electrostatic adsorption between the NPs with the MB than with MO, thus more MB available for photocatalyzed degradation, because MB and MO are regarded as cationic and anionic dyes, respectively (Nguyen et al., 2018) (Trandafilović et al., 2017) (S. L. Wang et al., 2018). The Zeta potential of pristine In_2S_3, 5wt% CuS, 10wt% CuS, 15wt% CuS, and pure CuS NPs were measured negatively charged of potential values -9.29, -10.1, -10.3, -10.6, and -11.3 mV, respectively (see **Figure B. S3.6**). It shows the more wt% CuS in NPs is more negatively charged, corroborated by the O intensity in the XPS results which suggest more negatively charged groups. Another factor that may cause less efficiency of MO

degradation is that the azo bond (-N=N-) in MO is strong and hard to be cleaved (Nguyen et al., 2018)(Trandafilović et al., 2017)(S. L. Wang et al., 2018).

Kinetics of photocatalytic degradation reaction was examined by using Langmuir-Hinshelwood model expressed as Eq. 3.3 (Messerer et al., 2006) (K. V. Kumar et al., 2008). In Eq. 3.3, the parameters r, C, k_1 and k_2 represent the degradation rate of solute, concentration of the dye solute, reaction rate constant, and adsorption equilibrium constant of the reactant. At conditions of t=0 for dye concentration is C_0, which is the concentration right after the dark static time. In the case of the low concentration of reactant and weak adsorption, the k_2C value is much smaller than 1, the reaction is approximated to be first order kinetics expressed as Eq. 3.4 where $k=k_1k_2$. Hence, degradation rate constant can be obtained from the slope of $\ln(C_0/C)$ vs. time t in the linear range (Messerer et al., 2006).

$$r = \frac{dC}{dt} = \frac{k_1 k_2 C}{1+k_2 C} \tag{3.3}$$

$$\mathrm{Ln}\frac{C_0}{C} = kt \tag{3.4}$$

We analyzed the kinetics of the photodegradation using the data points within 30 min irradiation treatment. **Figure 3.4** shows the results for different NPs in MB and MO solutions. The C_0 value here used is the equilibrium concentration of dye molecules in solution after 30 min in dark. The degradation rate constant results are summarized in **Table 3.1**. The value of rate constant k quantifies the speed of photocatalytic degradation reaction in the order of 10%wt CuS > 5wt% CuS > pristine In_2S_3 > 15wt% CuS > pristine CuS for both MB and MO dyes. The k value in MB is almost 4.6 times of the value in MO for the 10wt% CuS treatment.

Figure 3.4. Fitting the first order kinetics of the photodegradation using different NPs in **a**) MB solution and **b**) MO solution.

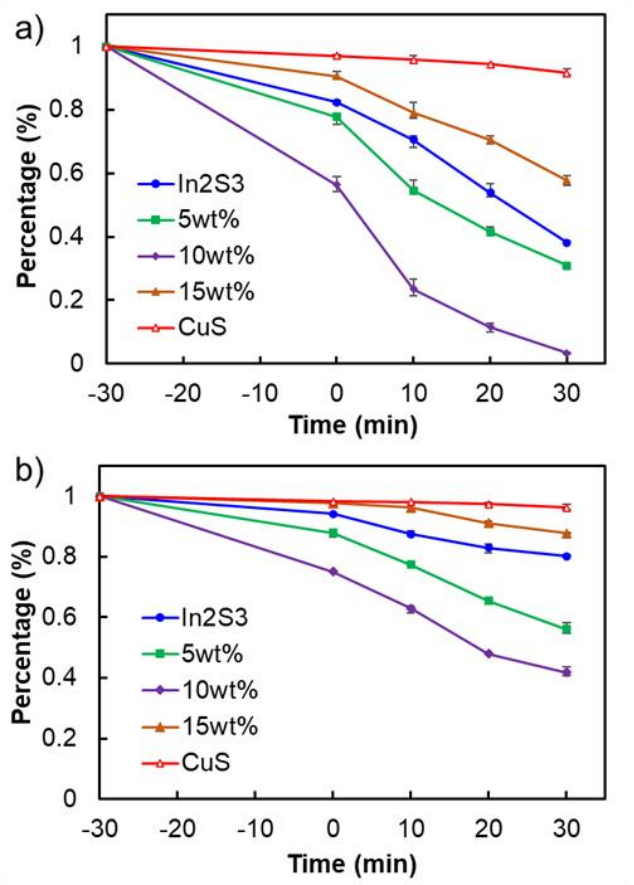

The FTIR spectra was utilized to monitor the photocatalyzed decomposition of MB and MO. **Figure 3.5** shows the measured FTIR spectra in powder, in solution before (-30 min) and after (90 min) light irradiation with presence of 10%wt CuS@In_2S_3 NPs, **Figure 3.5a** & **c** presents a broader range of the wavenumber (1000-4000 cm^{-1}) and **Figure 3.5b** & **d** are the magnification spectra with the range of 1000-2000 cm^{-1}.

Table 3.1. Photodegradation reaction rate constant (*k*) obtained with Langmuir-Hinshelwood model for different NPs in MB and MO solutions.

NPs	**Photodegradation of MB**	**Photodegradation of MO**
	***k* (min^{-1})**	***k* (min^{-1})**
Pristine In_2S_3	0.0258 ± 0.0007	0.0053 ± 0.0002
5wt% CuS	0.0304 ± 0.0003	0.0151 ± 0.001
10wt% CuS	0.092 ± 0.004	0.0203 ± 0.001
15wt% CuS	0.0146 ± 0.002	0.0037 ± 0.0003
Pristine CuS	0.002 ± 0.0002	0.0007 ± 0.0004

Figure 3.5. FTIR spectra of MB (**a** and **b**) and MO (**c** and **d**) before and after 90min photodegradation process using 10%wt CuS@In_2S_3 NPs.

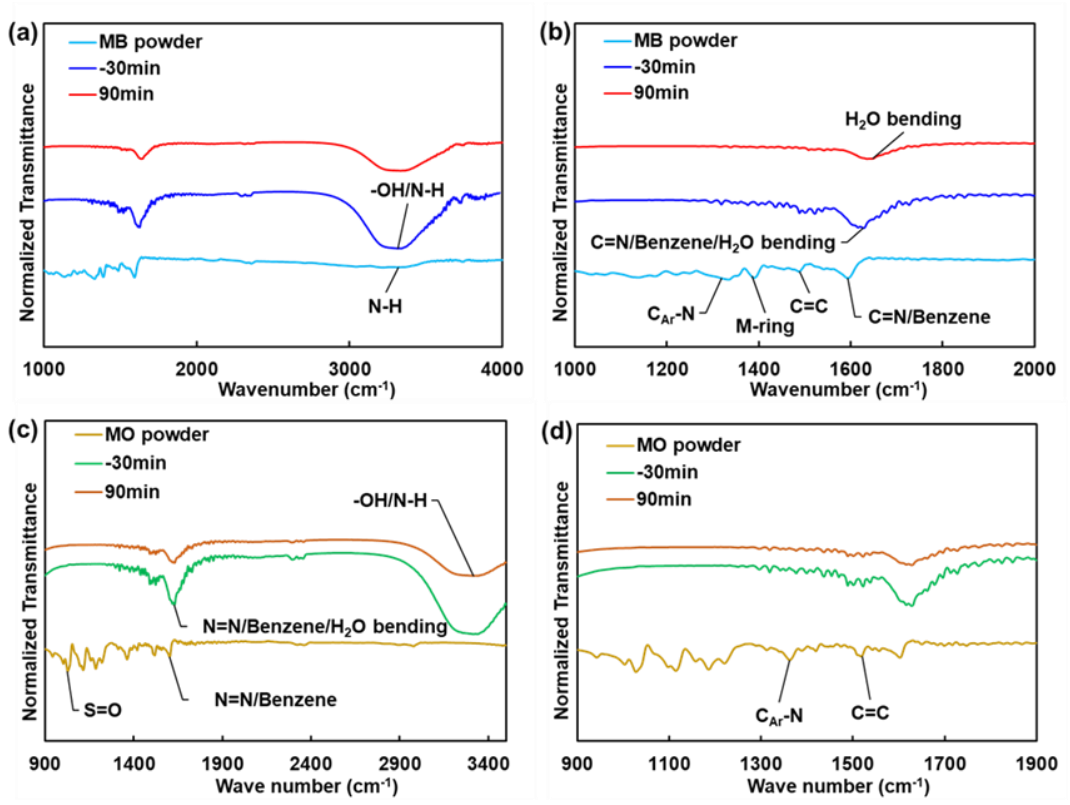

In general, the FTIR spectra in water show that every identical peak of MB and MO dye has obvious reduction after 90 min irradiation. For the MB powder (see **Figure 3.5a** and **b**), the C=N/benzene ring vibration mode is represented by the peak at the wavenumber of ~1590 cm^{-1} (Xu et al., 2011). After the MB dissolved in DI water at concentration 20 mg/L, the peak is shifted forward to the wavenumber of 1627cm^{-1} by the effect of -OH bending vibration (Xueref & Dominé, 2003) (Baruah et al., 2019). After 90 min, the corresponding peak moves to the wavenumber position of 1643 cm^{-1} with significant peak intensity reduction (Baruah et al., 2019). Additionally, the N-H stretching vibration peak of MB in water at 3359 cm^{-1} becomes more profound with the influence of H_2O stretching; while this peak reduced significantly after 90 min irradiation because of the decomposition of N-H in water (Baruah et al., 2019). Furthermore, the wavenumbers of 1319, 1438, and 1488 cm^{-1} in MB FITR spectrum, which illustrate the C-N stretching between side aromatic ring and nitrogen atom (C_{Ar}-N), multiple aromatic rings stretching, and C=C side ring stretching, almost disappear after 90 min photodegradation, suggesting the decomposition and conversion to CO_2, NO^{3-}, SO_3^{2-}, and/or SO_4^{2-} (Xu et al., 2011) (I. Khan et al., 2022).

From the FTIR of MO (**Figure 3.5c** & **d**), the N=N/Benzene vibration is also demonstrated by the wavenumber of 1590 cm^{-1} which shifts to ~1627 cm^{-1} after dissolved in water. After 90 min irradiation for degradation, the peak intensity becomes less however the change is not as significant as that of MB due to the incomplete decomposition (Baruah et al., 2019) (T. Shen et al., 2015) (J. Ma et al., 2012). Similarly, the corresponding intensity of other peaks also decrease after 90 min photodegradation, implying the decomposition of the MO, though not as efficacy as the MB degradation.

Based on our FTIR analysis of the MB and MO before and after photodegradation, a radical induced photocatalytic decomposition reaction is applicable (Nguyen et al., 2018). To better understand the results of this work, the conduction/valance bandgap energy edge of the core CuS and shell In_2S_3 is further analyzed and obtained by Mulliken electronegativity approach (Kong et al., 2019) (see details in **Table 3.2**). The band edge of conduction and valence can be estimated by Eq. 3.5 & 3.6, where χ, E_0, E_g, E_{CB}, and E_{VB} indicate the absolute electronegativity of the material, energy of free electron on the hydrogen scale (NHE ~ 4.5 eV), the apparent optical bandgap energy obtained in Tau's law, conduction (CB) and valence (VB) band edge of the NPs (N. Li et al., 2018). In this case, electronegativity of the single element (In, Cu, or S) and compounds can be calculated using Eq 3.7, 3.8, and 3.9 from the first ionization potential (I) and electron affinity (A) of each element provided in **Table 3.2** (Kong et al., 2019). The calculated values of conduction and valence band of the In_2S_3 are -1.02 eV (CB) and 1.43 eV (VB), and -0.72 eV (CB) and 2.30 eV (VB) for CuS vs. NHE.

$$E_{CB} = \chi_{CuS/In_2S_3} - E_0 - \frac{1}{2}E_g \quad (3.5)$$

$$E_{VB} = E_{CB} + E_g \quad (3.6)$$

$$\chi_{In/Cu/S} = \frac{I_{In/Cu/S} + A_{In/Cu/S}}{2} \quad (3.7)$$

$$\chi_{CuS} = (\chi_{Cu} \times \chi_S)^{\frac{1}{2}} \quad (3.8)$$

$$\chi_{In_2S_3} = (\chi_{In}^2 \times \chi_S^3)^{\frac{1}{5}} \quad (3.9)$$

Table 3.2. Ionization potential and Electron affinity used for the calculation of band edge.

Element	*Ionization potential (I, eV)*	*Electron affinity (A, eV)*
In	**5.7864** (Afroz et al., 2020)	**0.40** (Rienstra-Kiracofe et al., 2002)
Cu	**7.7246** (Chan et al., 1998)	**1.23** (Oros-Ruiz et al., 2013)
S	**10.36** (Laming, 2009)	**2.07** (Köhler & Chang, 2000)

According to the obtained CB and VB edge values, the potential charge carrier transfer in the hybrid NPs under irradiation and the reaction mechanism for the photodegradation of MB and MO are proposed schematically in **Figure 3.6**. Under irradiation to the hybrid CuS@In_2S_3 NPs, electrons in the valence band (VB) are excited to the CB to form paired excitons. The excited electron and hole pairs could partially recombine immediately for photoemission; however, a fraction of the excited charge carries may transfer to the interface between the NPs and solutions. The more charge carrier separation and transportation through the interfaces, the more recombination is inhibited, and the photocatalytic activity can be enhanced for the hybrid NPs. The photoemission results suggest most of the exciton pairs in the hybrid CuS@In_2S_3 NPs are inhibited from recombination. The excited electrons migrate to the surfaces of NPs may reduce adsorbed oxygen into anionic superoxide radicals ($\bullet O_2^-$) or further react with H^+ to be H_2O_2 at the surfaces of the NPs; while the holes may oxidize water molecules or hydroxyls to convert highly active •OH radicals (Khanchandani et al., 2013). As a result, these active species including excited electron-hole pairs, $\bullet O_2^-$, H_2O_2, •OH can effective catalyze the degradation of the dye molecules to smaller intermediates then the final products CO_2 and H_2O, along with the nitride, sulfite, and/or sulfide salt (Xu et al., 2011) (Pirhashemi et al., 2018) (Lv et al., 2022).

Figure 3.6. Schematic view of the charge carrier transportation of the hybrid NPs under irradiation (A), and proposed reaction mechanism of photodegradation of dye molecules (B).

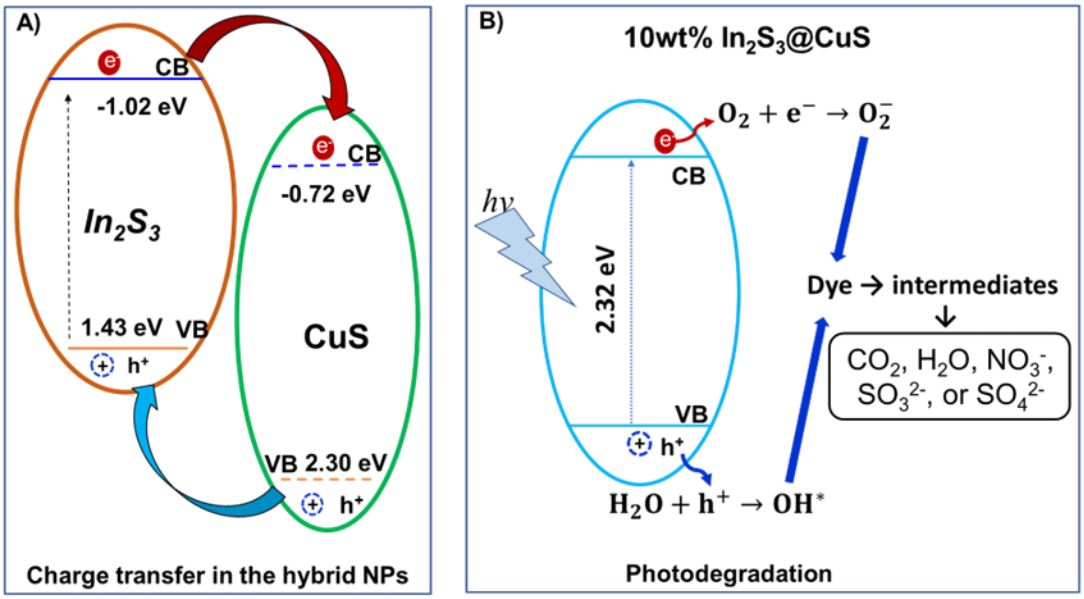

In this work, the photocatalytic activity in 10wt% hybridized shows the best efficacy in the dye photodegradation. Firstly, as above mentioned, the bandgap of 10%wt CuS@In_2S_3 NPs is smaller than the 5%wt and 15%wt NPs, thus offer a wide range of light absorption for increased photocatalytic activity. Moreover, it is obvious that the photocatalytic efficiency relies on radical generation based on the pair separation and photodegradation mechanism. In this case, the sacrificial S anions on the surface of the NPs plays critical roles not only in the excitation to generate electron hole pairs, but also the charge carrier transportation through the heterojunction interfaces between CuS and In_2S_3 to inhibit recombination (N. Li et al., 2018) (Do et al., 2018). At the heterojunction interfaces, dangling bonds and S vacancies might be generated at the presence of In^{3+}/Cu^{2+} charge unbalance, leading lattice defects for photoactive sites (Do et al., 2018). Consequently, the photocatalytic activity increases with the increment of the CuS weight percentage from 5wt% to 10wt%. However, further increasing CuS weight ratio (15%) renders

lower photocatalytic efficiency in this study, which may be a tradeoff of the larger bandgap (2.80 eV) caused less light absorbance.

Figure 3.7. Recyclability of the 10wt% CuS@In_2S_3 NPs for photodegradation of MB (**a**) and MO (**b**).

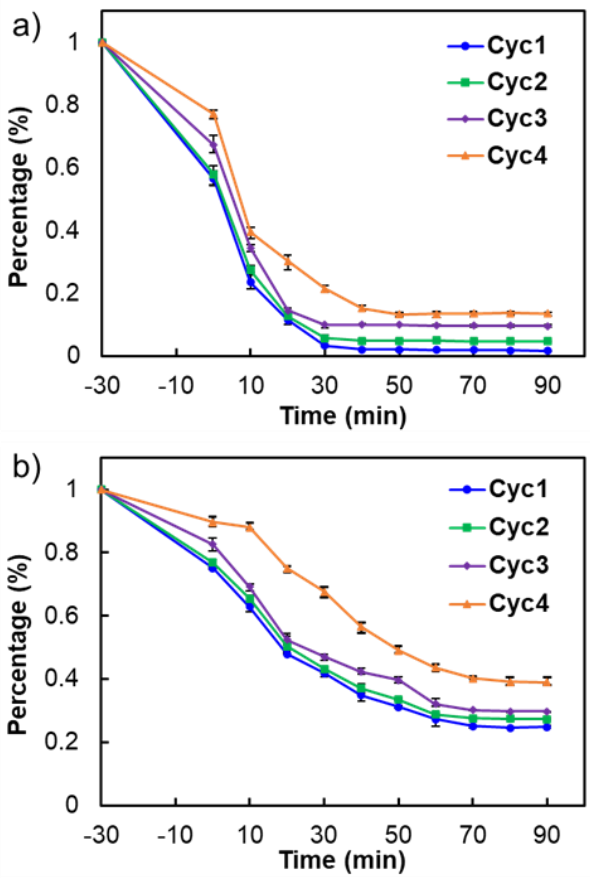

Reusability of the 10%wt CuS@In_2S_3 NPs was performed for 4 cycles. After a former photodecomposition test, the NPs were collected by the centrifugation of 10000 rpm for 10 min. The photocatalyst was rinsed by DI water 2 times followed with 5 min sonication. Then, the NPs were redispersed again into a new MB or MO dye solution for photodegradation measurements. The reusability efficiency for MB and MO are shown in Figure 8. The average MB degradation efficiencies from the 1st to the 4th cycle at 90 min irradiation are 98.7%, 95.3%, 90.5% and

86.4%, and for MO are 75.2%, 72.7%, 70.2% and 61.0%, respectively. The results demonstrate high recyclability/reusability and corrosive resistance of the 10%wt CuS@In_2S_3 core-shell construction for photodegradation applications (A. Kumar et al., 2018).

Conclusion

In this Chapter, fabricated In_2S_3, CuS, and the CuS@In_2S_3 NPs were applied on the photodegradation of MB and MO dye solution. With more addition of CuS, the photocatalytic efficiency increased, and the 10wt% core-shell hybridized NPs. The reaction rate constant of the 10wt% on MB and MO degradation are 0.092 and 0.0221/min, respectively. Firstly, the reduced bandgap energy offers a wide range of light absorption. Secondly, the heterojunction structure interface inhibits the quickly charge carriers recombination rate.

CHAPTER IV: OXYGEN EVOLUTION REACTION AND OXYGEN REDUCTION REACTION PERFORMANCE OF THE MICROWAVE SYNTHESIZED COPPER SULFIDE, INDIUM SULFIDE, AND THE CORE-SHELL INSTALLATION

Introduction

OER and ORR performance control the performance of cathode side of MABs and FCs (K. Sheng et al., 2021) (W. H. Lee et al., 2021) (Q. Zhang & Guan, 2021). To fabricate the low cost, high active, and high stable catalyst are necessary to keep or enhance columbic efficiency and recyclability of MABs and FCs systems. For OER, it is known as one branch of water splitting reaction. Compared with the countered hydrogen evolution reaction (HER), the former is a more kinetic sluggish 4 steps electron transfer process (Xiaorui Gao et al., 2020) (Lu et al., 2020). The reaction is highly pH dependent. Each step of electron transferring under an acidic environment can be expressed by the formula from Eq. 4.1 to 4.4, in which M represent the active site of the catalyst (Suen et al., 2017). Simultaneously, the 4 electron transfer steps under alkaline solution are represented by Eq. 4.5, 4.6, 4.7, and 4.8, respectively (Suen et al., 2017).

$$M + H_2O \rightarrow MOH + H^+ + e^- \quad (4.1)$$

$$MOH + OH^- \rightarrow MO + H_2O + e^- \quad (4.2)$$

$$MO + H_2O \rightarrow MOOH + H^+ + e^- \quad (4.3)$$

$$MOOH + H_2O \rightarrow M + O_2 + H^+ + e^- \quad (4.4)$$

According to the theory of catalysis process, energy barrier of the kinetic sluggish reaction can be reduced to lower level (Suen et al., 2017). With the binding of precursor and intermediate, oxidation state of catalyst may be shifted temporarily until the release of the product. To estimate the electrocatalytic activity, some essential parameters, such as polarization curve, overpotential (η), Tafel slope (b), and/or exchange current density (i_0), are utilized (Tahir

et al., 2017). Polarization curve usually can be obtain based on linear sweep voltammetry (LSV) or cyclic voltammetry (CV) analysis system, and the important parameters are obtained from the curves. The material, which has lower η value, possess higher catalytic activity. Tafel slope and exchange current density are the relative parameters. The relation between these two parameter is demonstrated by Eq. 4.9, where b, j_0, j, and η are the Tafel slope, exchange current density, reaction current density and overpotential correspondingly (Shinagawa et al., 2015). Tafel slope illustrates the magnitude of overpotential needs to be increased to increase reaction rate by a factor of ten. In that case, a better catalyst should have lower Tafel slope value (Marshall & Vaisson-Béthune, 2015).

$$M + OH^- \rightarrow MOH + e^- \quad (4.5)$$

$$MOH + OH^- \rightarrow MO + H_2O + e^- \quad (4.6)$$

$$MO + OH^- \rightarrow MOOH + e^- \quad (4.7)$$

$$MOOH + OH^- \rightarrow M + O_2 + H_2O + e^- \quad (4.8)$$

$$\eta = b\log\frac{j}{j_0} \quad (4.9)$$

Compared with OER, the ORR is a reverse reaction. Theoretically, ORR is also known as sluggish 4-electron transfer pathway, and the reaction is highly pH dependent too, which means that the mechanism of intermediates' absorption and transferring under acidic (Eq. 4.10 to 4.14) or alkaline (Eq. 4.15 to 4.19) environment is different (R. Ma et al., 2019). Under the reaction, it starts from the absorption of O_2, and the first electron contribute to the formation of OOH^* intermediate; the formation of followed intermediates is determined by the pH value of the electrolyte. Additionally, H_2O_2 will appear with a 2-electron transfer pathway (Stacy et al., 2017). For the reaction, two hydrogen atoms are provided to combine with absorbed O_2 for H_2O_2 generation (Eq. 4.20); however, the mechanism is distinct in alkaline solution (Eq. 4.21).

$$O_2 + M \rightarrow MO_2 \quad (4.10)$$

$$MO_2 + H^+ + e^- \rightarrow MOOH \quad (4.11)$$

$$MOOH + H^+ + e^- \rightarrow MO + H_2O \quad (4.12)$$

$$MO + H^+ + e^- \rightarrow MOH \quad (4.13)$$

$$MOH + H^+ + e^- \rightarrow H_2O + M \quad (4.14)$$

Performances of OER and ORR highly depends on intrinsic properties of electrocatalyst. According to Sabatier theory, a selected catalyst material needs to have optimized absorption energy and overpotential on the state of precursors absorption and intermediates transferring, which the absorption energy should not be very low or high so that the precursors or products cannot be bonded or release easily from the active sites of electrocatalyst (Wodrich et al., 2021). In that case, common type of catalyst is based on noble metal/oxides, and the materials located at vertex of the 'Volcano-plot' (Wodrich et al., 2021). In general, traditional OER catalyst are IrO_2, RuO_2, PtO_2, and RhO_2; and, Ag, Pd, Pt, and Ir are the most prevalent ORR catalyst (Z. F. Huang et al., 2017). Normally, noble metal based particle has outstanding electrocatalytic activity and charge carriers transfer rate, however the high cost on extraction and manufacturing limit the utilization in large scales. Additionally, because of difference of working mechanism and operating potential, a noble based material cannot satisfy the requirement of OER and ORR at the same time (Hoshi et al., 2013) (Reier et al., 2012). For example, Pt has high activity on ORR, the current density can be as high as 6.5 mA/cm^2 at 0.5 V (Vs. Reversible hydrogen electrode (RHE)). However, the performance the material is quenched on OER process (Hoshi et al., 2013) (Reier et al., 2012). On the other hand, separated installation of OER and ORR material on the individual working electrode not only can increase the complexity of manufacturing process but also decrease there cyclability of the electrocatalyst (Fu et al., 2019).

$$O_2 + M \rightarrow MO_2 \quad (4.15)$$

$$MO_2 + H_2O + e^- \rightarrow MOOH + OH^- \quad (4.16)$$

$$MOOH + e^- \rightarrow MO + OH^- \quad (4.17)$$

$$MO + H_2O + e^- \rightarrow MOH + OH^- \quad (4.18)$$

$$MOH + e^- \rightarrow OH^- + M \quad (4.19)$$

$O_2 + 2H^+ + 2e^- \rightarrow H_2O_2$ (2-electron pathway, in acidic solution) (4.20)

$O_2 + H_2O + 2e^- \rightarrow HO_2^- + OH^-$ (2-electron pathway, in alkaline solution) (4.21)

In general, to obtain high catalytic activity, charge transfer kinetics, and chemical stability, hybridization is a most popular goal for the improvement of bifunctional catalyst (Y. L. Zhang et al., 2020a). Firstly, the carbonaceous particles decorated noble metal is available combination (Su et al., 2016). Because of the participation of carbon based material, active site and charge transfer kinetics are be improved by the outstanding high surface area and electrical conductivity of the doped material (Y. L. Zhang et al., 2020b). Other non-metal materials, such as heteroatom doped graphene, decorated carbon nanotube, and the 3D porous carbon material, also have high catalytic activity on both OER and ORR process (Y. L. Zhang et al., 2020b). Additionally, spinal and perovskite constructed transition metal oxides, which possess the properties of high surface area, large numbers of active sites, and excellent electrochemical stability, etc. are concerned as the candidate of high performance bifunctional materials (Z. F. Huang et al., 2017). Even though the catalytic mechanism is still under debates, but the microstructural perturbation can enhance the absorption of intermediates significantly.

The influence of bandgap energy of the synthesized NPs on the electrocatalytic performance will be investigated by OER and ORR tests. Polarization curves were created by the assistance of 3-electrode rotating disk electrode system which helps eliminate the ununiform

mass diffusion and generated bubbles on the surface of working electrode. Catalytic activity was studied by Tafel slope. The charge transfer kinetics was furtherly detected by the electrochemical impedance spectroscopy. On the other hand, because of the shortage of current reference on the evaluation of metal sulfides based electrocatalyst, this Chapter also provide a databased for future research.

Experimental

To obtain a homogenous diffusion rate, RDE system (RRDE-3A Ver. 3.0) was applied for OER and ORR analysis. The geometric structure of the glassy carbon (GC) tip of the RDE is displayed in **Figure 4.1**, in which the surface area of the circle GC is 0.071 cm^2. Initially, the GC surface was cleaned by IPA and washed by deionized (DI) water several times with polishing by the 0.05 μm alumina Micropolish powder for 10 min (CH Instrument Inc.). Then, the tip was dried into oven under atmosphere for 1 hour.

In Chapter II, the synthesized NPs had already been dissolved into toluene. So, the NPs needs to be extracted and re-dispersed into IPA for utilization of electrocatalyst ink. Initially, 0.5 mL NPs – toluene solution was taken, and the NPs were collected by 10000 rpm centrifugation for 10 min. After residual toluene was removed, 0.5 mL IPA solvent was added again. To furtherly remove residual impurity, the solution was sonicated for 10 min and centrifuged again under 10000 rpm, 10 min. After the waste was pooled away carefully, new IPA was injected again. This purging process was repeated by 3 times. Finally, the NPs were dissolved into 0.5 mL IPA. Finally, 30 μL Nafion binder was homogenously mixed with the NPs – IPA solution under 60 min sonication.

5 μL (~0.08 mg) electrocatalyst inks were drop-casted on the surface of the GC. Platinum wire (0.5 mm diameter) and Ag/AgCl (filled with 1 M KCl) was applied for counter and reference electrode, respectively. The OER and ORR performance were recorded on the electrochemical working station (biologic VMP3). 1M KOH solution was utilized for the electrolyte on both OER and ORR analysis. The scan rate was 50 mV/s on both OER and ORR test also. Rotating speed of the RDE was controlled at 2000 rpm. Working potential of OER were limited under the region of 0 – 2V (Vs. Ag/AgCl). However, the working potential of ORR test was arranged from -0.8 to 0.2 V (Vs. Ag/AgCl). Before the first LSV scan, either N_2 or air was injected into the electrolyte 2 hours to obtain a N_2 or O_2 saturated environment. But, for the following scan after the first, N_2 or air was also pumped into the electrolyte for 20 minutes before next test. Additionally, the potential was measured versus the Ag/AgCl reference electrode in this report.

To furtherly study the charge transfer rate and kinetics, electrochemical impedance spectrum (EIS) test was also completed based on a same 3-electrodes system. As the same method as before, corresponding NPs was drop-casted on the surface of GC tip, but rotating of the RDE system was kept off. Charge transfer resistance were measured based on the redox reactions between ferrous and ferric ion; so, a 5 mM $K_3Fe(CN)_3$ solution (mixed with 0.1 M KCl) was used for the electrolyte in this experiment. The magnitude oscillation voltage was set as 10 mV (Vs. open circle voltage). The frequency was arranged from 0.1 to 200 KHz. As similar as before, N_2 was also pumped into the electrode for purging.

Figure 4.1. Geometric structure of GC tip of the RDE system

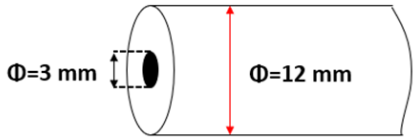

Result and Discussion

OER performance of different samples was displayed in **Figure 4.2a**. In general, NPs did not possess obvious high electrocatalytic activity under relatively lower working potential. For instance, the potential at 10 mA/cm^2 for In_2S_3, 5wt%, and 10wt% have the similar value of 1.47 V. For 15wt% and CuS, they displayed the approximate same value on 1.50 V. According to current references, onset potential of the state-of-the-art OER catalyst IrO_2 and RuO_2 at 10 mA/cm^2 are nearly 0.60 V (H. Singh et al., 2022) (Touni et al., 2019). However, in our experiment, current density at 1.0 V was less than 1 mA/cm^2 in the 10 wt% CuS@In_2S_3 core-shell NPs. The dull electrocatalytic performance may be rendered by larger bandgap energy of the NPs which gave stronger semiconductor behavior. So, the electronic conductivity can be restrained, and higher working potential needs to be added to provide more energy for electrons' migration (Cho et al., 2016). We estimated the electrocatalytic performance of different NPs based on the magnitude of the current density. In this case, the 10wt% NPs had the highest current density value of 184.2 mA/cm^2 at 2 V, which value was approximately 1.6 and 2.6 times' larger than the pristine In_2S_3 and CuS. It also can be detected from the polarization curves that the electrocatalytic activity of NPs were bandgap energy dependent, which tendency was as same as the photocatalytic performance showed in Chapter III.

Electrocatalytic activity were also studied by Tafel slope, in which the original polarization curve was replotted under the relations of potential versus logarithm of current

density (Mondal et al., 2022). Tafel slopes and the value were summarized in **Figure 4.2b** and Table **4.1**. It can be detected that variation of the value has the same tendency with the change of bandgap energy. Even though, Tafel slope of fabricated NPs were obvious higher than the eminent InO_2 and RuO_2 catalyst, the 10wt% core-shell NPs displayed the lowest value. Moreover, current density without catalyst has a significant low value, so, the synthesized NPs also have electrocatalytic activity, and which need to be enhanced by other strategies.

Figure 4.2a. LSV plots of the fabricated NPs under OER test; **b.** Tafel slopes of different NPs.

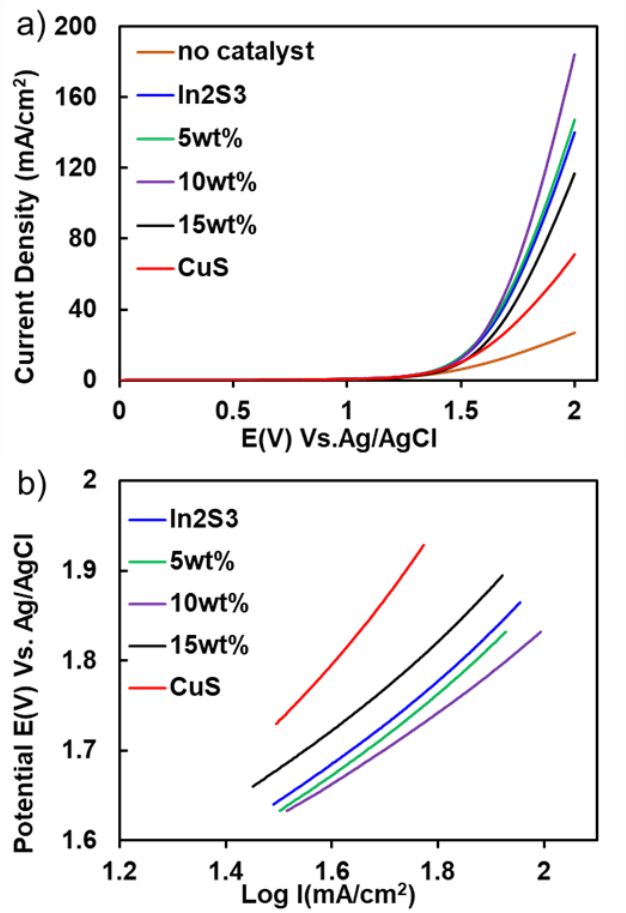

Table 4.1. Summary of the Tafel slope values in OER tests.

Sample	**Tafel slope (mV/dec)**
In_2S_3	479.4
5wt%	466.2
10wt%	416.6
15wt%	497.1
CuS	716.4

ORR activities of the NPs were also studied by the RDE system under 1 M KOH electrolyte with a set-up scan rate of 50 mV/s. The polarization curves were obtained under the rotating speed of 2000 rpm (see **Figure 4.2a**). Compared with the electrocatalytic performance in OER test, ORR activity of synthesized NPs was more sluggish. At the lower working potential region, current density values' change also follows variation of bandgap energy. For instance, under the potential region of -0.8 ~ -0.64 V, 10wt% CuS@In_2S_3 NPs exhibited the highest performance than others. However, the conclusion was not stable under high potential area. At the potential larger than -0.64 V, several plateaus appeared on the polarization curve. The noise usually existed on the catalyst particles which had been decorated by carbon material or carbon participated radicals that can interrupt the immobilization and transportation of ORR precursors and intermediates (Masa et al., 2012) (Hu et al., 2005) (Bocchetta et al., 2016). Because of the low electrocatalytic activity the NPs, the effect on carbon participated composition was more obvious (Hu et al., 2005) (Bocchetta et al., 2016).

Tafel slopes of NPs under the ORR tests are also displayed in **Figure 4.3b**. Simultaneously, the values were summarized in **Table 4.2**. The trend of the variation of catalytic

performance also depends on bandgap energy modification. Because of the bandgap energy reduction by core-shell assembling, 10 wt% NPs had the lowest value. However, stronger semiconductor property and carbon participated radicals provided largely negative influence on electrocatalytic activity. For instance, the terminal current density of the 10wt% NPs was less than 1 mA/cm^2. Compared the Tafel slope value with the OER conclusion, the value in ORR was almost 2.2 times' larger than it. Additionally, ORR performance of the 10 wt% $CuS@In_2S_3$ sample was examined under O_2 or N_2 saturated circumstance respectively. In **Figure 4.4**, even the catalyst displayed low current density under OER and ORR test, the current density in N_2 saturated environment was almost 0, illustrating the high sensitivity of the NPs in the ORR test. So, it also demonstrated that the NPs have large space on electrocatalytic activity enhancement.

Charge transfer resistance was measured based on redox reaction between ferrous and ferric ions. **Figure 4.5** exhibited the Nyquist plots, and the inset illustrates equivalent circuit on data fitting and analysis, in which the parameters of R_c, R_{ct}, and Z_w present the contact resistance of the electrolyte, charge transfer resistance at the interface of electrode-electrolyte, and Warburg impedance (Quevedo et al., 2018) (Tajdid Khajeh et al., 2020). The C_{dl} represent the constant phase element which related with double layer capacitance. Charge transfer resistance was represented by the semicircle of the normalized Nyquist plot. The plot of In_2S_3, 5wt%, and 10wt% NPs displayed a complete semicircle, but the curve owned a pseudo semicircle in the 15wt% and CuS sample. The distortion of the semicircle region may induced by the enlarged bandgap energy with the more addition of CuS NPs (Bo et al., 2012) (Premathilake et al., 2017). The charge transfer resistances were approximately measured, which are 69.0, 68.7, 52.1, 97.3, and 103.7 Ohm for pristine In_2S_3, 5wt%, 10wt%, 15wt%, and bare CuS NPs, respectively. The variation of the resistance has an inversed relation with the change of bandgap energy. Compared

with other reference, the charge transfer resistance of the 10wt% NPs value in our research is approximately 3 to 4 times' larger (H. Singh et al., 2022) (Mondal et al., 2022). So, it was confirmed that the stronger semiconductor behavior quenched the OER and ORR activity.

Figure 4.3a. ORR polarization curve of the pristine In_2S_3, CuS, and their core-shell installed NPs; **b.** Tafel slope of the corresponding NPs.

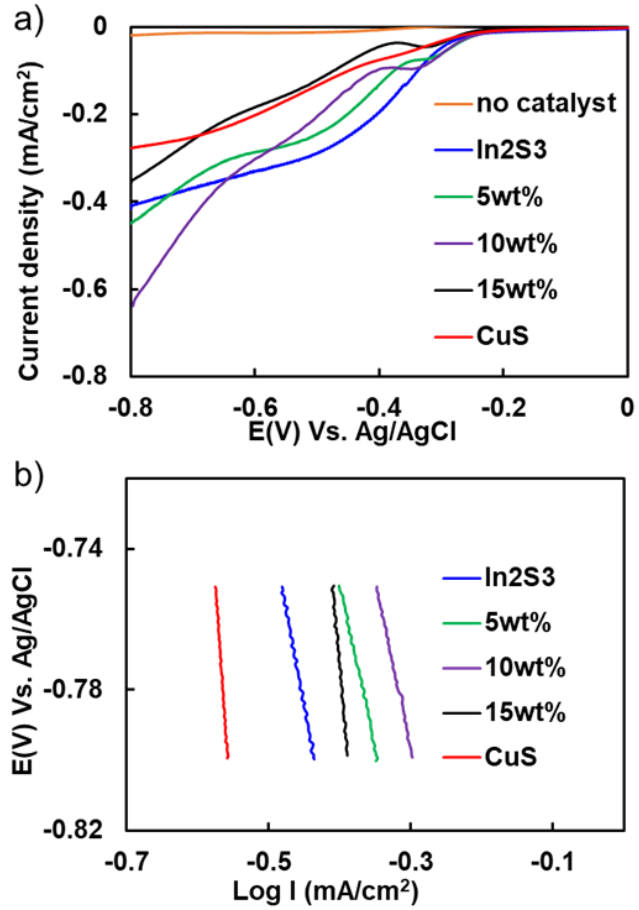

Table 4.2. Tafel slope value of different NPs under the ORR tests.

Sample	Tafel slope (mV/dec)
In_2S_3	109.2
5wt%	109.0
10wt%	104.4
15wt%	110.3
CuS	147.8

Figure 4.4. ORR catalytic performance of the 10 wt% NPs with O_2 or N_2 saturated circumstance under the rotating speed of 2000 rpm.

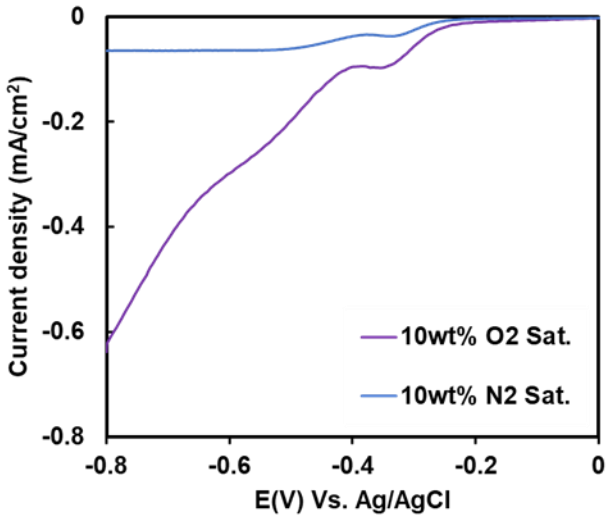

Figure 4.5. Nyquist plots of pristine In_2S_3, 5wt% CuS, 10wt% CuS, 15wt% CuS, and bare CuS NPs.

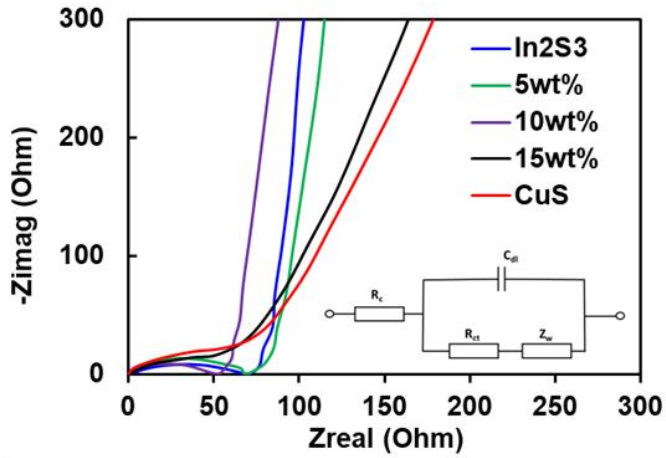

Conclusion

In this Chapter, electrocatalytic performance were tested based on the microwave synthesized In_2S_3, CuS, and their core-shell hybridized structure. According to the polarization curves, Tafel slopes, and Nyquist plots, 10wt% CuS core-shell Hy-NPs possess the highest OER and ORR catalytic activity. However, the larger bandgap energy induced low electronic conductivity limited the electrocatalytic performance of the NPs.

CHAPTER V: THE OXYGEN EVOLUTION PERFORMANCE OF ALPHA-MANGNESESE OXIDE ELECTRODEPOSITED SUPER-ALIGNED CARBON NANO FIBERS UNDER AN INFLUENCE OF EXTERNAL MAGNETIC FIELD

Introduction

Over combustion of fossil fuel has induced significant environmental problems, such as global warming, extremely climate change, and serious air pollution (McDuffie et al., 2021) (Yao et al., 2020) (Beidaghy Dizaji et al., 2022). Generation, utilization, and storage of renewable energy have been advocated to address and solve these problems. Currently, MABs, FCs and supercapacitors, have been deeply explored and highly recommended because of their eminent efficiency (Z. Zhang et al., 2021) (Korberg et al., 2021). For example, theoretical energy density of the MABs is doubled than the traditional metal-ion batteries (MIBs), and bare metal (Li, Na, K, Zn, Al, Mg, Fe, etc.) can be set as anode for long term charging-discharging process without serious dendrites structure formation on anode side (Ling et al., 2021) (Pierini et al., 2021) (Y. Peng et al., 2022). OER device can be coupled with MABs for O_2 supplying (H. F. Wang & Xu, 2019). And, electrocatalytic behaviors of OER system can determine the rate capacity and long-term stability of the advanced electrochemical energy generation/storage device (Beall et al., 2021) (Xiong & Ivey, 2019). Similarly, hydrogen-based FCs is another open and green energy storage system, in which HER and OER device are respectively constructed on cathode and anode side, and H_2O is the only by-product (Kwan et al., 2021) (M. Singh et al., 2021). Especially, the by-product, in hydrogen-based FCs also can be recycled directly by OER system (Mardini & Bicer, 2021). However, compared with HER, a 2-steps electron transfer reaction, the OER is a more sluggish electron transfer processes, which needs higher energy inputting to make the reaction smoothly happen (Charles et al., 2021).

Conventionally, noble metal, such as Pt, Pd, Ru, Ir, and their oxides are the benchmark of high activity OER catalyst (Sun et al., 2021). Theoretically, the superior electrocatalytic performances of these materials were induced by the optimization between binding energy of the intermediates' adsorption and overpotential of the reaction (R. Wang et al., 2018). However, the high cost of noble metal is one of the obvious bottleneck for widespread applications (Jiang et al., 2022). Additionally, low stability under alkaline solution also limit the performance of the noble metal based catalyst (Oh et al., 2021). Currently, morphology, size, and composition modification method have been widely operated on the earth abundant transition metal oxides OER electrocatalyst, the most promising candidates of low-cost and high performance OER electrocatalyst, to improve electrochemical properties and corrosion resistance (Yuan et al., 2021).

Transition metal oxides hybridization has been highly preferred because the composition with mixed valence state often displayed low overpotential and high current density under the OER test (Hazarika et al., 2021). For instance, Shao et al. introduced a series of bi-transition metal decorated vanadate OER catalyst by inorganic metal salts precipitation (Shao et al., 2022). All fabricated materials, such as CoFe, NiFe, and NiCo bimetal decorated vanadate, exhibited excellent electrocatalytic activity and charge transfer kinetics. Especially, the NiFe co-hybridized catalyst has the most eminent performance, in which the lowest overpotential of 267 mV was obtained to approach the current density of 10 mA/cm^2, and the Tafel slope was as low as 38 mV/dec. Additionally, Zhou et al. adopted a high porous Ni and Fe co-participated foam by a simple electrodeposition method (Jianqing Zhou et al., 2021). To get a 10 mA/cm^2 current density, a significant low overpotential of 206 mV was only needed. To reach the current density of 100 mA/cm^2, only 265 mV overpotential applied, which value was eminently outperformed than the 346 mV of the RuO_2 benchmark.

Additionally, exotic non-metal elements decorated carbon based substrate has been considered due to its high specific area, electronic conductivity, and stability (Tang et al., 2022). Bare carbon material does not possess a good electrocatalytic activity because of low active sites. Non-metal element such as nitrogen, phosphorous, and sulfur are often hybridized with the host substrate (Ren et al., 2020) (Jing Yang et al., 2019) (T. Liu et al., 2018). For instance, Peng et al. invented a N doped hierarchical porous carbon plates by an novel enzyme pyrolysis strategy on raw wood chips (X. Peng et al., 2019). The crosslinked porous structure did not only improve stability but also the wettability of the material. The enzyme treated catalyst under 900°C calcination had an obvious higher current density value than RuO_2 control (X. Peng et al., 2019). In addition, Wang et al. fabricated a non-metal B, N, and F, tri-doped carbon nanofiber by electrospinning (Y. Wang et al., 2022). In the OER test, the optimized catalyst had a overpotential of 342 mV under the current density of 10 mV/cm^2, and the Tafel slope value was also as low as 63.6 mV/dec. Especially, by the directly utilization on an assembled MAB system, the electrocatalyst can drive a high capacity of 791.5 mAh/g, which value is obvious superior than a traditional noble metal associated electrode (720.0 mAh/g) (Y. Wang et al., 2022).

In this report, magnetic field were applied for O_2 boosting. For the experimental design, a special 2-electrodes system was utilized. According to current research, external magnetic field may not have obvious effect under lower working potential (C. Wei & Xu, 2022). So, to clearly detect the OER behaviors on the electrodeposited SA-CNFs, the applied potential was increased to 3.5 V. Under the test, SA-CNFs substrate supply a backbone to resist the destroy from bubbles generation under high working potential. On the other hand, α-MnO_2 was selected because it possess relatively high charge transfer rate and electrochemical stability from a 2 by 2 ‘open’ tunnel structure and di-oxo-bridge of Mn-O connection (H. H. Yang et al., 2022) (M. A. Khan et

al., 2022). To shorten the deposition time, relatively high deposition current and concentration of manganese salt was adopted for homogenously electrodeposition. Faster Mn^{2+} diffusion rate and oxidation process on the surface of SA-CNFs did not affect the uniformity of the MnO_2 particles and the alignment of carbon fibers.

Experimental

Material and agent

Polyacrylonitrile powder (PAN, Acros Organics, M_w = 150000), dimethylformamide (DMF, Acros Organics, 99.8%), nitride acid (HNO_3, J. T. Baker, 69%), manganese sulfide monohydrate ($MnSO_4 \cdot H_2O$, Acros Organic, >99%), sodium sulfide anhydrous (Na_2SO_4, Acros Organics, 99%), potassium hexacyanoferrate (III) ($K_3Fe(CN)_3$, Sigma Aldrich, >99%), potassium chloride (KCl, Acros Organic, extra pure), and KOH (Acros Organics, ≥85%) were applied without any further purification.

Fabrication of SA-CNFs

The SA-CNFs was fabricated based on a method in our previous report (Z. Zeng et al., 2018) (Y. Liu et al., 2018), and 10% (wt.) PAN dissolved by and 90% (wt.) DMF solvent was mixed homogenously. After that, the solution was removed carefully into a 10 mL syringe with an assembling of a steel needle tip. For the electrospinning setting up, distance between needle tip and the collector was 15 cm with an application of 18 KV high voltage, and injection rate (1.4 mL/hour) of the precursor solution was controlled by a syringe pump (NE-300, Southpointe Surgical Supply, Inc.); moreover, speed of the collector wheel was maintained under 2000 rpm. 5 hours later, the original aligned fibers were collected. Then, stabilization and carbonization were completed separately for 6 hours (280 °C) and 1 hour (1200 °C) with different heating rate of 1

°C/min (air flow) and 5 °C/min (N_2 flow), respectively. The treated fiber was rinsed by deionized (DI) water and moved into oven for drying under 80°C for 4 hours. Then, 4M HNO_3 was used for functionalization, which process was under 25°C for 24 hours. Eventually, the treated fiber was cleaned by DI water and dried in the oven again under 80°C for 4 hours.

α-MnO_2 electrodeposition

α-MnO_2 was electrodeposited on a rectangular shape (2×1 cm^2) cut SA-CNFs by galvanostatic method with a current of 4 mA on a bio-logic VMP3 electrochemical workstation. The SA-CNFs was taped on an Au coated electrode by conductive carbon glue (Ted Pella, Inc.); and Pt wire was used for counter electrode. Electrolyte was based on a 0.1 M $MnSO_4$•H_2O aqueous solution with the blending of 0.1 M Na_2SO_4 stabilizer. Deposition time was controlled as 5, 10, and 15 min, and the corresponding sample are marked by 5-MnO_2@SA-CNFs, 10-MnO_2@SA-CNFs, and 15-MnO_2@SA-CNFs, respectively.

Material Characterization

X-ray diffraction (XRD, Agilent Technologies Oxford Germini X-Ray Diffractometer), Field-emission scanning electron microscopy (FESEM, Carl Zeiss Auriga Microscope), Energy dispersive X-ray spectroscopy (EDX, Hitachi S-4800-I), and X-ray photoelectron spectroscopy (XPS, Thermo Scientific Escalab) were applied for crystallinity investigation, morphology detection, and elemental analysis.

Electrochemical analysis

Electrochemical behaviors of the electrodeposited MnO_2@SA-CNFs were recorded by the biologic VMP3 electrochemical workstation. O_2 generation was estimated based on a 2 electrodes system, in which platinum wire was used as counter electrode (CE), SA-CNFs with and without α-MnO_2 deposition was applied as working electrode (WE) under the electrolyte of 1 M KOH

aqueous solution. The scan rate and working potential were set as 200 mV/s and 3.5 V, respectively. Before each scan, N_2 was pumped into the electrolyte for 20 min purging.

Magnetic field was created by Helmholtz coil (3B Scientific). Intensity of the external magnetic field was adjusted through the current, passing through the wire of the coil. Relation between the magnetic field and current was obtained by Eq.5.1, where the parameter of μ_o, n, R, I, and B represent magnetic field constant (μ_o= 1.257×10^{-6} T·m/A), number of turns of the individual coil (n=124), radius of the coil (R=150 mm), magnitude of the applied current, and intensity of the created magnetic field (Y. Liu et al., 2018). The schematic structure of the electrochemistry testing set was displayed in **Figure 5.1**, in which the fiber surface was kept parallelly with the plane of the coil.

The electrochemical impedance spectrum (EIS) tests were organized based on a 3 electrodes system. Platinum wire and saturated Ag/AgCl were utilized as counter and reference electrodes, individually. 5 mM $K_3Fe(CN)_3$ with the mixing of 0.1 M KCl was used as electrolyte. Magnitude of the oscillation voltage was under 10 mV versus the open circle voltage (OCV). Similarly, N_2 was also pumped into the electrolyte 20 min for purging before each scan.

$$B = 0.72\frac{\mu_o nI}{R} \tag{5.1}$$

Figure 5.1. Schematic description of the magnetic field influenced electrochemical working station setup.

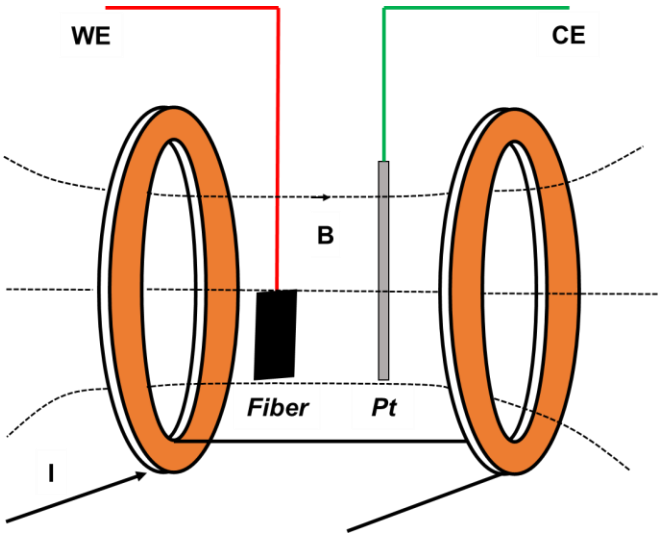

Result and discussion

Figure 5.2. XRD diagrams of the MnO_2@SA-CNFs samples with 5-, 10-, and 15-min deposition time.

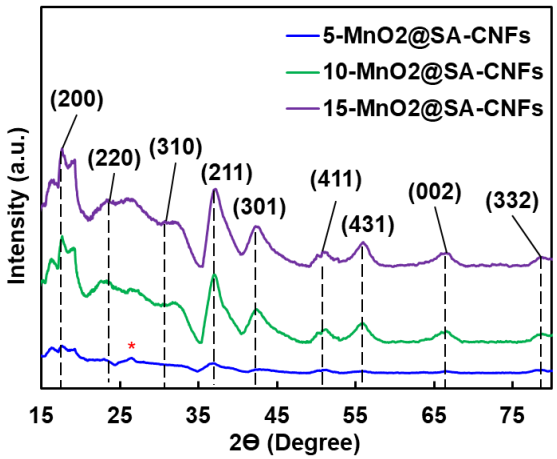

Figure 5.2 displays the XRD patterns of the 5, 10, and 15 min deposited SA-CNFs. The identical diffraction peaks became shaper and more outstanding with the increment of deposition time. The characteristic plane of (200), (220), (310), (211), (301), (411), (431), (002) and (332) are defined by the diffraction angle of 17.67, 23.68, 30.86, 37,22, 42.12, 50.80, 56.39, 66.62, and 78.61, indicating the property of α-MnO_2 (Y. Liu et al., 2018) (Xu Gao et al., 2020). Furthermore, the peak at 2Θ angle of 26.91° which marked by * in **Figure 5.2**, representing (002) plane of the graphitized SA-CNFs substrate, gradually disappeared with the addition of deposition time (Xie et al., 2022). The phenomenon demonstrated that the aligned fiber was totally and homogenously covered by the α-MnO_2 particle.

Figure 5.3. SEM images (3500×) of bare SA-CNFs **(a)**, 5-MnO_2@SA-CNFs **(b)**, 10-MnO_2@SA-CNFs **(c)**, 15-MnO_2@SA-CNFs **(d)**.

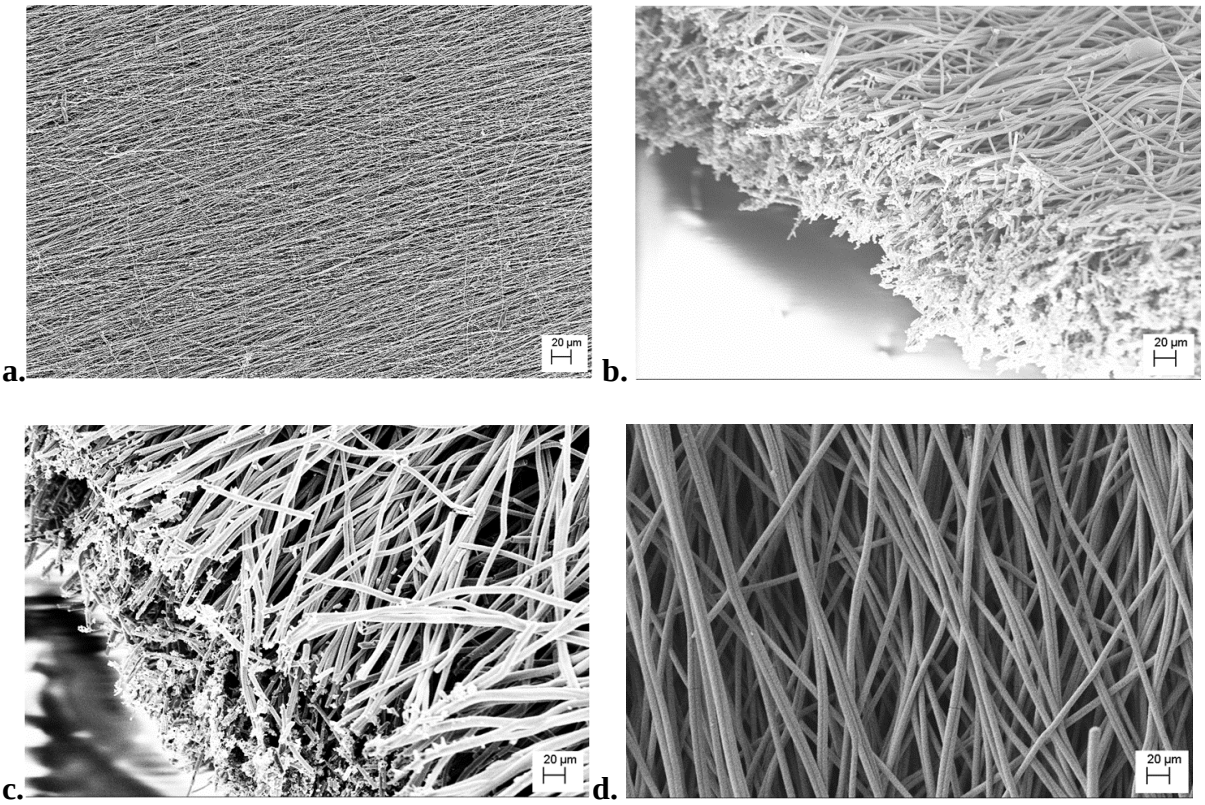

The morphology of bare and α-MnO_2 deposited SA-CNFs were exhibited in SEM images. **Figure 5.3** and **Figure C. S5.1** present the SEM image of SA-CNFs, 5-MnO_2@SA-CNFs, 10-MnO_2@SA-CNFs, and 15-MnO_2@SA-CNFs at low (3500×) and high (38600×) magnification. Briefly, carbon fibers were aligned properly, and the alignment of carbon fibers was not varied after the electrodeposition. Moreover, single fiber became more identical with the increment of deposition time, illustrating size increase after deposition. According to **Figure C. S5.1**, the distribution of α-MnO_2 in 10-MnO_2@SA-CNFs and 15-MnO_2@SA-CNFs became denser than the 5-MnO_2@SA-CNFs. By the assistance of ImageJ software, thickness of different samples was measured. The average size distribution was showed in **Table C S5.1** and **Figure C S5.2**. According to the data, thickness enhances significantly with electrodeposition time. After 5, 10, and 15 min, the thickness of the fiber is almost 1, 3, and 5 times' larger than the bare SA-CNFs, respectively.

Figure C. S5.3 displayed the EDX elemental distribution maps of different samples. In SA-CNFs, C signal is strong, O signal is relative weak, which O element may belong to the -OH and/or -COOH groups. After electrodeposition, Mn and O signal became more obvious, and the elemental distribution is also homogenous. Simultaneously, C signal was weakened gradually with the addition of deposition time, indicating that uniformly α-MnO_2 particles coverage. The atomic ratio of C, O, and Mn on different sample are displayed in **Table C. S5.2**. Similarly, the percentage of C is significant high in bare SA-CNFs. The ratio of Mn to O under the 5-, 10-, and 15-MnO_2@SA-CNFs is close to 1:2, illustrating the desired stoichiometry composition.

Figure 5.4. XPS spectrum of bare SA-CNFs and electrodeposited samples under different time.

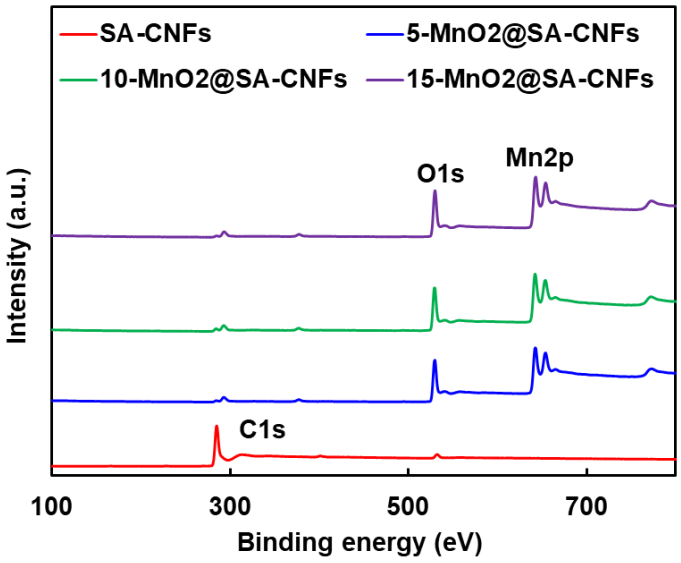

The compositions in different samples were also checked by XPS. In bare SA-CNFs, the broader peak at 285.40 eV indicates the coexistence of graphitic carbon, C-O-H, and O=C-O configuration (see **Figure 5.4** and **Figure C. S5.4**) (Kang et al., 2022). The intensity of the C1s peak was quenched and had a negatively shifting to 284.5 eV after electrodeposition because of the coverage of α-MnO_2 layer, and only the graphitic carbon peak left. Under the α-MnO_2 deposited sample, an ambiguous C1s peak, which was centered at 293.1 eV, was induced by the π – π* satellite peak (see **Figure C. S5.4**) (Pinjari et al., 2022). The peak in O1s spectra (see **Figure 5.4** and **Figure C. S5.4**) of the bare carbon fiber, locating at the binding energy of 532.5 eV, also figure out the O element in both of the C-O-H and O=C-O configuration (Rais et al., 2021). After electrodeposition, O1s binding energy has a negatively shifting to 529.6 eV and peak also became more significant than the bare SA-CNFs because of the formation of homogenous Mn-O-Mn structure covering on the surface of aligned fiber (Jiacheng Zhou et al., 2019). In **Figure 5.4**, the Mn2p splitting orbital structure, was defined by the binding energy of 642.5 and 654 eV (Ji et al.,

2022). Additionally, the binding energy position and intensity of the Mn2p deconvoluted peaks do not have obvious variation with the change of deposition time (see **Figure C. S5.4**).

In **Figure 5.5**, electrocatalytic performance can be directly investigated based on the variation of current. For the bare SA-CNFs, there was no current change under the magnetic field. However, current values had obvious variation in α-MnO_2 deposited samples, and the variations were more significant with the increase of deposition time. Additionally, in **Figure 5.5a**, a smooth polarization curve displayed the electrochemical performance of the SA-CNFs electrode, however, several tiny plateaus can be found in the electrodeposited samples, especially, LSV line had obvious slope change when working potential was added above to 2 V. The phenomenon may relate with the intrinsic rule of the OER process. According to the former research by Fortunelli et al., the accumulation and transferring of intermediates, such as -OH, -O, and -OOH, gradually happen with the increment of working potential, and each step is linearly correlated (Fortunelli et al., 2015). The obvious current change above 2 V might be induced by the release of significant amount of O_2 after large amount intermediates' transformation.

To easily detect the OER performance under different samples, current value at 3.5 V were summarized in **Figure 5.6**. Total values' change on the 5, 10, and 15 mins' electrodeposited SA-CNFs was 2.54, 6.03, and 8.16 mA, respectively. Therefore, the increase of the intensity of magnetic field can boost generation of O_2. To furtherly demonstrate the influence of the applied magnetic field, OER performance was also monitored by the 15-MnO_2@SA-CNFs electrode without the influence of magnetic field. However, in this condition, the OER current does not have any change within the scans (see **Figure C. S5.5**).

Figure 5.5a. LSV diagram of bare SA-CNFs; **b.** 5-MnO_2@SA-CNFs; **c.** 10-MnO_2@SA-CNFs; **d.** 15-MnO_2@SA-CNFs.

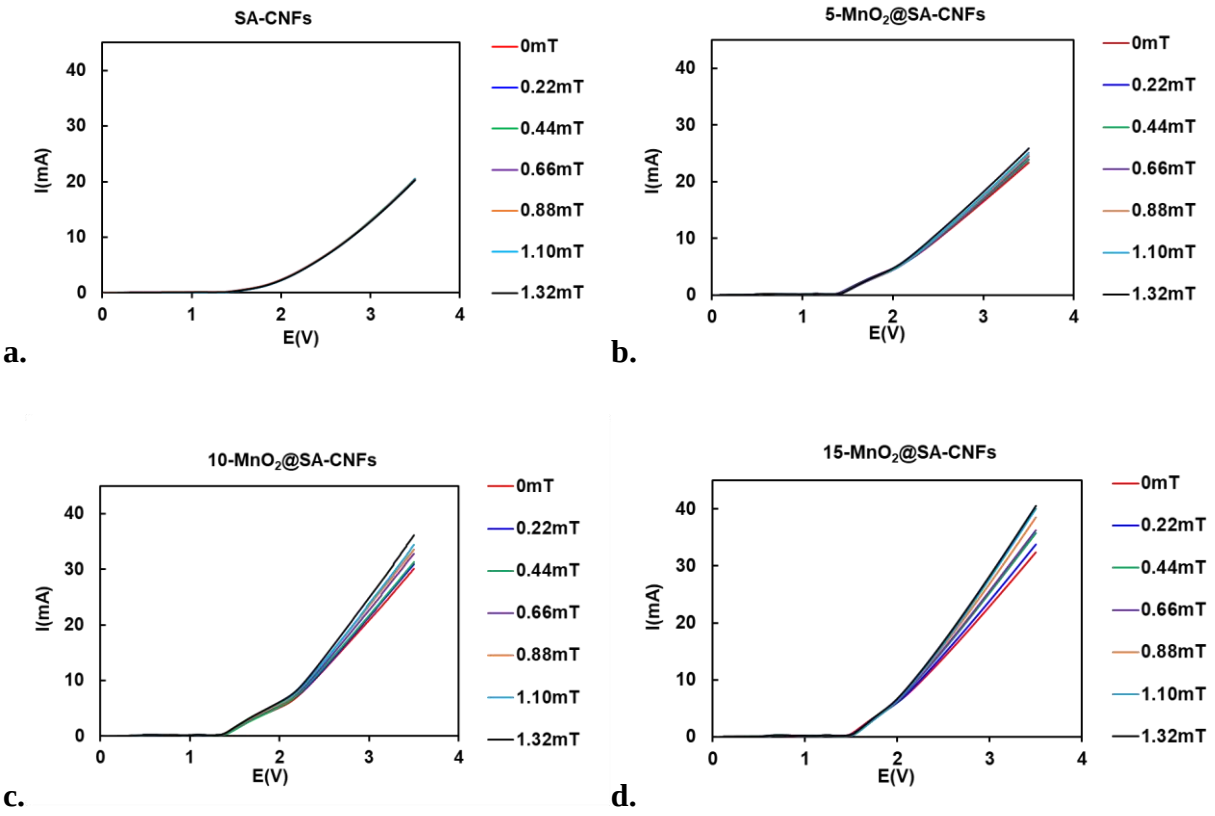

Figure 5.6. 3-dimentional chart of the OER performance of different samples.

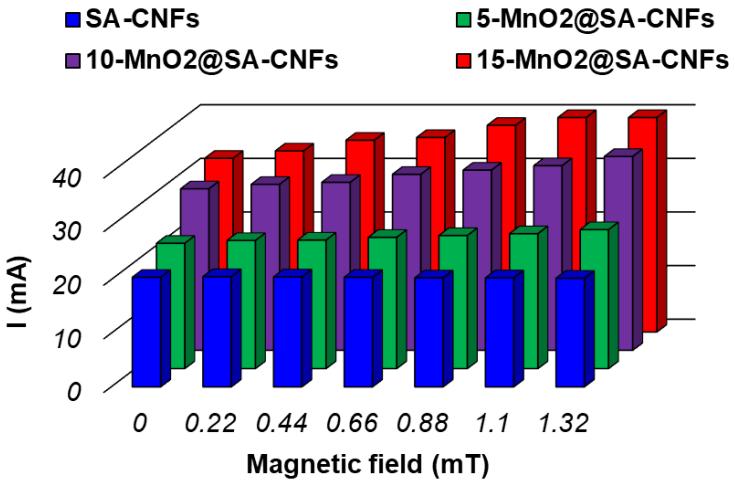

Figure 5.7a. Magnetic field influenced Nyquist plot of bare SA-CNFs; **b.** 5-MnO_2@SA-CNFs; **c.** 10-MnO_2@SA-CNFs; **d.** 15-MnO_2@SA-CNFs (insert represents the equivalent circuit).

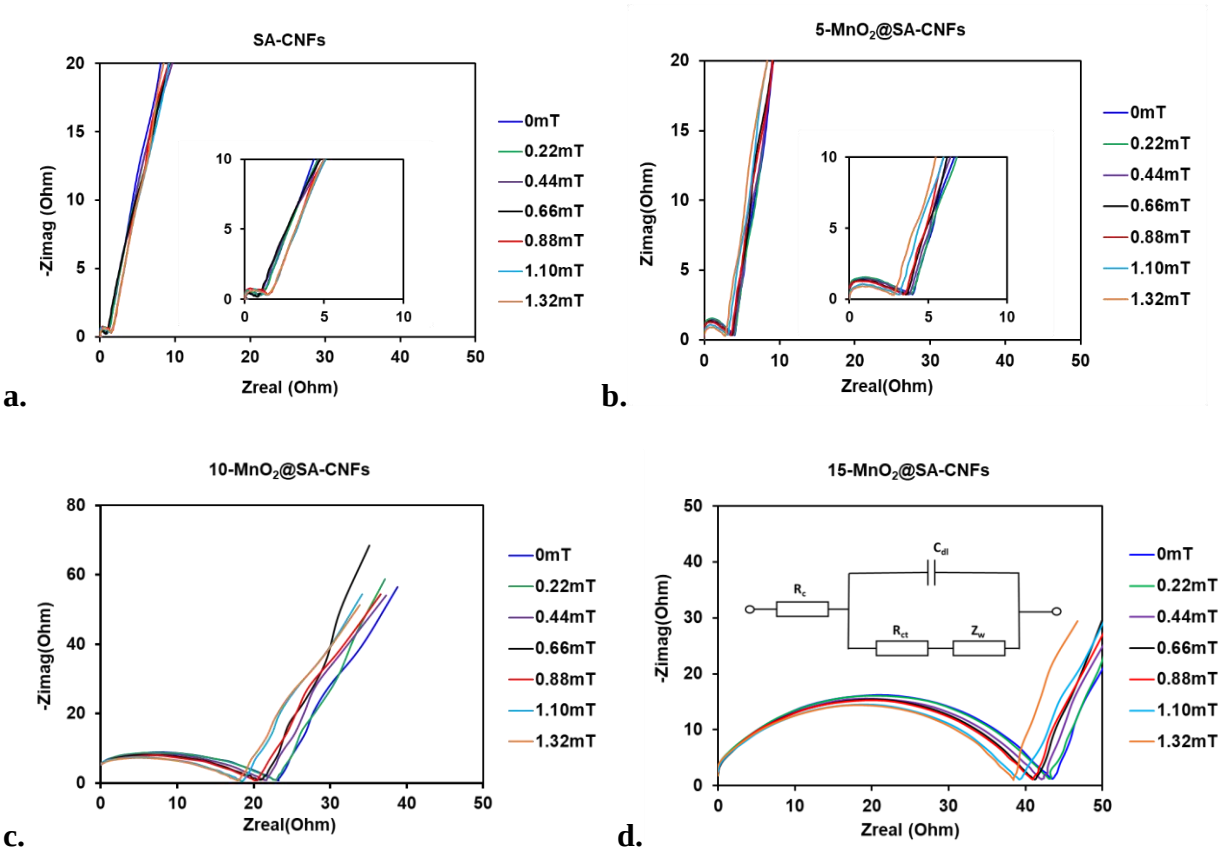

Figure 5.8. Summary of the charge transfer resistance of different samples.

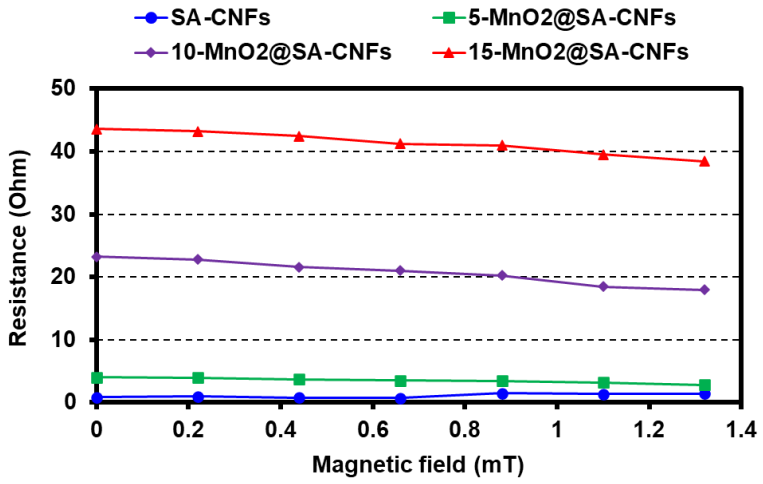

To furtherly confirm the influence of the magnetic field on charge transfer kinetics, charge transfer resistance was estimated by EIS test with the addition of magnetic field. Charge transfer process was observed based on redox reaction between Fe^{2+} and Fe^{3+}. Nyquist plots and the equivalent circuit are exhibited in **Figure 5.7**, and the charge transfer resistance were also summarized in **Figure 5.8**. For the equivalent circuit (see the insert of **Figure 5.7d**), parameter of R_c, R_{ct}, and Z_w represent contact resistance of electrolyte, charge transfer resistance at the interface of electrode and electrolyte, and Warburg impedance, respectively. And the C_{dl} is double layer capacitance which is defined by constant phase element (Tajdid Khajeh et al., 2020). Charge transfer resistance represents by the semicircle of the Nyquist plots. In general, the resistance increased with deposition time because of the thickness increasing which can reduce electronic conductivity. The resistance did not have variation under the external magnetic field on SA-CNFs electrode (see **Figure 5.7** and **5.8**). The resistance changes between the minimum and maximum strength of applied magnetic field was also summarized in **Figure 5.9**. It can be observed that the fibers after 10 and 15 min electrodeposition had an obvious distinction; however, the value of 10-MnO_2@SA-CNFs was slightly larger than the 15-MnO_2@SA-CNFs, illustrating a negative effect on electron transfer rate by the increasing of thickness, and α-MnO_2 is not a super electron conductive material (H. J. Lee et al., 2022).

Figure 5.9. Summary of the charge transfer resistance variation between the minimum and maximum intensity of external magnetic field.

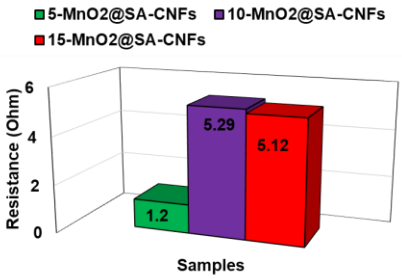

According to our previous report, the magnetic field's influence can be explained by the Transition State Theory (TST). With the adoption of magnetic field, degeneracy on unpaired electron of the transition metal/oxides can optimizes the activation energy under an electron transfer reaction (Z. Zeng et al., 2018) (Z. Zeng et al., 2017). And the electron transfer process of the MnO_2 catalyst under the OER test had been studied and approved by current research that oxidation state of Mn have a temporarily variation during the hydroxylation (MO – MOOH) and deprotonation (MOOH – O_2) process, and the electron configuration of the Mn^{4+} changes from $[Ar]3d^3$ to $[Ar]3d^2$, then goes back to $[Ar]3d^3$ at the ending of OER (Tripkovic et al., 2018).

Theoretically, activation energy can be described in Eq. 5.2, in which T is the absolute temperature, and other parameters, such as ΔG_o, ΔH_o, and ΔS_o, are the variation of Gibbs free energy, enthalpy, and entropy of the redox reaction (Z. Zeng et al., 2018) (Z. Zeng et al., 2017). With the operation of external magnetic field, entropy and enthalpy can be redefined by Eq. 5.3 & 5.4, respectively. In that case, electron transfer rate k_o in Eq. 5.5 (without magnetic field) is refreshed by Eq. 5.6. In Eq. 5.6, the parameter of ΔH_m can also be expressed by Zeeman energy of $-gHS_p\beta$, in which the g, H, S_p and β represent magnetic response to an applied magnetic field, intensity of the external magnetic field, electron spin, and Bohr magneton, correspondingly (Z. Zeng et al., 2018). Finally, reaction rate of the OER is facilitated by the reduced activation energy. Additionally, other study also points out that the movement of electrons and charged ions near the surface of fiber may induce a current convection with the effect of Lorentz force, providing a positive effect on OER performance, and the Lorentz force introduced charged ions and electron perturbation may also increase the mass diffusion rate near the fiber surface (Yuanyuan Zhang et al., 2022).

$$\Delta G_o = \Delta H_o - T\Delta S_o \tag{5.2}$$

$$\Delta H_o^* = \Delta H_o + \Delta H_m \quad (5.3)$$

$$\Delta S_o^* = \Delta S_o + \Delta S_m \quad (5.4)$$

$$k_o = A\exp\left[\frac{\Delta S_o}{k_b}\right]\exp[-\frac{\Delta H_o}{k_b T}] \quad (5.5)$$

$$k_m = A\exp\left[\frac{\Delta S_o}{k_b}\right]\exp\left[\frac{\Delta S_m}{k_b}\right]\exp[-\frac{\Delta H_o}{k_b T}]\exp\left[-\frac{\Delta H_m}{k_b T}\right] \quad (5.6)$$

Conclusion

In this study, SA-CNFs was fabricated by a well-designed electrospinning method, and α-MnO_2 was homogenously electrodeposited on the surface of the fiber. The SA-CNFs not only support a bone structure for the uniform MnO_2 deposition, but also provide high electrical conductivity for the electron transfer. OER performance of the α-MnO_2@SA-CNFs was investigated under magnetic fields. The electrocatalytic performance was determined by the magnitude of the generated current. A simple homemade 2-electrodes system was preferred in this study instead of a more complex 3-electrodes system. The fabricated electrode has high stability so that the electrode was not twisted and peeled easily by the generated gas under high working potential. Because of the reduction of activation energy of the OER process by the influence of magnetic field, O_2 generation and charge transfer kinetics was boosted.

CHAPTER VI: CONCLUSION

The fundamental goal of this research was to explore the low time and energy consumption CuS and In_2S_3 fabrication way. And the 'core-shell' installed NPs were also constructed under the microwave associated solvothermal strategy. Compared with traditional hydrothermal, solvothermal, or chemical vapor deposition way, the applied strategy is 'greener'. Additionally, with the assistance of the device, the synthesis process became easier on handling, especially, more effective because electromagnetic wave can be directly act on the homogenously blended solid – liquid precursors. On the other hand, photocatalytic performances of the synthesized NPs were investigated based on the degradation of MB and MO aqueous solution. Simultaneously, the electrocatalytic behaviors of the NPs were also detected and analyzed on OER and ORR tests.

In Chapter II, precursors selection, devices setting up, and parameters during fabrication were explained step by step. NPs' characterization was based on microstructural examination, elemental analysis, and optical properties investigation. XRD, SEM, HRTEM, and SAED were utilized for the comprehensive study of crystal configuration and elemental distribution, Oxidation state were checked by the EDX and XPS. Optical properties were detected by ultraviolet (UV)-visible spectrometer. Simultaneously, the charge carriers' recombination rate was estimated by a photoluminescence spectrometer. In this study, light absorption intensity was only focused on UV and visible light region. The absorption ability at the near infrared region (NIR) also needs to be concerned to make sure that NPs can be applied on the area of cancer thermal therapy. On the other hand, the NPs' characterization was also the experimental based. To furtherly explore physical properties, density function theory (DFT) dependent theoretical computation is also necessary.

Chapter III focused on the photodegradation performance of fabricated NPs on MB and MO dyes. Rather than utilized a high-power light source (~300 W), the potable blue light generator (5 – 500 mW) was applied with an assistance of unique testing system. Light beam can be focused directly on the surface of photocatalysts. With a installation of high-speed stirring plate, generated heat can be removed effectively from the solution. Because of the reduced bandgap energy and optimized charge carrier pairs' recombination rate, the 10wt% CuS core-shell hybridized NPs has the highest performance on MB and MO dyes' photodegradation. However, the photocatalytic activity should be observed under the irradiation of UV or natural light. On the other hand, the influence of working temperature, pH values, and concentration of dyes also need to be investigated.

Chapter IV mainly discussed the electrocatalytic activity of the NPs. Electrocatalysis of OER and ORR was exanimated. Based on current references and studies, catalytic behaviors of metal sulfides have not been sufficiently provided. To eliminate ununiform mass diffusion rate, rotating disk electrode (RDE) was adopted. LSV curves and Tafel plots were utilized to identify activity of different NPs. It was approved that the 10wt% CuS core-shell NPs also displayed outstanding catalytic performance on both OER and ORR because of the modified bandgap structure. However, the strong semiconductor behaviors limited the charge transfer kinetics, so, the value of OER current density at lower potential was not obvious as same as the performance in ORR test. Our future goal is to improve the electrocatalytic activity of the synthesized NPs based on the microwave associate method. Atoms, coming from other dopants, such as precious metals, transition metals, and their corresponding oxides, should be introduced and combined with current core-shell configuration.

Chapter V illustrated the magnetic influenced OER electrocatalytic performance based on α-MnO_2 electrodeposited SA-CNFs. With the addition of magnetic field, reaction rate of OER was boosted under an accelerated charge transfer process. With the enhancement of electrodeposition time, variation of OER current became more obvious. The high thickness of the SA-CNFs backbone can protect the working electrode from the corrosion by generated bubbles; however, it also limited the electron transfer rate and kinetics, so the generated current was small under low working potential. In that case, the next goal for us is the electronic conductivity enhancement by an optimized electrospinning method. And the thickness of working electrode material should be reduced without weaken the chemical and physical stability.

REFERENCES

Afroz, S., Haque, M. M., Fazlul Haque, A. K., Jakubassa-Amundsen, D. H., Patoary, M. A. R., Shorifuddoza, M., Khandker, M. H., & Alfaz Uddin, M. (2020). Elastic scattering of electrons and positrons from 115In atoms over the energy range 1 eV–0.5 GeV. *Results in Physics*, *18*(May), 103179. https://doi.org/10.1016/j.rinp.2020.103179

Ain, N. ul, Zia-ur-Rehman, Aamir, A., Khan, Y., Rehman, M. ur, & Lin, D. J. (2020). Catalytic and photocatalytic efficacy of hexagonal CuS nanoplates derived from copper(II) dithiocarbamate. *Materials Chemistry and Physics*, *242*(August 2016), 122408. https://doi.org/10.1016/j.matchemphys.2019.122408

Al-Mamun, M. R., Kader, S., Islam, M. S., & Khan, M. Z. H. (2019). Photocatalytic activity improvement and application of UV-TiO_2 photocatalysis in textile wastewater treatment: A review. *Journal of Environmental Chemical Engineering*, *7*(5). https://doi.org/10.1016/j.jece.2019.103248

Alhammadi, S., Mun, B. G., Gedi, S., Minnam Reddy, V. R., Rabie, A. M., Sayed, M. S., Shim, J. J., Park, H., & Kim, W. K. (2021). Effect of silver doping on the properties and photocatalytic performance of In_2S_3 nanoparticles. *Journal of Molecular Liquids*, *344*, 117649. https://doi.org/10.1016/j.molliq.2021.117649

Amato, C., Devillers, S., Calas, P., Delhalle, J., & Mekhalif, Z. (2008). New semifluorinated dithiols self-assembled monolayers on a copper platform. *Langmuir*, *24*(19), 10879–10886. https://doi.org/10.1021/la800496d

An, L., Li, Y., Luo, M., Yin, J., Zhao, Y. Q., Xu, C., Cheng, F., Yang, Y., Xi, P., & Guo, S. (2017). Atomic-Level Coupled Interfaces and Lattice Distortion on CuS/NiS_2 Nanocrystals Boost Oxygen Catalysis for Flexible Zn-Air Batteries. *Advanced Functional Materials*, *27*(42), 1–9. https://doi.org/10.1002/adfm.201703779

Arslan, I., Balcioglu, I. A., & Tuhkanen, T. (1999). Advanced oxidation of synthetic dyehouse effluent by O_3, H_2O_2/O_3 and H_2O_2/uv processes. *Environmental Technology (United Kingdom)*, *20*(9), 921–931. https://doi.org/10.1080/09593332008616887

Ayodhya, D., & Veerabhadram, G. (2018). A review on recent advances in photodegradation of dyes using doped and heterojunction based semiconductor metal sulfide nanostructures for environmental protection. *Materials Today Energy*, *9*, 83–113. https://doi.org/10.1016/j.mtener.2018.05.007

Bai, L., Wang, X., Tang, S., Kang, Y., Wang, J., Yu, Y., Zhou, Z. K., Ma, C., Zhang, X., Jiang, J., Chu, P. K., & Yu, X. F. (2018). Black Phosphorus/Platinum Heterostructure: A Highly Efficient Photocatalyst for Solar-Driven Chemical Reactions. *Advanced Materials*, *30*(40). https://doi.org/10.1002/adma.201803641

Balakrishnan, A., Groeneveld, J. D., Pokhrel, S., & Mädler, L. (2021). Metal Sulfide Nanoparticles: Precursor Chemistry. *Chemistry - A European Journal*, *27*(21), 6390–6406. https://doi.org/10.1002/chem.202004952

Baruah, J. M., Kalita, S., & Narayan, J. (2019). Green chemistry synthesis of biocompatible ZnS quantum dots (QDs): their application as potential thin films and antibacterial agent. *International Nano Letters*, *9*(2), 149–159. https://doi.org/10.1007/s40089-019-0270-x

Basu, M., Garg, N., & Ganguli, A. K. (2014). A type-II semiconductor (ZnO/CuS heterostructure) for visible light photocatalysis. *Journal of Materials Chemistry A*, *2*(20), 7517–7525. https://doi.org/10.1039/c3ta15446g

Beall, C. E., Fabbri, E., & Schmidt, T. J. (2021). Perovskite Oxide Based Electrodes for the Oxygen Reduction and Evolution Reactions: The Underlying Mechanism. *ACS Catalysis*, *11*(5), 3094–3114. https://doi.org/10.1021/acscatal.0c04473

Beidaghy Dizaji, H., Zeng, T., Hölzig, H., Bauer, J., Klöß, G., & Enke, D. (2022). Ash transformation mechanism during combustion of rice husk and rice straw. *Fuel*, *307*(July 2021). https://doi.org/10.1016/j.fuel.2021.121768

Bhatnagar, A., & Jain, A. K. (2005). A comparative adsorption study with different industrial wastes as adsorbents for the removal of cationic dyes from water. *Journal of Colloid and Interface Science*, *281*(1), 49–55. https://doi.org/10.1016/j.jcis.2004.08.076

Bo, Z., Wen, Z., Kim, H., Lu, G., Yu, K., & Chen, J. (2012). One-step fabrication and capacitive behavior of electrochemical double layer capacitor electrodes using vertically-oriented graphene directly grown on metal. *Carbon*, *50*(12), 4379–4387. https://doi.org/10.1016/j.carbon.2012.05.014

Bocchetta, P., Sánchez, C. R., Taurino, A., & Bozzini, B. (2016). Accurate Assessment of the Oxygen Reduction Electrocatalytic Activity of Mn/Polypyrrole Nanocomposites Based on Rotating Disk Electrode Measurements, Complemented with Multitechnique Structural Characterizations. *Journal of Analytical Methods in Chemistry*, *2016*, 1–16. https://doi.org/10.1155/2016/2030675

Byeon, J. H., & Kim, Y. W. (2014). Au-TiO_2 nanoscale heterodimers synthesis from an ambient spark discharge for efficient photocatalytic and photothermal activity. *ACS Applied Materials and Interfaces*, *6*(2), 763–767. https://doi.org/10.1021/am405004a

Casalongue, H. S., Kaya, S., Viswanathan, V., Miller, D. J., Friebel, D., Hansen, H. A., Nørskov, J. K., Nilsson, A., & Ogasawara, H. (2013). Direct observation of the oxygenated species during oxygen reduction on a platinum fuel cell cathode. *Nature Communications*, *4*(May). https://doi.org/10.1038/ncomms3817

Chaki, S. H., Deshpande, M. P., & Tailor, J. P. (2014). Characterization of CuS nanocrystalline thin films synthesized by chemical bath deposition and dip coating techniques. *Thin Solid Films*, *550*, 291–297. https://doi.org/10.1016/j.tsf.2013.11.037

Chan, W. T., Leung, A. P. K., Mao, X. L., & Russo, R. E. (1998). Effects of gas environment on picosecond laser ablation. *Applied Surface Science*, *127–129*(22), 269–273. https://doi.org/10.1016/S0169-4332(97)00641-7

Charles, V., Anumah, A. O., Adegoke, K. A., Adesina, M. O., Ebuka, I. P., Gaya, N. A., Ogwuche, S., & Yakubu, M. O. (2021). Progress and challenges pertaining to the earthly-abundant electrocatalytic materials for oxygen evolution reaction. *Sustainable Materials and Technologies*, *28*, e00252. https://doi.org/10.1016/j.susmat.2021.e00252

Chen, B., Chang, S., Li, D., Chen, L., Wang, Y., Chen, T., Zou, B., Zhong, H., & Rogach, A. L. (2015). Template Synthesis of $CuInS_2$ Nanocrystals from In_2S_3 Nanoplates and Their Application as Counter Electrodes in Dye-Sensitized Solar Cells. *Chemistry of Materials*, *27*(17), 5949–5956. https://doi.org/10.1021/acs.chemmater.5b01971

Chen, L., Yang, G., Wei, X., Xu, H., & Jin, S. (2022). One-pot soft integration fabrication of graphene-induced phase transition to form dimension control contact In_2S_3/G heterojunction hybrids for enhancing visible photocatalytic purification performances. *Journal of Alloys and Compounds*, *895*, 162589. https://doi.org/10.1016/j.jallcom.2021.162589

Chen, Q., Wu, S., & Xin, Y. (2016). Synthesis of Au-CuS-TiO2 nanobelts photocatalyst for efficient photocatalytic degradation of antibiotic oxytetracycline. *Chemical Engineering Journal*, *302*, 377–387. https://doi.org/10.1016/j.cej.2016.05.076

Chen, Y. F., Duan, X., Li, J., Liu, W., Ren, S., Yang, J., & Liu, Q. (2021). Hydrothermal synthesis of Ca doped β-In_2S_3 for effective dyes degradation. *Advanced Powder Technology*, *32*(6), 1881–1890. https://doi.org/10.1016/j.apt.2021.03.042

Cho, K., Han, S.-H., & Suh, M. P. (2016). Copper-Organic Framework Fabricated with CuS Nanoparticles: Synthesis, Electrical Conductivity, and Electrocatalytic Activities for Oxygen Reduction Reaction. *Angewandte Chemie*, *128*(49), 15527–15531. https://doi.org/10.1002/ange.201607271

Conesa, J. C. (2022). Sulfide-based photocatalysts using visible light, with special focus on In_2S_3, SnS_2 and $ZnIn_2S_4$. In *Catalysts* (Vol. 12, Issue 1). https://doi.org/10.3390/catal12010040

Cui, H., Dong, S., Wang, K., Luan, M., & Huang, T. (2021). Synthesis of a novel Type-II In_2S_3/Bi_2MoO_6 heterojunction photocatalyst: Excellent photocatalytic performance and degradation mechanism for Rhodamine B. *Separation and Purification Technology*, *255*(September 2020), 117758. https://doi.org/10.1016/j.seppur.2020.117758

Cui, Y., Lin, C., Li, M., Zhu, N., Meng, J., & Zhao, J. (2022). $CuWO_4$/CuS heterojunction photocatalyst for the application of visible-light-driven photodegradation of dye pollutions. *Journal of Alloys and Compounds*, *893*, 162181. https://doi.org/10.1016/j.jallcom.2021.162181

Das, P., Tantubay, K., Ghosh, R., Dam, S., & Baskey (Sen), M. (2021). Transformation of CuS/ZnS nanomaterials to an efficient visible light photocatalyst by 'photosensitizer' graphene and the potential antimicrobial activities of the nanocomposites. *Environmental Science and Pollution Research*, *28*(35), 49125–49138. https://doi.org/10.1007/s11356-021-14068-1

Deng, X., Li, K., Cai, X., Liu, B., Wei, Y., Deng, K., Xie, Z., Wu, Z., Ma, P., Hou, Z., Cheng, Z., & Lin, J. (2017). A Hollow-Structured CuS@Cu_2S@Au Nanohybrid: Synergistically Enhanced Photothermal Efficiency and Photoswitchable Targeting Effect for Cancer Theranostics. *Advanced Materials*, *29*(36). https://doi.org/10.1002/adma.201701266

Devaraju, M. K., & Honma, I. (2012). Hydrothermal and solvothermal process towards development of $LiMPO_4$ (M = Fe, Mn) nanomaterials for lithium-ion batteries. *Advanced Energy Materials*, *2*(3), 284–297. https://doi.org/10.1002/aenm.201100642

Do, J. Y., Chava, R. K., Kim, S. K., Nahm, K., Park, N. K., Hong, J. P., Lee, S. J., & Kang, M. (2018). Fabrication of core@interface:shell structured CuS@$CuInS_2$:In_2S_3 particles for highly efficient solar hydrogen production. *Applied Surface Science*, *451*, 86–98. https://doi.org/10.1016/j.apsusc.2018.04.172

El-Hout, S. I., El-Sheikh, S. M., Gaber, A., Shawky, A., & Ahmed, A. I. (2020). Highly efficient sunlight-driven photocatalytic degradation of malachite green dye over reduced graphene oxide-supported CuS nanoparticles. *Journal of Alloys and Compounds*, *849*, 156573. https://doi.org/10.1016/j.jallcom.2020.156573

El Habnouni, S., Darcos, V., Garric, X., Lavigne, J. P., Nottelet, B., & Coudane, J. (2011). Mild methodology for the versatile chemical modification of polylactide surfaces: Original combination of anionic and click chemistry for biomedical applications. *Advanced Functional Materials*, *21*(17), 3321–3330. https://doi.org/10.1002/adfm.201100412

Emil, E., & Gürmen, S. (2018). Estimation of yttrium oxide microstructural parameters using the Williamson–Hall analysis. *Materials Science and Technology (United Kingdom)*, *34*(13), 1549–1557. https://doi.org/10.1080/02670836.2018.1490857

Feng, J., Yang, Z., He, S., Niu, X., Zhang, T., Ding, A., Liang, H., & Feng, X. (2018). Photocatalytic reduction of Uranium(VI) under visible light with Sn-doped In2S3 microspheres. *Chemosphere*, *212*, 114–123. https://doi.org/10.1016/j.chemosphere.2018.08.070

Ferraz, E. R. A., Grando, M. D., & Oliveira, D. P. (2011). The azo dye Disperse Orange 1 induces DNA damage and cytotoxic effects but does not cause ecotoxic effects in Daphnia similis and Vibrio fischeri. *Journal of Hazardous Materials*, *192*(2), 628–633. https://doi.org/10.1016/j.jhazmat.2011.05.063

Fortunelli, A., Goddard, W. A., Sementa, L., & Barcaro, G. (2015). Optimizing the oxygen evolution reaction for electrochemical water oxidation by tuning solvent properties. *Nanoscale*, *7*(10), 4514–4521. https://doi.org/10.1039/c4nr07277d

Fu, K., Wang, Y., Mao, L., Yang, X., Peng, W., Jin, J., Yang, S., & Li, G. (2019). Rational assembly of hybrid carbon nanotubes grafted on the carbon nanofibers as reliable and robust bifunctional catalyst for rechargeable zinc-air battery. *Journal of Power Sources*, *421*(April 2018), 68–75. https://doi.org/10.1016/j.jpowsour.2019.03.005

Gao, W., Liu, W., Leng, Y., Wang, X., Wang, X., Hu, B., Yu, D., Sang, Y., & Liu, H. (2015). In_2S_3 nanomaterial as a broadband spectrum photocatalyst to display significant activity. *Applied Catalysis B: Environmental*, *176–177*, 83–90. https://doi.org/10.1016/j.apcatb.2015.03.048

Gao, Xiaorui, Liu, X., Zang, W., Dong, H., Pang, Y., Kou, Z., Wang, P., Pan, Z., Wei, S., Mu, S., & Wang, J. (2020). Synergizing in-grown Ni_3N/Ni heterostructured core and ultrathin Ni_3N surface shell enables self-adaptive surface reconfiguration and efficient oxygen evolution reaction. *Nano Energy*, *78*(September), 105355. https://doi.org/10.1016/j.nanoen.2020.105355

Gao, Xu, Wu, H., Li, W., Tian, Y., Zhang, Y., Wu, H., Yang, L., Zou, G., Hou, H., & Ji, X. (2020). H+-Insertion Boosted α-MnO2 for an Aqueous Zn-Ion Battery. *Small*, *16*(5). https://doi.org/10.1002/smll.201905842

Gautam, S., Agrawal, H., Thakur, M., Akbari, A., Sharda, H., Kaur, R., & Amini, M. (2020). Metal oxides and metal organic frameworks for the photocatalytic degradation: A review. *Journal of Environmental Chemical Engineering*, *8*(3), 103726. https://doi.org/10.1016/j.jece.2020.103726

Gharaei, S. K., Abbasnejad, M., & Maezono, R. (2018). Bandgap reduction of photocatalytic TiO_2 nanotube by Cu doping. *Scientific Reports*, *8*(1), 1–10. https://doi.org/10.1038/s41598-018-32130-w

González-Martín, J., Kraakman, N. J. R., Pérez, C., Lebrero, R., & Muñoz, R. (2021). A state–of–the-art review on indoor air pollution and strategies for indoor air pollution control. *Chemosphere*, *262*. https://doi.org/10.1016/j.chemosphere.2020.128376

Gül, Ş., & Özcan-Yildirim, Ö. (2009). Degradation of Reactive Red 194 and Reactive Yellow 145 azo dyes by O_3 and H_2O_2/UV-C processes. *Chemical Engineering Journal*, *155*(3), 684–690. https://doi.org/10.1016/j.cej.2009.08.029

Guo, Y., Zhou, X., Tang, J., Tanaka, S., Kaneti, Y. V., Na, J., Jiang, B., Yamauchi, Y., Bando, Y., & Sugahara, Y. (2020). Multiscale structural optimization: Highly efficient hollow iron-doped metal sulfide heterostructures as bifunctional electrocatalysts for water splitting. *Nano Energy*, *75*(March), 104913. https://doi.org/10.1016/j.nanoen.2020.104913

Gupta, V. K., Pathania, D., Agarwal, S., & Singh, P. (2012). Adsorptional photocatalytic degradation of methylene blue onto pectin-CuS nanocomposite under solar light. *Journal of Hazardous Materials*, *243*, 179–186. https://doi.org/10.1016/j.jhazmat.2012.10.018

Gusain, R., Gupta, K., Joshi, P., & Khatri, O. P. (2019). Adsorptive removal and photocatalytic degradation of organic pollutants using metal oxides and their composites: A comprehensive review. *Advances in Colloid and Interface Science*, *272*, 102009. https://doi.org/10.1016/j.cis.2019.102009

Hao, H., & Lang, X. (2019). Metal Sulfide Photocatalysis: Visible-Light-Induced Organic Transformations. *ChemCatChem*, *11*(5), 1378–1393. https://doi.org/10.1002/cctc.201801773

Haq, I., Raj, A., & Markandeya. (2018). Biodegradation of Azure-B dye by Serratia liquefaciens and its validation by phytotoxicity, genotoxicity and cytotoxicity studies. *Chemosphere*, *196*, 58–68. https://doi.org/10.1016/j.chemosphere.2017.12.153

Hazarika, K. K., Yamada, Y., Matus, E. V., Kerzhentsev, M., & Bharali, P. (2021). Enhancing the electrocatalytic activity via hybridization of Cu(I/II) oxides with Co3O4 towards oxygen electrode reactions. *Journal of Power Sources*, *490*(January), 229511. https://doi.org/10.1016/j.jpowsour.2021.229511

Hofmann, D. M., Fairbrother, D. H., Hamers, R. J., & Murphy, C. J. (2019). Two-Phase Synthesis of Gold-Copper Bimetallic Nanoparticles of Tunable Composition: Toward Optimized Catalytic CO_2 Reduction. *ACS Applied Nano Materials*, *2*(6), 3989–3998. https://doi.org/10.1021/acsanm.9b00904

Hong, D., Zang, W., Guo, X., Fu, Y., He, H., Sun, J., Xing, L., Liu, B., & Xue, X. (2016). High Piezo-photocatalytic Efficiency of CuS/ZnO Nanowires Using Both Solar and Mechanical Energy for Degrading Organic Dye. *ACS Applied Materials and Interfaces*, *8*(33), 21302–21314. https://doi.org/10.1021/acsami.6b05252

Horani, F., & Lifshitz, E. (2019). Unraveling the Growth Mechanism Forming Stable γ-In_2S_3 and β-In_2S_3 Colloidal Nanoplatelets. *Chemistry of Materials*, *31*(5), 1784–1793. https://doi.org/10.1021/acs.chemmater.9b00013

Hoshi, N., Nakamura, M., & Hitotsuyanagi, A. (2013). Active sites for the oxygen reduction reaction on the high index planes of Pt. *Electrochimica Acta*, *112*, 899–904. https://doi.org/10.1016/j.electacta.2013.05.045

Hossain, S., Abdalla, A. M., Suhaili, S. B. H., Kamal, I., Shaikh, S. P. S., Dawood, M. K., & Azad, A. K. (2020). Nanostructured graphene materials utilization in fuel cells and batteries: A review. *Journal of Energy Storage*, *29*(April), 101386. https://doi.org/10.1016/j.est.2020.101386

Hou, Y., Wen, Z., Cui, S., Ci, S., Mao, S., & Chen, J. (2015). An advanced nitrogen-doped graphene/cobalt-embedded porous carbon polyhedron hybrid for efficient catalysis of oxygen reduction and water splitting. *Advanced Functional Materials*, *25*(6), 872–882. https://doi.org/10.1002/adfm.201403657

Hu, F. P., Zhang, X. G., Xiao, F., & Zhang, J. L. (2005). Oxygen reduction on Ag-MnO_2/SWNT and Ag-MnO_2/AB electrodes. *Carbon*, *43*(14), 2931–2936. https://doi.org/10.1016/j.carbon.2005.06.010

Huang, H. B., Wang, Y., Jiao, W. Bin, Cai, F. Y., Shen, M., Zhou, S. G., Cao, H. L., Lü, J., & Cao, R. (2018). Lotus-Leaf-Derived Activated-Carbon-Supported Nano-CdS as Energy-Efficient Photocatalysts under Visible Irradiation. *ACS Sustainable Chemistry and Engineering*, *6*(6), 7871–7879. https://doi.org/10.1021/acssuschemeng.8b01021

Huang, Hengming, Dai, B., Wang, W., Lu, C., Kou, J., Ni, Y., Wang, L., & Xu, Z. (2017). Oriented built-in electric field introduced by surface gradient diffusion doping for enhanced photocatalytic H_2 evolution in CdS nanorods. *Nano Letters*, *17*(6), 3803–3808. https://doi.org/10.1021/acs.nanolett.7b01147

Huang, Huoshuai, Jiang, X., Li, N., Chen, D., Xu, Q., Li, H., He, J., & Lu, J. (2021). Noble-metal-free ultrathin MXene coupled with In_2S_3 nanoflakes for ultrafast photocatalytic reduction of hexavalent chromium. *Applied Catalysis B: Environmental*, *284*(July 2020), 119754. https://doi.org/10.1016/j.apcatb.2020.119754

Huang, Y., Nengzi, L. chao, Zhang, X., Gou, J., Gao, Y., Zhu, G., Cheng, Q., & Cheng, X. (2020). Catalytic degradation of ciprofloxacin by magnetic $CuS/Fe_2O_3/Mn_2O_3$ nanocomposite activated peroxymonosulfate: Influence factors, degradation pathways and reaction mechanism. *Chemical Engineering Journal*, *388*(November 2019). https://doi.org/10.1016/j.cej.2020.124274

Huang, Z. F., Wang, J., Peng, Y., Jung, C. Y., Fisher, A., & Wang, X. (2017). Design of efficient bifunctional oxygen reduction/evolution electrocatalyst: Recent advances and perspectives. *Advanced Energy Materials*, *7*(23), 1–21. https://doi.org/10.1002/aenm.201700544

Hulicova-Jurcakova, D., Seredych, M., Lu, G. Q., & Bandosz, T. J. (2009). Combined effect of nitrogen- and oxygen-containing functional groups of microporous activated carbon on its electrochemical performance in supercapacitors. *Advanced Functional Materials*, *19*(3), 438–447. https://doi.org/10.1002/adfm.200801236

Ibrahim, M., Labaki, M., Giraudon, J. M., & Lamonier, J. F. (2020). Hydroxyapatite, a multifunctional material for air, water and soil pollution control: A review. *Journal of Hazardous Materials*, *383*(September 2019), 121139. https://doi.org/10.1016/j.jhazmat.2019.121139

Iqbal, S., Bahadur, A., Anwer, S., Ali, S., Saeed, A., Muhammad Irfan, R., Li, H., Javed, M., Raheel, M., & Shoaib, M. (2020). Shape and phase-controlled synthesis of specially designed 2D morphologies of L-cysteine surface capped covellite (CuS) and chalcocite (Cu2S) with excellent photocatalytic properties in the visible spectrum. *Applied Surface Science*, *526*(March), 146691. https://doi.org/10.1016/j.apsusc.2020.146691

Iqbal, S., Bahadur, A., Anwer, S., Shoaib, M., Liu, G., Li, H., Raheel, M., Javed, M., & Khalid, B. (2020). Designing novel morphologies of l-cysteine surface capped 2D covellite (CuS) nanoplates to study the effect of CuS morphologies on dye degradation rate under visible light. *CrystEngComm*, *22*(24), 4162–4173. https://doi.org/10.1039/d0ce00421a

Iqbal, S., Xu, J., Allen, S. D., Khan, S., Nadir, S., Arif, M. S., & Yasmeen, T. (2020). Unraveling consequences of soil micro- and nano-plastic pollution on soil-plant system: Implications for nitrogen (N) cycling and soil microbial activity. *Chemosphere*, *260*, 127578. https://doi.org/10.1016/j.chemosphere.2020.127578

Isac, L., Andronic, L., Visa, M., & Enesca, A. (2020). Selective photocatalytic degradation of organic pollutants by $Cu_xS/ZnO/TiO_2$ heterostructures. *Ceramics International*, *46*(4), 4265–4273. https://doi.org/10.1016/j.ceramint.2019.10.147

Isac, L., Cazan, C., Enesca, A., & Andronic, L. (2019). Copper Sulfide Based Heterojunctions as Photocatalysts for Dyes Photodegradation. *Frontiers in Chemistry*, *7*(October), 1–9. https://doi.org/10.3389/fchem.2019.00694

Ito, T., Adachi, Y., Yamanashi, Y., & Shimada, Y. (2016). Long–term natural remediation process in textile dye–polluted river sediment driven by bacterial community changes. *Water Research*, *100*, 458–465. https://doi.org/10.1016/j.watres.2016.05.050

Iwase, A., Yoshino, S., Takayama, T., Ng, Y. H., Amal, R., & Kudo, A. (2016). Water Splitting and CO_2 Reduction under Visible Light Irradiation Using Z-Scheme Systems Consisting of Metal Sulfides, CoO_x-Loaded $BiVO_4$, and a Reduced Graphene Oxide Electron Mediator. *Journal of the American Chemical Society*, *138*(32), 10260–10264. https://doi.org/10.1021/jacs.6b05304

Ji, J., Yao, J., Xu, Y., Wan, H., Zhang, B., Lv, L., Li, J., Wang, N., Zheng, Z., Zhang, J., Ma, G., Tao, L., Wang, H., Wang, Y., & Wang, H. (2022). Promoting Proton Migration Kinetics by Ni^{2+} Regulating Enables Improved Aqueous Zn-MnO_2 Batteries. *Energy and Environmental Materials*, 1–10. https://doi.org/10.1002/eem2.12340

Jiang, S., Tian, K., Li, X., Duan, C. Q., Wang, D., Wang, Z., Sun, H., Zheng, R., & Liu, Y. (2022). Amorphous High-entropy Non-precious metal oxides with surface reconstruction toward highly efficient and durable catalyst for oxygen evolution reaction. *Journal of Colloid and Interface Science*, *606*, 635–644. https://doi.org/10.1016/j.jcis.2021.08.060

Kang, Y. H., Chen, T., Gao, J., Li, F., Hu, L., Liu, G. H., Lu, C. Y., Li, Y. J., Wei, X. Y., Ma, Y. J., Zong, Z. M., & Bai, H. C. (2022). Comprehensive investigation of the mechanisms for pyrolyzing macromolecular networks in Hecaogou subbituminous coal by comparing the ethanolysis and flash pyrolysis. *Fuel*, *324*(PB), 124619. https://doi.org/10.1016/j.fuel.2022.124619

Kao, Y. T., Yang, S. M., & Lu, K. C. (2019). Synthesis and photocatalytic properties of CuO-CuS core-shell nanowires. *Materials*, *12*(7). https://doi.org/10.3390/ma12071106

Khan, I., Saeed, K., Zekker, I., Zhang, B., Hendi, A. H., Ahmad, A., Ahmad, S., Zada, N., Ahmad, H., Shah, L. A., Shah, T., & Khan, I. (2022). *and Photodegradation*.

Khan, M. A., Sen, U. R., Khan, S., Sengupta, S., Shruti, S., & Naskar, S. (2022). Manganese based Molecular Water Oxidation Catalyst: From Natural to Artificial Photosynthesis. *Comments on Inorganic Chemistry*, *00*(00), 1–34. https://doi.org/10.1080/02603594.2022.2130273

Khan, S., Naushad, M., Lima, E. C., Zhang, S., Shaheen, S. M., & Rinklebe, J. (2021). Global soil pollution by toxic elements: Current status and future perspectives on the risk assessment and remediation strategies – A review. *Journal of Hazardous Materials*, *417*(May), 0–2. https://doi.org/10.1016/j.jhazmat.2021.126039

Khanchandani, S., Kundu, S., Patra, A., & Ganguli, A. K. (2013). Band gap tuning of ZnO/In_2S_3 core/shell nanorod arrays for enhanced visible-light-driven photocatalysis. *Journal of Physical Chemistry C*, *117*(11), 5558–5567. https://doi.org/10.1021/jp310495j

Khatri, A., Peerzada, M. H., Mohsin, M., & White, M. (2015). A review on developments in dyeing cotton fabrics with reactive dyes for reducing effluent pollution. *Journal of Cleaner Production*, *87*(1), 50–57. https://doi.org/10.1016/j.jclepro.2014.09.017

Kheirandish, A., Kazemi, M. S., & Dahari, M. (2014). Dynamic performance assessment of the efficiency of fuel cell-powered bicycle: An experimental approach. *International Journal of Hydrogen Energy*, *39*(25), 13276–13284. https://doi.org/10.1016/j.ijhydene.2014.06.138

Khlyustova, A., Sirotkin, N., Kusova, T., Kraev, A., Titov, V., & Agafonov, A. (2020). Doped TiO_2 : the effect of doping elements on photocatalytic activity . *Materials Advances*, *1*(5), 1193–1201. https://doi.org/10.1039/d0ma00171f

Kirubakaran, A., Jain, S., & Nema, R. K. (2009). A review on fuel cell technologies and power electronic interface. *Renewable and Sustainable Energy Reviews*, *13*(9), 2430–2440. https://doi.org/10.1016/j.rser.2009.04.004

Köhler, J., & Chang, J. H. (2000). [PtIn6]10+ octahedra in $PtIn_7F_{13}$: The first compound of a new class of metal-cluster fluorides. *Angewandte Chemie - International Edition*, *39*(11), 1998–2000. https://doi.org/10.1002/1521-3773(20000602)39:11<1998::AID-ANIE1998>3.0.CO;2-X

Kong, L., Guo, J., Makepeace, J. W., Xiao, T., Greer, H. F., Zhou, W., Jiang, Z., & Edwards, P. P. (2019). Rapid synthesis of $BiOBr_xI_{1-x}$ photocatalysts: Insights to the visible-light photocatalytic activity and strong deviation from Vegard's law. *Catalysis Today*, *335*(February), 477–484. https://doi.org/10.1016/j.cattod.2019.02.013

Korberg, A. D., Brynolf, S., Grahn, M., & Skov, I. R. (2021). Techno-economic assessment of advanced fuels and propulsion systems in future fossil-free ships. *Renewable and Sustainable Energy Reviews*, *142*(July 2020). https://doi.org/10.1016/j.rser.2021.110861

Kumar, A., Khan, M., Zeng, X., & Lo, I. M. C. (2018). Development of g-C_3N_4/TiO_2/Fe_3O_4@SiO_2 heterojunction via sol-gel route: A magnetically recyclable direct contact Z-scheme nanophotocatalyst for enhanced photocatalytic removal of ibuprofen from real sewage effluent under visible light. *Chemical Engineering Journal*, *353*(July), 645–656. https://doi.org/10.1016/j.cej.2018.07.153

Kumar, K. V., Porkodi, K., & Rocha, F. (2008). Langmuir-Hinshelwood kinetics - A theoretical study. *Catalysis Communications*, *9*(1), 82–84. https://doi.org/10.1016/j.catcom.2007.05.019

Kwan, T. H., Shen, Y., & Pei, G. (2021). Recycling fuel cell waste heat to the thermoelectric cooler for enhanced combined heat, power and water production. *Energy*, *223*, 119922. https://doi.org/10.1016/j.energy.2021.119922

Lachheb, H., Puzenat, E., Houas, A., Ksibi, M., Elaloui, E., Guillard, C., & Herrmann, J. M. (2002). Photocatalytic degradation of various types of dyes (Alizarin S, Crocein Orange G, Methyl Red, Congo Red, Methylene Blue) in water by UV-irradiated titania. *Applied Catalysis B: Environmental*, *39*(1), 75–90. https://doi.org/10.1016/S0926-3373(02)00078-4

Laming, J. M. (2009). Non-wkb models of the first ionization potential effect: Implications for solar coronal heating and the coronal helium and neon abundances. *Astrophysical Journal*, *695*(2), 954–969. https://doi.org/10.1088/0004-637X/695/2/954

Lee, H. J., Noor, N., Gumeci, C., Dale, N., Parrondo, J., & Higgins, D. C. (2022). Understanding the Impact of the Morphology, Phase Structure, and Mass Fraction of MnO_2within MnO_2/Reduced Graphene Oxide Composites for Supercapacitor Applications. *Journal of Physical Chemistry C*, *126*(31), 13004–13014. https://doi.org/10.1021/acs.jpcc.2c02731

Lee, K. M., Lai, C. W., Ngai, K. S., & Juan, J. C. (2016). Recent developments of zinc oxide based photocatalyst in water treatment technology: A review. *Water Research*, *88*, 428–448. https://doi.org/10.1016/j.watres.2015.09.045

Lee, S. Y., & Mahajan, R. L. (2021). A facile method for coal to graphene oxide and its application to a biosensor. *Carbon*, *181*, 408–420. https://doi.org/10.1016/j.carbon.2021.05.007

Lee, W. H., Ko, Y. J., Kim, J. H., Choi, C. H., Chae, K. H., Kim, H., Hwang, Y. J., Min, B. K., Strasser, P., & Oh, H. S. (2021). High crystallinity design of Ir-based catalysts drives catalytic reversibility for water electrolysis and fuel cells. *Nature Communications*, *12*(1), 1–10. https://doi.org/10.1038/s41467-021-24578-8

Li, F., Kong, T., Bi, W., Li, D., Li, Z., & Huang, X. (2009). Synthesis and optical properties of CuS nanoplate-based architectures by a solvothermal method. *Applied Surface Science*, *255*(12), 6285–6289. https://doi.org/10.1016/j.apsusc.2009.02.001

Li, J., Ma, Y., Ye, Z., Zhou, M., Wang, H., Ma, C., Wang, D., Huo, P., & Yan, Y. (2017). Fast electron transfer and enhanced visible light photocatalytic activity using multi-dimensional components of carbon quantum dots@3D daisy-like In_2S_3/single-wall carbon nanotubes. *Applied Catalysis B: Environmental*, *204*, 224–238. https://doi.org/10.1016/j.apcatb.2016.11.021

Li, N., Fu, W., Chen, C., Liu, M., Xue, F., Shen, Q., & Zhou, J. (2018). Controlling the Core-Shell Structure of CuS@CdS Heterojunction via Seeded Growth with Tunable Photocatalytic Activity. *ACS Sustainable Chemistry and Engineering*, *6*(11), 15867–15875. https://doi.org/10.1021/acssuschemeng.8b04606

Li, W., Wang, G., Feng, Y., & Li, Z. (2018). Efficient photocatalytic performance enhancement in Co-doped ZnO nanowires coupled with CuS nanoparticles. *Applied Surface Science*, *428*, 154–164. https://doi.org/10.1016/j.apsusc.2017.09.049

Li, X., Wei, Y., Ma, C., Jiang, H., Gao, M., Zhang, S., Liu, W., Huo, P., Wang, H., & Wang, L. (2021). Multichannel Electron Transmission and Fluorescence Resonance Energy Transfer in In_2S_3/Au/rGO Composite for CO_2 Photoreduction. *ACS Applied Materials and Interfaces*, *13*(10), 11755–11764. https://doi.org/10.1021/acsami.0c18809

Li, Yanguang, & Lu, J. (2017). Metal-Air Batteries: Will They Be the Future Electrochemical Energy Storage Device of Choice? *ACS Energy Letters*, *2*(6), 1370–1377. https://doi.org/10.1021/acsenergylett.7b00119

Li, Yujie, Li, T., Tian, J., Wang, X., & Cui, H. (2017). TiO_2 Nanobelts Decorated with In_2S_3 Nanoparticles as Photocatalysts with Enhanced Full-Solar-Spectrum (UV–vis–NIR) Photocatalytic Activity toward the Degradation of Tetracycline. *Particle and Particle Systems Characterization*, *34*(7), 1–12. https://doi.org/10.1002/ppsc.201700127

Ling, W., Wang, H., Chen, Z., Ji, Z., Wang, J., Wei, J., & Huang, Y. (2021). Intrinsic Structure Modification of Electrode Materials for Aqueous Metal-Ion and Metal-Air Batteries. *Advanced Functional Materials*, *31*(5). https://doi.org/10.1002/adfm.202006855

Liu, M., Li, P., Wang, S., Liu, Y., Zhang, J., Chen, L., Wang, J., Liu, Y., Shen, Q., Qu, P., & Sun, H. (2021). Hierarchically porous hydrangea-like In_2S_3/In_2O_3 heterostructures for enhanced photocatalytic hydrogen evolution. *Journal of Colloid and Interface Science*, *587*, 876–882. https://doi.org/10.1016/j.jcis.2020.11.048

Liu, T., Zhang, L., & Tian, Y. (2018). Earthworm-like N, S-Doped carbon tube-encapsulated Co_9S_8 nanocomposites derived from nanoscaled metal-organic frameworks for highly efficient bifunctional oxygen catalysis. *Journal of Materials Chemistry A*, *6*(14), 5935–5943. https://doi.org/10.1039/c7ta11122c

Liu, X., Zhang, T., Li, Y., Zhang, J., Du, Y., Yang, Y., Jiang, Y., & Lin, K. (2021). Construction of core-shell $ZnS@In_2S_3$ rhombic dodecahedron Z-scheme heterojunction structure: Enhanced photocatalytic activity and mechanism insight. *Chemical Engineering Journal*, *423*(April), 130138. https://doi.org/10.1016/j.cej.2021.130138

Liu, Y., Zeng, Z., Bloom, B., Waldeck, D. H., & Wei, J. (2018). Stable Low-Current Electrodeposition of α-MnO_2 on Superaligned Electrospun Carbon Nanofibers for High-Performance Energy Storage. *Small*, *14*(3), 1–7. https://doi.org/10.1002/smll.201703237

Lu, X. F., Xia, B. Y., Zang, S., & Lou, X. W. (David). (2020). Metal–Organic Frameworks Based Electrocatalysts for the Oxygen Reduction Reaction. *Angewandte Chemie*, *132*(12), 4662–4678. https://doi.org/10.1002/ange.201910309

Lv, S. W., Cong, Y., Chen, X., Wang, W., & Che, L. (2022). Developing fine-tuned metal–organic frameworks for photocatalytic treatment of wastewater: A review. *Chemical Engineering Journal*, *433*(P2), 133605. https://doi.org/10.1016/j.cej.2021.133605

Ma, D., Wang, Z., Shi, J. W., Zhu, M., Yu, H., Zou, Y., Lv, Y., Sun, G., Mao, S., & Cheng, Y. (2020). Cu-In_2S_3 nanorod induced the growth of Cu&In co-doped multi-arm CdS hetero-phase junction to promote photocatalytic H2 evolution. *Chemical Engineering Journal*, *399*(June), 125785. https://doi.org/10.1016/j.cej.2020.125785

Ma, J., Yu, F., Zhou, L., Jin, L., Yang, M., Luan, J., Tang, Y., Fan, H., Yuan, Z., & Chen, J. (2012). Enhanced adsorptive removal of methyl orange and methylene blue from aqueous solution by alkali-activated multiwalled carbon nanotubes. *ACS Applied Materials and Interfaces*, *4*(11), 5749–5760. https://doi.org/10.1021/am301053m

Ma, L., Liang, S., Liu, X. L., Yang, D. J., Zhou, L., & Wang, Q. Q. (2015). Synthesis of dumbbell-like gold-metal sulfide core-shell nanorods with largely enhanced transverse plasmon resonance in visible region and efficiently improved photocatalytic activity. *Advanced Functional Materials*, *25*(6), 898–904. https://doi.org/10.1002/adfm.201403398

Ma, R., Lin, G., Zhou, Y., Liu, Q., Zhang, T., Shan, G., Yang, M., & Wang, J. (2019). A review of oxygen reduction mechanisms for metal-free carbon-based electrocatalysts. *Npj Computational Materials*, *5*(1). https://doi.org/10.1038/s41524-019-0210-3

Makuła, P., Pacia, M., & Macyk, W. (2018). How To Correctly Determine the Band Gap Energy of Modified Semiconductor Photocatalysts Based on UV-Vis Spectra. *Journal of Physical Chemistry Letters*, *9*(23), 6814–6817. https://doi.org/10.1021/acs.jpclett.8b02892

Mardini, N., & Bicer, Y. (2021). Direct synthesis of formic acid as hydrogen carrier from CO_2 for cleaner power generation through direct formic acid fuel cell. *International Journal of Hydrogen Energy*, *46*(24), 13050–13060. https://doi.org/10.1016/j.ijhydene.2021.01.124

Marshall, A. T., & Vaisson-Béthune, L. (2015). Avoid the quasi-equilibrium assumption when evaluating the electrocatalytic oxygen evolution reaction mechanism by Tafel slope analysis. *Electrochemistry Communications*, *61*, 23–26. https://doi.org/10.1016/j.elecom.2015.09.019

Masa, J., Schilling, T., Bron, M., & Schuhmann, W. (2012). Electrochemical synthesis of metal-polypyrrole composites and their activation for electrocatalytic reduction of oxygen by thermal treatment. *Electrochimica Acta*, *60*, 410–418. https://doi.org/10.1016/j.electacta.2011.11.076

Mayonado, G., Mian, S. M., Robbiano, V., & Cacialli, F. (2015). *Investigation Of The Bragg-Snell Law In Photonic Crystals*. 60–63. https://doi.org/10.1119/bfy.2015.pr.015

McDuffie, E. E., Martin, R. V., Spadaro, J. V., Burnett, R., Smith, S. J., O'Rourke, P., Hammer, M. S., van Donkelaar, A., Bindle, L., Shah, V., Jaeglé, L., Luo, G., Yu, F., Adeniran, J. A., Lin, J., & Brauer, M. (2021). Source sector and fuel contributions to ambient PM2.5 and attributable mortality across multiple spatial scales. *Nature Communications*, *12*(1), 1–12. https://doi.org/10.1038/s41467-021-23853-y

Messerer, A., Niessner, R., & Pöschl, U. (2006). Comprehensive kinetic characterization of the oxidation and gasification of model and real diesel soot by nitrogen oxides and oxygen under engine exhaust conditions: Measurement, Langmuir-Hinshelwood, and Arrhenius parameters. *Carbon*, *44*(2), 307–324. https://doi.org/10.1016/j.carbon.2005.07.017

Meyer, E., Mbese, J., & Agoro, M. (2019). *Exciting New Infrared Material*. 1–19.

Mondal, R., Ratnawat, H., Mukherjee, S., Gupta, A., & Singh, P. (2022). Investigation of the Role of Sr and Development of Superior Sr-Doped Hexagonal $BaCoO_3$-δ Perovskite Bifunctional OER/ORR Catalysts in Alkaline Media. *Energy and Fuels*, *36*(6), 3219–3228. https://doi.org/10.1021/acs.energyfuels.2c00357

Morales-García, A., Soares, A. L., Dos Santos, E. C., De Abreu, H. A., & Duarte, H. A. (2014). First-principles calculations and electron density topological analysis of covellite (CuS). *Journal of Physical Chemistry A*, *118*(31), 5823–5831. https://doi.org/10.1021/jp4114706

Naqash, N., Prakash, S., Kapoor, D., & Singh, R. (2020). Interaction of freshwater microplastics with biota and heavy metals: a review. *Environmental Chemistry Letters*, *18*(6), 1813–1824. https://doi.org/10.1007/s10311-020-01044-3

Ndlwana, L., Raleie, N., Dimpe, K. M., Ogutu, H. F., Oseghe, E. O., Motsa, M. M., Msagati, T. A. M., & Mamba, B. B. (2021). Sustainable hydrothermal and solvothermal synthesis of advanced carbon materials in multidimensional applications: A review. *Materials*, *14*(17). https://doi.org/10.3390/ma14175094

Nguyen, C. H., Fu, C. C., & Juang, R. S. (2018). Degradation of methylene blue and methyl orange by palladium-doped TiO2 photocatalysis for water reuse: Efficiency and degradation pathways. *Journal of Cleaner Production*, *202*, 413–427. https://doi.org/10.1016/j.jclepro.2018.08.110

Nwaji, N., & Akinoglu, E. M. (2021). Synthesis of ZnS-CuS-Bi nanonail heterostructures and funnel mechanism of their photocatalytic activity. *Journal of Environmental Chemical Engineering*, *9*(5), 106066. https://doi.org/10.1016/j.jece.2021.106066

Oh, N. K., Seo, J., Lee, S., Kim, H. J., Kim, U., Lee, J., Han, Y. K., & Park, H. (2021). Highly efficient and robust noble-metal free bifunctional water electrolysis catalyst achieved via complementary charge transfer. *Nature Communications*, *12*(1), 1–12. https://doi.org/10.1038/s41467-021-24829-8

Oros-Ruiz, S., Zanella, R., & Prado, B. (2013). Photocatalytic degradation of trimethoprim by metallic nanoparticles supported on TiO_2-P25. *Journal of Hazardous Materials*, *263*, 28–35. https://doi.org/10.1016/j.jhazmat.2013.04.010

Peng, X., Zhang, L., Chen, Z., Zhong, L., Zhao, D., Chi, X., Zhao, X., Li, L., Lu, X., Leng, K., Liu, C., Liu, W., Tang, W., & Loh, K. P. (2019). Hierarchically Porous Carbon Plates Derived from Wood as Bifunctional ORR/OER Electrodes. *Advanced Materials*, *31*(16). https://doi.org/10.1002/adma.201900341

Peng, Y., Lai, C., Zhang, M., Liu, X., Yin, Y., Li, Y., & Wu, Z. (2022). Zn–Sn alloy anode with repressible dendrite grown and meliorative corrosion resistance for Zn-air battery. *Journal of Power Sources*, *526*(February), 231173. https://doi.org/10.1016/j.jpowsour.2022.231173

Perera, S. D., Zhang, H., Ding, X., Nelson, A., & Robinson, R. D. (2015). Nanocluster seed-mediated synthesis of $CuInS_2$ quantum dots, nanodisks, nanorods, and doped Zn-$CuInGaS_2$ quantum dots. *Journal of Materials Chemistry C*, *3*(5), 1044–1055. https://doi.org/10.1039/c4tc01887g

Pierini, A., Brutti, S., & Bodo, E. (2021). Reactive pathways toward parasitic release of singlet oxygen in metal-air batteries. *Npj Computational Materials*, *7*(1), 1–8. https://doi.org/10.1038/s41524-021-00597-3

Pinjari, S., Bera, T., Kapur, G. S., & Kjeang, E. (2022). The mechanism and sorption kinetic analysis of hydrogen storage at room temperature using acid functionalized carbon nanotubes. *International Journal of Hydrogen Energy*, *xxxx*. https://doi.org/10.1016/j.ijhydene.2022.10.080

Pirhashemi, M., Habibi-Yangjeh, A., & Rahim Pouran, S. (2018). Review on the criteria anticipated for the fabrication of highly efficient ZnO-based visible-light-driven photocatalysts. *Journal of Industrial and Engineering Chemistry*, *62*, 1–25. https://doi.org/10.1016/j.jiec.2018.01.012

Pistor, P., Álvarez, J. M. M., León, M., Di Michiel, M., Schorr, S., Klenk, R., & Lehmann, S. (2016). Structure reinvestigation of α-, β- and γ-In_2S_3. *Acta Crystallographica Section B: Structural Science, Crystal Engineering and Materials*, *72*(3), 410–415. https://doi.org/10.1107/S2052520616007058

Prabhu, Y. T., Rao, K. V., Kumar, V. S. S., Kumari, B. S., & Scardi, P. (2014). X-Ray Analysis by Williamson-Hall and Size-Strain Plot Methods of ZnO Nanoparticles with Fuel Variation. *World Journal of Nano Science and Engineering*, *20*(01), 6903–6916. https://doi.org/10.1021/acs.cgd.0c00956

Pradhan, A. C., & Uyar, T. (2017). Morphological Control of Mesoporosity and Nanoparticles within Co_3O_4-CuO Electrospun Nanofibers: Quantum Confinement and Visible Light Photocatalysis Performance. *ACS Applied Materials and Interfaces*, *9*(41), 35757–35774. https://doi.org/10.1021/acsami.7b09026

Prado, A. G. S., Bolzon, L. B., Pedroso, C. P., Moura, A. O., & Costa, L. L. (2008). Nb_2O_5 as efficient and recyclable photocatalyst for indigo carmine degradation. *Applied Catalysis B: Environmental*, *82*(3–4), 219–224. https://doi.org/10.1016/j.apcatb.2008.01.024

Premathilake, D., Outlaw, R. A., Parler, S. G., Butler, S. M., & Miller, J. R. (2017). Electric double layer capacitors for ac filtering made from vertically oriented graphene nanosheets on aluminum. *Carbon*, *111*, 231–237. https://doi.org/10.1016/j.carbon.2016.09.080

Qian, J., Wang, K., Guan, Q., Li, H., Xu, H., Liu, Q., Liu, W., & Qiu, B. (2014). Enhanced wet hydrogen peroxide catalytic oxidation performances based on CuS nanocrystals/reduced graphene oxide composites. *Applied Surface Science*, *288*, 633–640. https://doi.org/10.1016/j.apsusc.2013.10.086

Quevedo, M. C., Galicia, G., Mayen-Mondragon, R., & Llongueras, J. G. (2018). Role of turbulent flow seawater in the corrosion enhancement of an Al-Zn-Mg alloy: An electrochemical impedance spectroscopy (EIS) analysis of oxygen reduction reaction (ORR). *Journal of Materials Research and Technology*, *7*(2), 149–157. https://doi.org/10.1016/j.jmrt.2017.06.004

Rais, B., Ostrowski, E. T., Canton, A., Skinner, C. H., Barison, S., Fiameni, S., & Koel, B. E. (2021). SIMS and HR-XPS characterization of lithiated graphite from the magnetic fusion device RFX-mod. *Applied Surface Science*, *567*(August), 150830. https://doi.org/10.1016/j.apsusc.2021.150830

Raizada, P., Sudhaik, A., Patial, S., Hasija, V., Parwaz Khan, A. A., Singh, P., Gautam, S., Kaur, M., & Nguyen, V. H. (2020). Engineering nanostructures of CuO-based photocatalysts for water treatment: Current progress and future challenges. In *Arabian Journal of Chemistry* (Vol. 13, Issue 11). The Author(s). https://doi.org/10.1016/j.arabjc.2020.06.031

Rauf, M. A., & Salman Ashraf, S. (2012). Survey of recent trends in biochemically assisted degradation of dyes. *Chemical Engineering Journal*, *209*, 520–530. https://doi.org/10.1016/j.cej.2012.08.015

Reier, T., Oezaslan, M., & Strasser, P. (2012). Electrocatalytic oxygen evolution reaction (OER) on Ru, Ir, and pt catalysts: A comparative study of nanoparticles and bulk materials. *ACS Catalysis*, *2*(8), 1765–1772. https://doi.org/10.1021/cs3003098

Ren, J. T., Wang, Y. S., Chen, L., Gao, L. J., Tian, W. W., & Yuan, Z. Y. (2020). Binary FeNi phosphides dispersed on N,P-doped carbon nanosheets for highly efficient overall water splitting and rechargeable Zn-air batteries. *Chemical Engineering Journal*, *389*(February), 124408. https://doi.org/10.1016/j.cej.2020.124408

Rienstra-Kiracofe, J. C., Tschumper, G. S., Schaefer, H. F., Nandi, S., & Ellison, G. B. (2002). Atomic and molecular electron affinities: Photoelectron experiments and theoretical computations. *Chemical Reviews*, *102*(1), 231–282. https://doi.org/10.1021/cr990044u

Saqib, N. us, Adnan, R., & Shah, I. (2016). A mini-review on rare earth metal-doped TiO_2 for photocatalytic remediation of wastewater. *Environmental Science and Pollution Research*, *23*(16), 15941–15951. https://doi.org/10.1007/s11356-016-6984-7

Scardi, P. (2020). Diffraction Line Profiles in the Rietveld Method. *Crystal Growth and Design*, *20*(10), 6903–6916. https://doi.org/10.1021/acs.cgd.0c00956

Shamraiz, U., Hussain, R. A., & Badshah, A. (2016). Fabrication and applications of copper sulfide (CuS) nanostructures. *Journal of Solid State Chemistry*, *238*, 25–40. https://doi.org/10.1016/j.jssc.2016.02.046

Shao, W., Xiao, M., Yang, C., Cheng, M., Cao, S., He, C., Zhou, M., Ma, T., Cheng, C., & Li, S. (2022). Assembling and Regulating of Transition Metal-Based Heterophase Vanadates as Efficient Oxygen Evolution Catalysts. *Small*, *18*(7), 1–10. https://doi.org/10.1002/smll.202105763

Sheardy, A. T., Arvapalli, D. M., & Wei, J. (2020a). Novel microwave synthesis of near-metallic copper sulfide nanodiscs with size control: experimental and DFT studies of charge carrier density. *Nanoscale Advances*, *2*(3), 1054–1058. https://doi.org/10.1039/d0na00069h

Sheardy, A. T., Arvapalli, D. M., & Wei, J. (2020b). Novel microwave synthesis of near-metallic copper sulfide nanodiscs with size control: experimental and DFT studies of charge carrier density. *Nanoscale Advances*, *2*(3), 1054–1058. https://doi.org/10.1039/d0na00069h

Shen, N., Liao, H., Deng, R., & Wang, Q. (2019). Different types of environmental regulations and the heterogeneous influence on the environmental total factor productivity: Empirical analysis of China's industry. *Journal of Cleaner Production*, *211*, 171–184. https://doi.org/10.1016/j.jclepro.2018.11.170

Shen, T., Jiang, C., Wang, C., Sun, J., Wang, X., & Li, X. (2015). A TiO_2 modified abiotic–biotic process for the degradation of the azo dye methyl orange . *RSC Advances*, *5*(72), 58704–58712. https://doi.org/10.1039/c5ra06686g

Sheng, K., Yi, Q., Chen, A. L., Wang, Y., Yan, Y., Nie, H., & Zhou, X. (2021). CoNi Nanoparticles Supported on N-Doped Bifunctional Hollow Carbon Composites as High-Performance ORR/OER Catalysts for Rechargeable Zn-Air Batteries. *ACS Applied Materials and Interfaces*, *13*(38), 45394–45405. https://doi.org/10.1021/acsami.1c10671

Sheng, W., Song, Y., Dou, M., Ji, J., & Wang, F. (2018). Constructing 1D hierarchical heterostructures of MoS_2 /In_2S_3 nanosheets on CdS nanorod arrays for enhanced photoelectrocatalytic H2 evolution. *Applied Surface Science*, *436*, 613–623. https://doi.org/10.1016/j.apsusc.2017.11.281

Shinagawa, T., Garcia-Esparza, A. T., & Takanabe, K. (2015). Insight on Tafel slopes from a microkinetic analysis of aqueous electrocatalysis for energy conversion. *Scientific Reports*, *5*(August), 1–21. https://doi.org/10.1038/srep13801

Singh, H., Marley-Hines, M., Chakravarty, S., & Nath, M. (2022). Multi-walled carbon nanotube supported manganese selenide as a highly active bifunctional OER and ORR electrocatalyst. *Journal of Materials Chemistry A*, *10*(12), 6772–6784. https://doi.org/10.1039/d1ta09864k

Singh, J., & Soni, R. K. (2021). Fabrication of nanostructured In_2S_3 thin film with broad optical absorption for improved sunlight mediated photocatalysis application. *Optical Materials*, *122*(PA), 111748. https://doi.org/10.1016/j.optmat.2021.111748

Singh, M., Zappa, D., & Comini, E. (2021). Solid oxide fuel cell: Decade of progress, future perspectives and challenges. *International Journal of Hydrogen Energy*, *46*(54), 27643–27674. https://doi.org/10.1016/j.ijhydene.2021.06.020

Singh, P., Shandilya, P., Raizada, P., Sudhaik, A., Rahmani-Sani, A., & Hosseini-Bandegharaei, A. (2020). Review on various strategies for enhancing photocatalytic activity of graphene based nanocomposites for water purification. *Arabian Journal of Chemistry*, *13*(1), 3498–3520. https://doi.org/10.1016/j.arabjc.2018.12.001

Song, C., Wang, X., Zhang, J., Chen, X., & Li, C. (2017). Enhanced performance of direct Z-scheme CuS-WO_3 system towards photocatalytic decomposition of organic pollutants under visible light. *Applied Surface Science*, *425*, 788–795. https://doi.org/10.1016/j.apsusc.2017.07.082

Song, Y., Zhao, X., & Liu, Z. H. (2021). Surface selenium doped hollow heterostructure/defects Co-Fe sulfide nanoboxes for enhancing oxygen evolution reaction and supercapacitors. *Electrochimica Acta*, *374*, 137962. https://doi.org/10.1016/j.electacta.2021.137962

Stacy, J., Regmi, Y. N., Leonard, B., & Fan, M. (2017). The recent progress and future of oxygen reduction reaction catalysis: A review. *Renewable and Sustainable Energy Reviews*, *69*(July 2016), 401–414. https://doi.org/10.1016/j.rser.2016.09.135

Su, C., Yang, T., Zhou, W., Wang, W., Xu, X., & Shao, Z. (2016). Pt/C-$LiCoO_2$ composites with ultralow Pt loadings as synergistic bifunctional electrocatalysts for oxygen reduction and evolution reactions. *Journal of Materials Chemistry A*, *4*(12), 4516–4524. https://doi.org/10.1039/c5ta10492k

Suen, N. T., Hung, S. F., Quan, Q., Zhang, N., Xu, Y. J., & Chen, H. M. (2017). Electrocatalysis for the oxygen evolution reaction: Recent development and future perspectives. *Chemical Society Reviews*, *46*(2), 337–365. https://doi.org/10.1039/c6cs00328a

Sun, H., Xu, X., Song, Y., Zhou, W., & Shao, Z. (2021). Designing High-Valence Metal Sites for Electrochemical Water Splitting. *Advanced Functional Materials*, *31*(16). https://doi.org/10.1002/adfm.202009779

Swinehart, D. F. (1962). The Beer-Lambert law. *Journal of Chemical Education*, *39*(7), 333–335. https://doi.org/10.1021/ed039p333

Tahir, M., Pan, L., Idrees, F., Zhang, X., Wang, L., Zou, J. J., & Wang, Z. L. (2017). Electrocatalytic oxygen evolution reaction for energy conversion and storage: A comprehensive review. *Nano Energy*, *37*(February), 136–157. https://doi.org/10.1016/j.nanoen.2017.05.022

Tainio, M., Jovanovic Andersen, Z., Nieuwenhuijsen, M. J., Hu, L., de Nazelle, A., An, R., Garcia, L. M. T., Goenka, S., Zapata-Diomedi, B., Bull, F., & Sá, T. H. de. (2021). Air pollution, physical activity and health: A mapping review of the evidence. *Environment International*, *147*(June 2020), 105954. https://doi.org/10.1016/j.envint.2020.105954

Tajdid Khajeh, R., Aber, S., & Zarei, M. (2020). Comparison of $NiCo_2O_4$, CoNiAl-LDH, and CoNiAl-LDH@$NiCo_2O_4$ performances as ORR catalysts in MFC cathode. *Renewable Energy*, *154*, 1263–1271. https://doi.org/10.1016/j.renene.2020.03.091

Tan, J., Yu, M., Cai, Z., Lou, X., Wang, J., & Li, Z. (2021). MOF-derived synthesis of MnS/In_2S_3 p-n heterojunctions with hierarchical structures for efficient photocatalytic CO_2 reduction. *Journal of Colloid and Interface Science*, *588*, 547–556. https://doi.org/10.1016/j.jcis.2020.12.110

Tang, W., Li, B., Teng, K., Wang, X., Liu, R., Wu, M., Zhang, L., Ren, P., Zhang, J., & Feng, M. (2022). Advanced noble-metal-free bifunctional electrocatalysts for metal-air batteries. *Journal of Materiomics*, *8*(2), 454–474. https://doi.org/10.1016/j.jmat.2021.07.001

Tkaczyk, A., Mitrowska, K., & Posyniak, A. (2020). Synthetic organic dyes as contaminants of the aquatic environment and their implications for ecosystems: A review. *Science of the Total Environment*, *717*, 137222. https://doi.org/10.1016/j.scitotenv.2020.137222

Touni, A., Papaderakis, A., Karfaridis, D., Banti, A., Mintsouli, I., Lambropoulou, D., & Sotiropoulos, S. (2019). Oxygen evolution at IrO_2-modified Ti anodes prepared by a simple galvanic deposition method. *Journal of Electroanalytical Chemistry*, *855*(July). https://doi.org/10.1016/j.jelechem.2019.113485

Trandafilović, L. V., Jovanović, D. J., Zhang, X., Ptasińska, S., & Dramićanin, M. D. (2017). Enhanced photocatalytic degradation of methylene blue and methyl orange by ZnO:Eu nanoparticles. *Applied Catalysis B: Environmental*, *203*, 740–752. https://doi.org/10.1016/j.apcatb.2016.10.063

Tripkovic, V., Hansen, H. A., & Vegge, T. (2018). Computational Screening of Doped A-MnO_2 Catalysts for the Oxygen Evolution Reaction. *ChemSusChem*, *11*(3), 629–637. https://doi.org/10.1002/cssc.201701659

Varma, A., Mukasyan, A. S., Rogachev, A. S., & Manukyan, K. V. (2016). Solution Combustion Synthesis of Nanoscale Materials. *Chemical Reviews*, *116*(23), 14493–14586. https://doi.org/10.1021/acs.chemrev.6b00279

Vempuluru, N. R., Kanakkampalayam Krishnan, C., Parnapalli, R., Velusamy, J., Marappan, S., Pitchaimuthu, S., Murikinati, M., & Muthukonda Venkatakrishnan, S. (2021). Solar hydrogen generation from organic substance using earth abundant CuS–NiO heterojunction semiconductor photocatalyst. *Ceramics International*, *47*(7), 10206–10215. https://doi.org/10.1016/j.ceramint.2020.12.062

Wang, B., Iocozzia, J., Zhang, M., Ye, M., Yan, S., Jin, H., Wang, S., Zou, Z., & Lin, Z. (2019). The charge carrier dynamics, efficiency and stability of two-dimensional material-based perovskite solar cells. *Chemical Society Reviews*, *48*(18), 4854–4891. https://doi.org/10.1039/c9cs00254e

Wang, H. F., & Xu, Q. (2019). Materials Design for Rechargeable Metal-Air Batteries. *Matter*, *1*(3), 565–595. https://doi.org/10.1016/j.matt.2019.05.008

Wang, L. (2016). Synthetic methods of CuS nanoparticles and their applications for imaging and cancer therapy. *RSC Advances*, *6*(86), 82596–82615. https://doi.org/10.1039/c6ra18355g

Wang, R., Chen, Z., Hu, N., Xu, C., Shen, Z., & Liu, J. (2018). Nanocarbon-Based Electrocatalysts for Rechargeable Aqueous Li/Zn-Air Batteries. *ChemElectroChem*, *5*(14), 1745–1763. https://doi.org/10.1002/celc.201800141

Wang, S. L., Zhu, Y., Luo, X., Huang, Y., Chai, J., Wong, T. I., & Xu, G. Q. (2018). 2D WC/WO_3 Heterogeneous Hybrid for Photocatalytic Decomposition of Organic Compounds with Vis–NIR Light. *Advanced Functional Materials*, *28*(11), 2–9. https://doi.org/10.1002/adfm.201705357

Wang, S., Lu, A., & Zhong, C. J. (2021). Hydrogen production from water electrolysis: role of catalysts. *Nano Convergence*, *8*(1). https://doi.org/10.1186/s40580-021-00254-x

Wang, X. C., Klemeš, J. J., Dong, X., Fan, W., Xu, Z., Wang, Y., & Varbanov, P. S. (2019). Air pollution terrain nexus: A review considering energy generation and consumption. *Renewable and Sustainable Energy Reviews*, *105*(December 2018), 71–85. https://doi.org/10.1016/j.rser.2019.01.049

Wang, Y., Gan, R., Zhao, S., Ma, W., Zhang, X., Song, Y., Ma, C., & Shi, J. (2022). B, N, F tri-doped lignin-derived carbon nanofibers as an efficient metal-free bifunctional electrocatalyst for ORR and OER in rechargeable liquid/solid-state Zn-air batteries. *Applied Surface Science*, *598*(April), 153891. https://doi.org/10.1016/j.apsusc.2022.153891

Wei, C., & Xu, Z. J. (2022). The possible implications of magnetic field effect on understanding the reactant of water splitting. *Chinese Journal of Catalysis*, *43*(1), 148–157. https://doi.org/10.1016/S1872-2067(21)63821-4

Wei, L., Zhang, J., & Ruan, M. (2021). Combined CdS/In_2S_3 heterostructures with cocatalyst for boosting carriers separation and photoelectrochemical water splitting. *Applied Surface Science*, *541*(November 2020), 148431. https://doi.org/10.1016/j.apsusc.2020.148431

Wodrich, M. D., Sawatlon, B., Busch, M., & Corminboeuf, C. (2021). The Genesis of Molecular Volcano Plots. *Accounts of Chemical Research*, *54*(5), 1107–1117. https://doi.org/10.1021/acs.accounts.0c00857

Xie, Y., Feng, C., Guo, Y., Hassan, A., Li, S., Zhang, Y., & Wang, J. (2022). Dimethylimidazole and dicyandiamide assisted synthesized rich-defect and highly dispersed CuCo-Nx anchored hollow graphite carbon nanocages as efficient trifunctional electrocatalyst in the same electrolyte. *Journal of Power Sources*, *517*(March 2021), 230721. https://doi.org/10.1016/j.jpowsour.2021.230721

Xiong, M., & Ivey, D. G. (2019). Synthesis of Bifunctional Catalysts for Metal-Air Batteries Through Direct Deposition Methods. *Batteries and Supercaps*, *2*(4), 326–335. https://doi.org/10.1002/batt.201800069

Xu, A., Li, X., Ye, S., Yin, G., & Zeng, Q. (2011). Catalyzed oxidative degradation of methylene blue by in situ generated cobalt (II)-bicarbonate complexes with hydrogen peroxide. *Applied Catalysis B: Environmental*, *102*(1–2), 37–43. https://doi.org/10.1016/j.apcatb.2010.11.022

Xueref, I., & Dominé, F. (2003). FTIR spectroscopic studies of the simultaneous condensation of HCl and H_2O at 190K - Atmospheric applications. *Atmospheric Chemistry and Physics*, *3*(5), 1779–1789. https://doi.org/10.5194/acp-3-1779-2003

Yadav, S., Shrivas, K., & Bajpai, P. K. (2019). Role of precursors in controlling the size, shape and morphology in the synthesis of copper sulfide nanoparticles and their application for fluorescence detection. *Journal of Alloys and Compounds*, *772*, 579–592. https://doi.org/10.1016/j.jallcom.2018.08.132

Yang, H. H., Du, J., Wu, M., Zhou, H., Yi, X., Zhan, J., & Liu, Y. (2022). Tin-Modified α-MnO_2 catalyst with high performance for benzene Oxidation, ozone decomposition and particulate matter filtration. *Chemical Engineering Journal*, *427*(June 2021), 132075. https://doi.org/10.1016/j.cej.2021.132075

Yang, Jing, Guo, D., Zhao, S., Lin, Y., Yang, R., Xu, D., Shi, N., Zhang, X., Lu, L., Lan, Y. Q., Bao, J., & Han, M. (2019). Cobalt Phosphides Nanocrystals Encapsulated by P-Doped Carbon and Married with P-Doped Graphene for Overall Water Splitting. *Small*, *15*(10), 1–12. https://doi.org/10.1002/smll.201804546

Yang, Jiqian, Zhou, X., Wu, D., Zhao, X., & Zhou, Z. (2017a). S-Doped N-Rich Carbon Nanosheets with Expanded Interlayer Distance as Anode Materials for Sodium-Ion Batteries. *Advanced Materials*, *29*(6). https://doi.org/10.1002/adma.201604108

Yang, Jiqian, Zhou, X., Wu, D., Zhao, X., & Zhou, Z. (2017b). S-Doped N-Rich Carbon Nanosheets with Expanded Interlayer Distance as Anode Materials for Sodium-Ion Batteries. *Advanced Materials*, *29*(6), 1–5. https://doi.org/10.1002/adma.201604108

Yang, S., Xu, C. Y., Zhang, B. Y., Yang, L., Hu, S. P., & Zhen, L. (2017). Ca(II) doped β-In_2S_3 hierarchical structures for photocatalytic hydrogen generation and organic dye degradation under visible light irradiation. *Journal of Colloid and Interface Science*, *491*, 230–237. https://doi.org/10.1016/j.jcis.2016.12.028

Yao, B., Xiao, T., Makgae, O. A., Jie, X., Gonzalez-Cortes, S., Guan, S., Kirkland, A. I., Dilworth, J. R., Al-Megren, H. A., Alshihri, S. M., Dobson, P. J., Owen, G. P., Thomas, J. M., & Edwards, P. P. (2020). Transforming carbon dioxide into jet fuel using an organic combustion-synthesized Fe-Mn-K catalyst. *Nature Communications*, *11*(1). https://doi.org/10.1038/s41467-020-20214-z

Yoo, J. H., Ji, M., Kim, J. H., Ryu, C. H., & Lee, Y. I. (2020). Facile synthesis of hierarchical CuS microspheres with high visible-light-driven photocatalytic activity. *Journal of Photochemistry and Photobiology A: Chemistry*, *401*(May), 112782. https://doi.org/10.1016/j.jphotochem.2020.112782

Yu, T., Zhao, Z., Sun, Y., Bergara, A., Lin, J., Zhang, S., Xu, H., Zhang, L., Yang, G., & Liu, Y. (2019). Two-Dimensional PC 6 with Direct Band Gap and Anisotropic Carrier Mobility. *Journal of the American Chemical Society*, *141*(4), 1599–1605. https://doi.org/10.1021/jacs.8b11350

Yuan, S., Duan, X., Liu, J., Ye, Y., Lv, F., Liu, T., Wang, Q., & Zhang, X. (2021). Recent progress on transition metal oxides as advanced materials for energy conversion and storage. *Energy Storage Materials*, *42*(July), 317–369. https://doi.org/10.1016/j.ensm.2021.07.007

Zeng, X., Li, M., Abd El-Hady, D., Alshitari, W., Al-Bogami, A. S., Lu, J., & Amine, K. (2019). Commercialization of Lithium Battery Technologies for Electric Vehicles. *Advanced Energy Materials*, *9*(27). https://doi.org/10.1002/aenm.201900161

Zeng, Z., Liu, Y., Zhang, W., Chevva, H., & Wei, J. (2017). Improved supercapacitor performance of MnO_2-electrospun carbon nanofibers electrodes by mT magnetic field. *Journal of Power Sources*, *358*, 22–28. https://doi.org/10.1016/j.jpowsour.2017.05.008

Zeng, Z., Zhang, T., Liu, Y., Zhang, W., Yin, Z., Ji, Z., & Wei, J. (2018). Magnetic Field-Enhanced 4-Electron Pathway for Well-Aligned Co_3O_4/Electrospun Carbon Nanofibers in the Oxygen Reduction Reaction. *ChemSusChem*, *11*(3), 580–588. https://doi.org/10.1002/cssc.201701947

Zhan, Z., An, J., Zhang, H., Hansen, R. V., & Zheng, L. (2014). Three-dimensional plasmonic photoanodes based on Au-embedded TiO_2 structures for enhanced visible-light water splitting. *ACS Applied Materials and Interfaces*, *6*(2), 1139–1144. https://doi.org/10.1021/am404738a

Zhang, H. T., Wu, G., & Chen, X. H. (2006). Controlled synthesis and characterization of covellite (CuS) nanoflakes. *Materials Chemistry and Physics*, *98*(2–3), 298–303. https://doi.org/10.1016/j.matchemphys.2005.09.024

Zhang, L., Hu, X., Wang, Z., Sun, F., & Dorrell, D. G. (2018). A review of supercapacitor modeling, estimation, and applications: A control/management perspective. *Renewable and Sustainable Energy Reviews*, *81*(June 2016), 1868–1878. https://doi.org/10.1016/j.rser.2017.05.283

Zhang, Q., & Guan, J. (2021). Applications of Atomically Dispersed Oxygen Reduction Catalysts in Fuel Cells and Zinc–Air Batteries. *Energy and Environmental Materials*, *4*(3), 307–335. https://doi.org/10.1002/eem2.12128

Zhang, X., Tian, F., Qiu, L., Gao, M., Yang, W., Liu, Y., & Yu, Y. (2021). Z-Scheme $Mo_2C/MoS_2/In_2S_3$dual-heterojunctions for the photocatalytic reduction of Cr(vi). *Journal of Materials Chemistry A*, *9*(16), 10297–10303. https://doi.org/10.1039/d1ta00999k

Zhang, Y. L., Goh, K., Zhao, L., Sui, X. L., Gong, X. F., Cai, J. J., Zhou, Q. Y., Zhang, H. Da, Li, L., Kong, F. R., Gu, D. M., & Wang, Z. B. (2020a). Advanced non-noble materials in bifunctional catalysts for ORR and OER toward aqueous metal-air batteries. *Nanoscale*, *12*(42), 21534–21559. https://doi.org/10.1039/d0nr05511e

Zhang, Y. L., Goh, K., Zhao, L., Sui, X. L., Gong, X. F., Cai, J. J., Zhou, Q. Y., Zhang, H. Da, Li, L., Kong, F. R., Gu, D. M., & Wang, Z. B. (2020b). Advanced non-noble materials in bifunctional catalysts for ORR and OER toward aqueous metal-air batteries. *Nanoscale*, *12*(42), 21534–21559. https://doi.org/10.1039/d0nr05511e

Zhang, Yuanjian, Schnepp, Z., Cao, J., Ouyang, S., Li, Y., Ye, J., & Liu, S. (2013). Biopolymer-activated graphitic carbon nitride towards a sustainable photocathode material. *Scientific Reports*, *3*, 1–5. https://doi.org/10.1038/srep02163

Zhang, Yuanyuan, Guo, P., Li, S., Sun, J., Wang, W., Song, B., Yang, X., Wang, X., Jiang, Z., Wu, G., & Xu, P. (2022). Magnetic field assisted electrocatalytic oxygen evolution reaction of nickel-based materials. *Journal of Materials Chemistry A*, *10*(4), 1760–1767. https://doi.org/10.1039/d1ta09444k

Zhang, Z., Ding, T., Zhou, Q., Sun, Y., Qu, M., Zeng, Z., Ju, Y., Li, L., Wang, K., & Chi, F. (2021). A review of technologies and applications on versatile energy storage systems. *Renewable and Sustainable Energy Reviews*, *148*(May). https://doi.org/10.1016/j.rser.2021.111263

Zhao, S., Li, K., Du, J., Song, C., & Guo, X. (2021). Facile Construction of a Hollow In_2S_3/Polymeric Carbon Nitride Heterojunction for Efficient Visible-Light-Driven CO_2 Reduction. *ACS Sustainable Chemistry and Engineering*, *9*(17), 5942–5951. https://doi.org/10.1021/acssuschemeng.1c00319

Zhao, Z., Cao, Y., Yi, J., He, X., Ma, C., & Qiu, J. (2012). Band-edge electronic structure of β-In_2S_3: The role of s or p orbitals of atoms at different lattice positions. *ChemPhysChem*, *13*(6), 1551–1556. https://doi.org/10.1002/cphc.201100968

Zhou, Jiacheng, Cao, L., Wang, Q., Tariq, M., Xue, Y., Zhou, Z., Sun, W., & Yang, J. (2019). Enhanced HgO removal via α-MnO_2 anchored to MIL-96(Al). *Applied Surface Science*, *483*(August 2018), 252–259. https://doi.org/10.1016/j.apsusc.2019.03.261

Zhou, Jianqing, Yu, L., Zhou, Q., Huang, C., Zhang, Y., Yu, B., & Yu, Y. (2021). Ultrafast fabrication of porous transition metal foams for efficient electrocatalytic water splitting. *Applied Catalysis B: Environmental*, *288*(November 2020). https://doi.org/10.1016/j.apcatb.2021.120002

APPENDIX A: CHARACTRIZATION OF THE MICROWAVE SYNTHESIZED COPPER SULFIDE, INDIUM SULFIDE, AND THE CORE-SHELL INSTALLATIONTABLES

Figure A. S2.1. Elementary spectra and distribution images of (a) In_2S_3; (b) CuS; (c) 5wt% CuS@In_2S_3 installation; (d) 10wt% CuS@In_2S_3 installation; (e) 15wt% CuS@In_2S_3 installation.

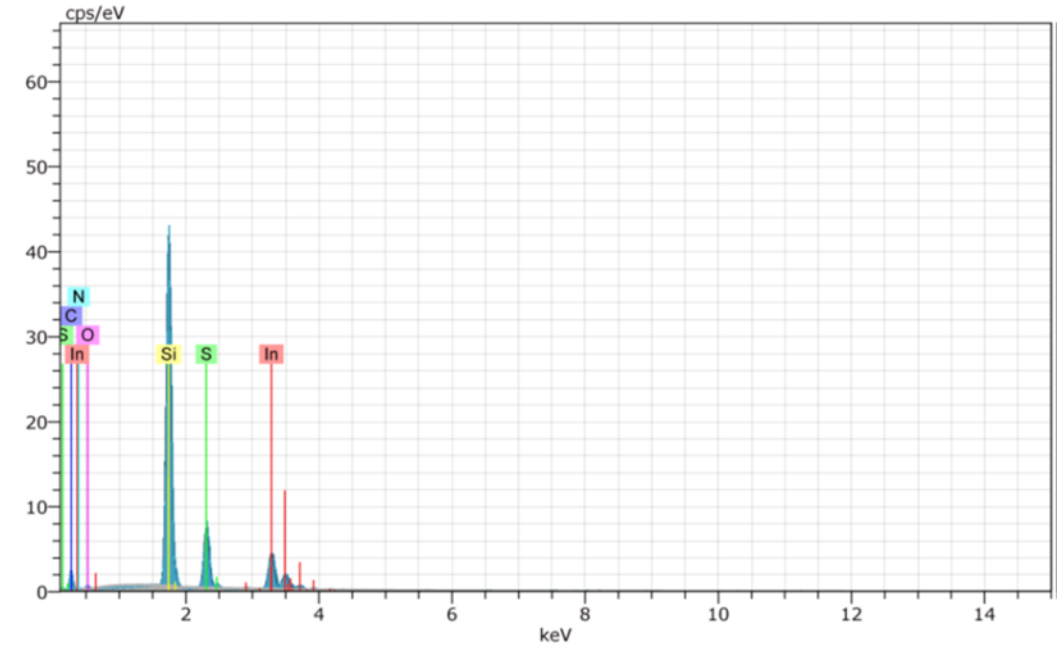

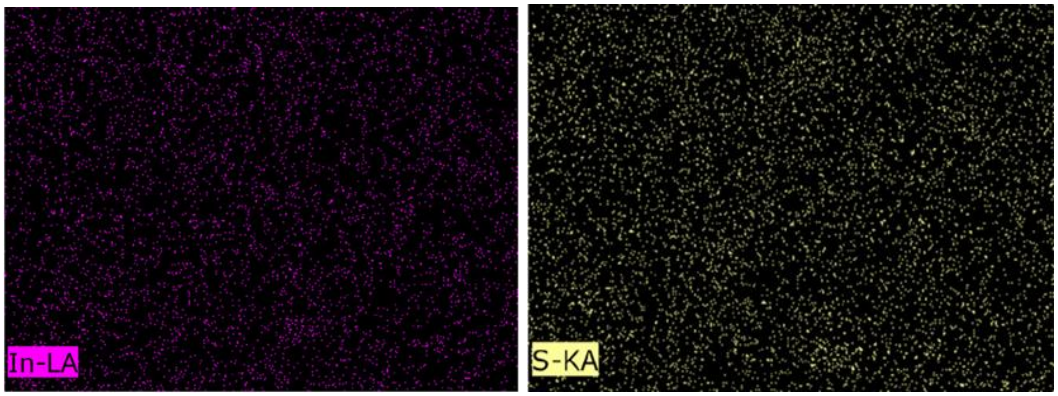

a.

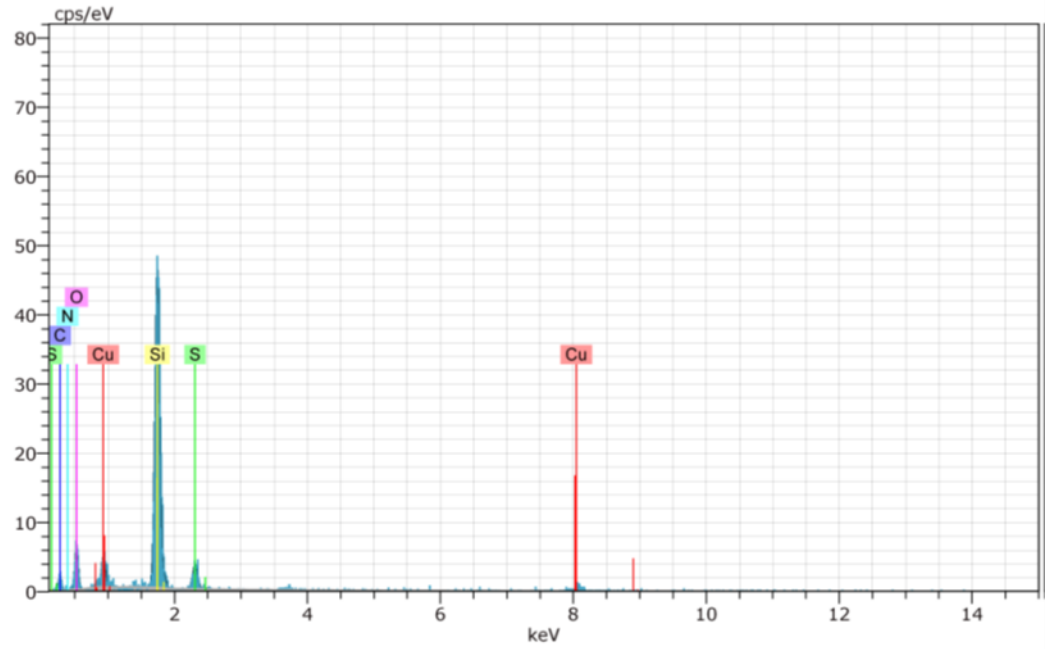
cps/eV
80
70
60
50
40
30
20
10
0
O
N
C
S
Cu
Si
S
Cu
2
4
6
8
10
12
14
keV

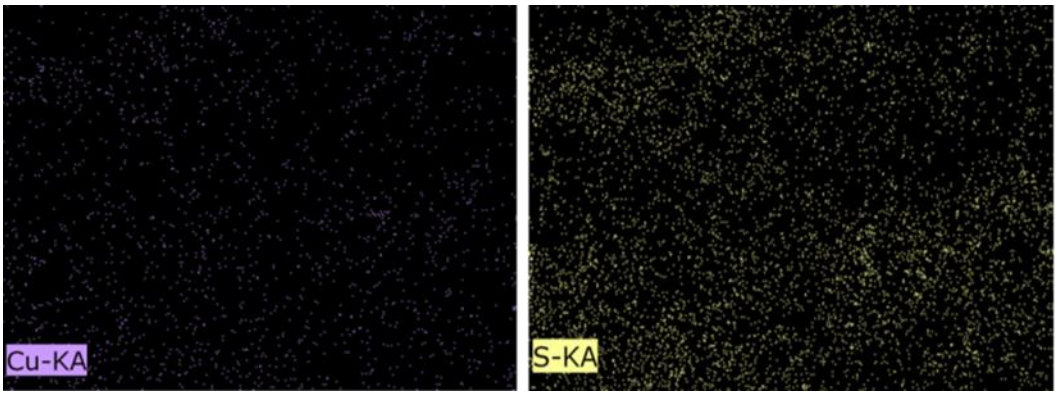
Cu-KA
S-KA

b.

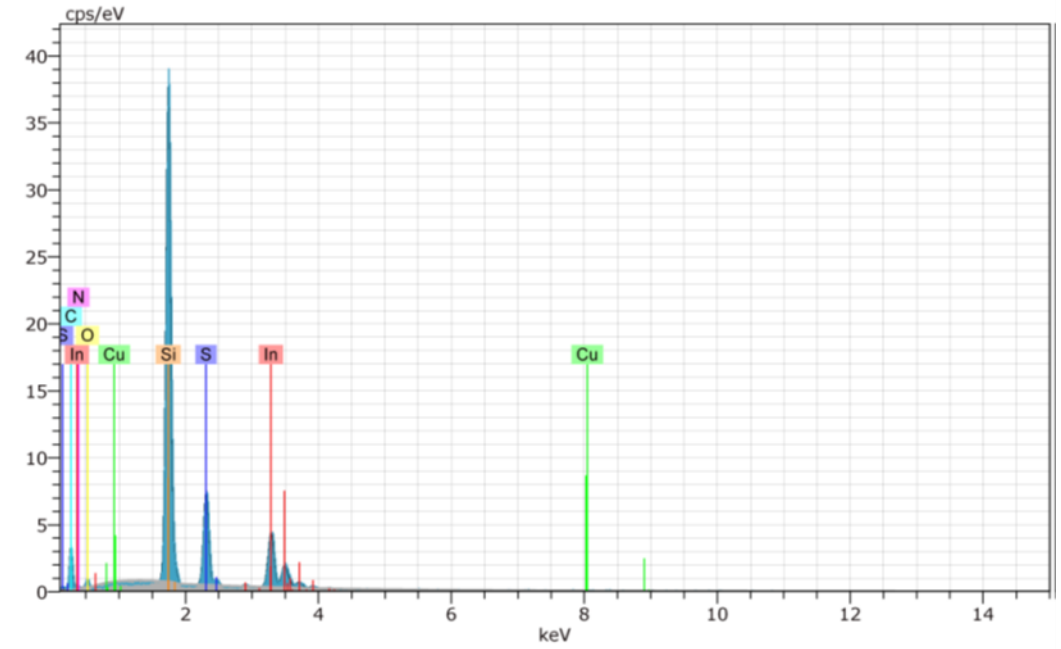
cps/eV
40
35
30
25
20
15
10
5
0
N
C
S
O
In
Cu
Si
S
In
Cu
2
4
6
8
10
12
14
keV

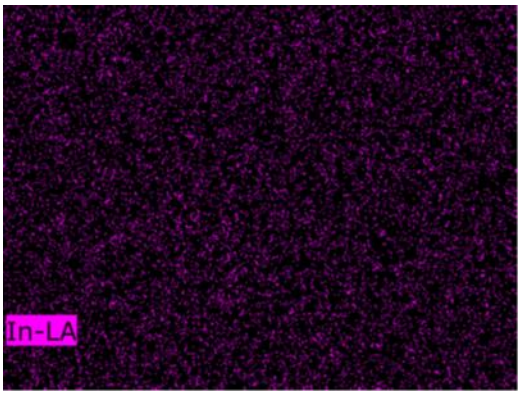
In-LA


Cu-KA

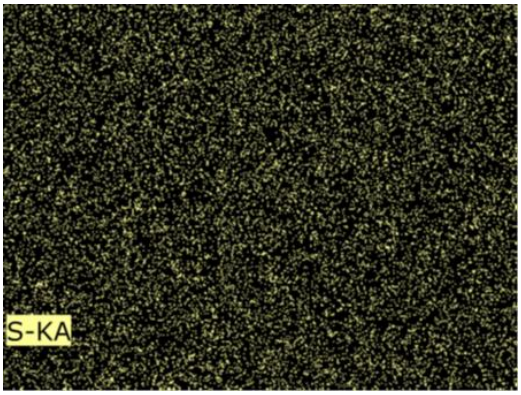
S-KA

c.

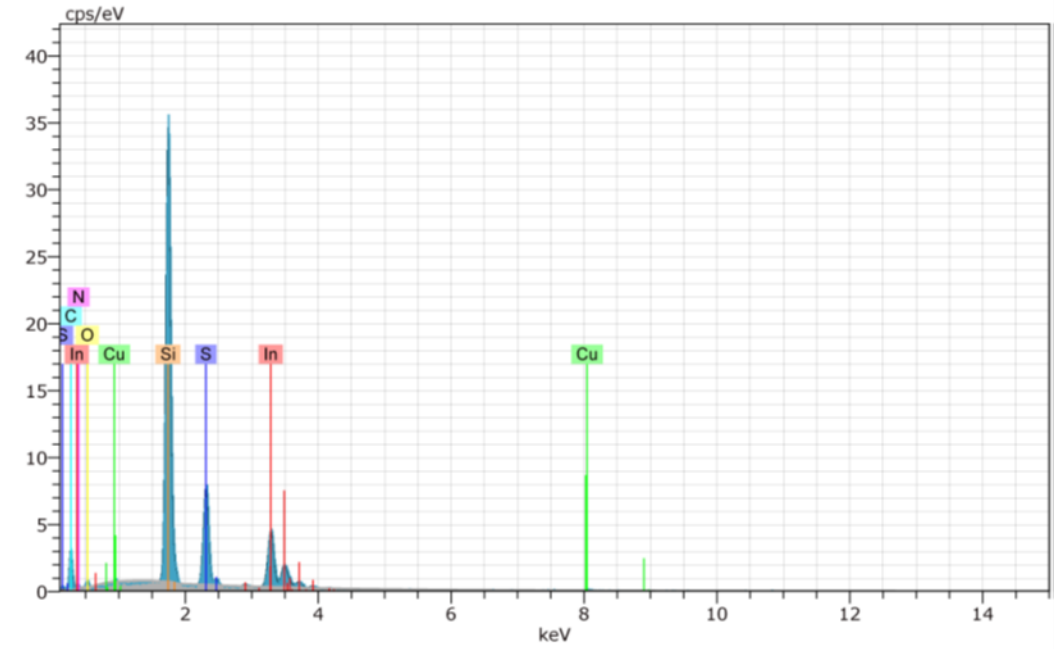
cps/eV
40
35
30
25
20
15
10
5
0
N
C
S
O
In
Cu
Si
S
In
Cu
2
4
6
8
10
12
14
keV

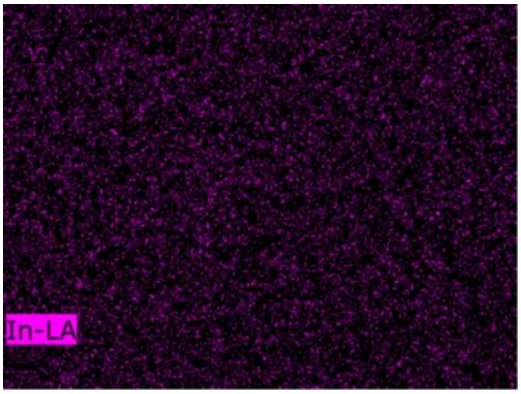
In-LA


Cu-KA

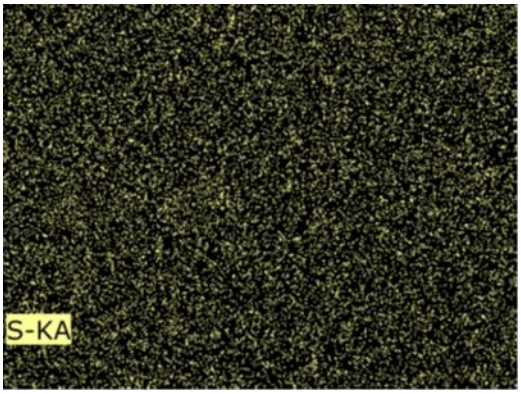
S-KA

d.

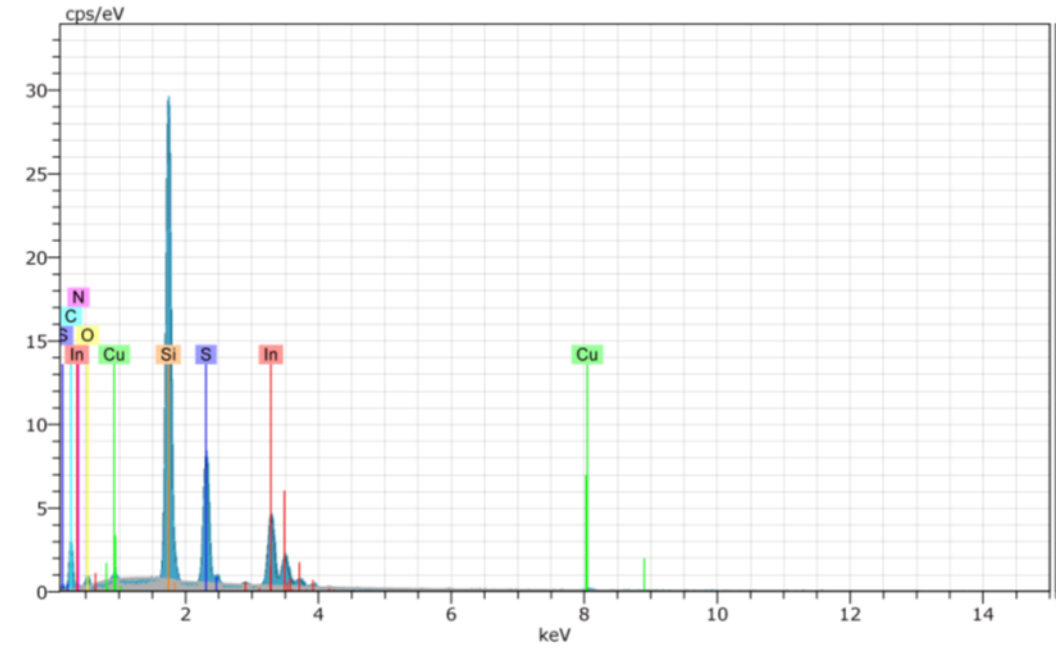
cps/eV
30
25
20
15
10
5
0
N
C
O
In
Cu
Si
S
In
Cu
2
4
6
8
10
12
14
keV

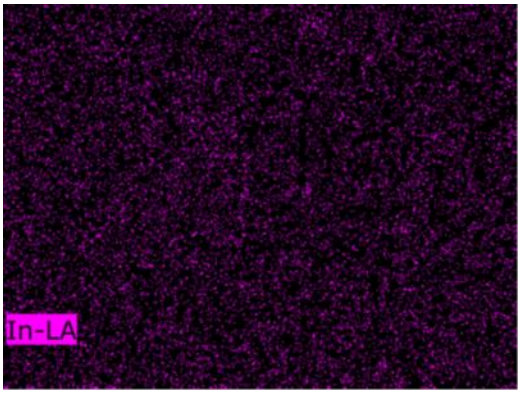
In-LA


Cu-KA

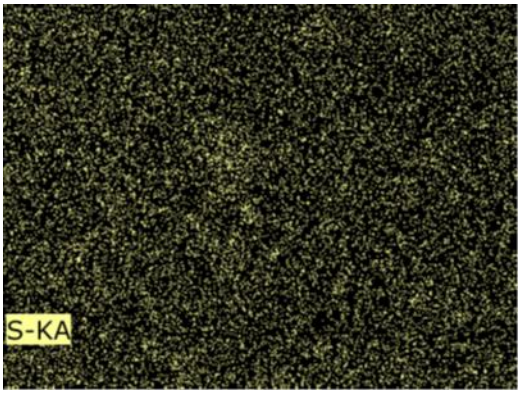
S-KA

e.

Figure A. S2.2. Convoluted full XPS spectra of different samples.

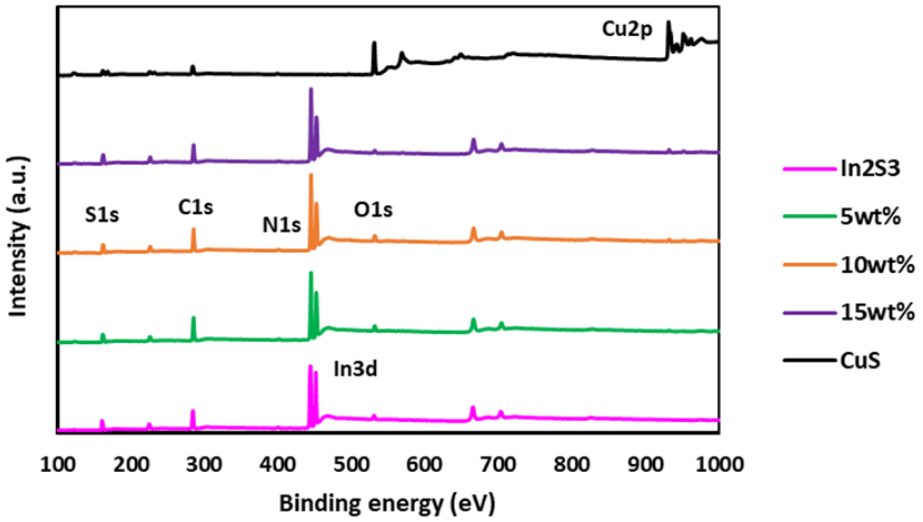

Figure A. S2.3a. Deconvoluted XPS spectra of In; **b.** Cu; **c.** S; **d.** C; **e.** O; and **f.** N in different samples.

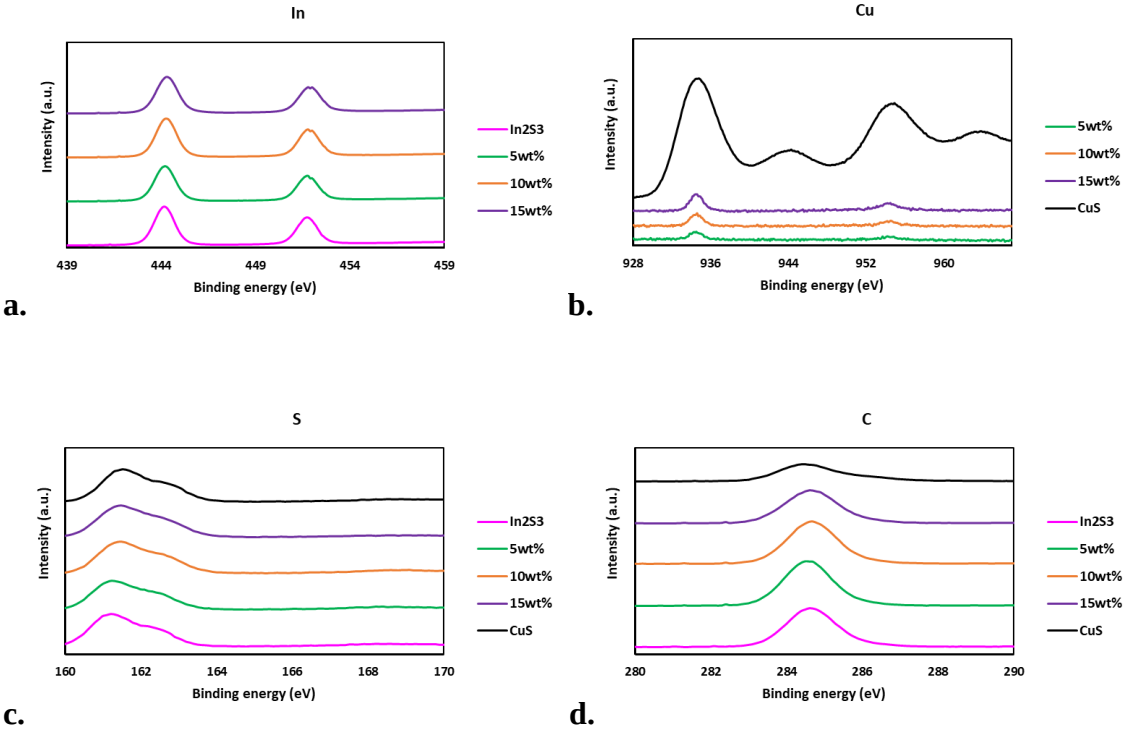

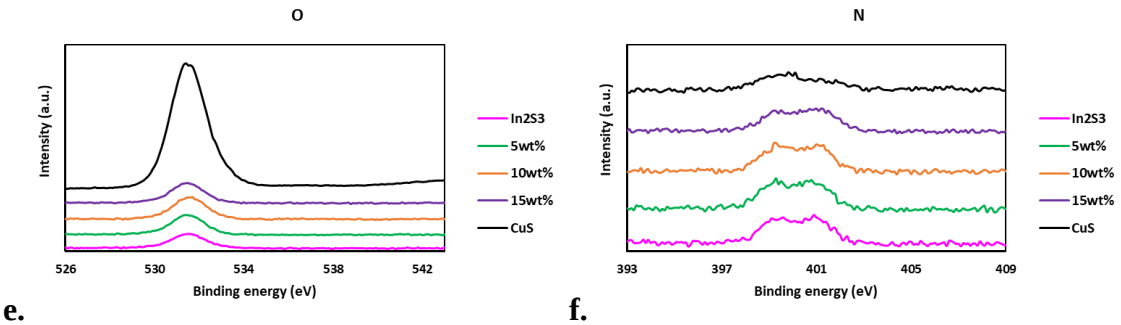

e. **f.**

Figure A. S2.4a. Size distribution of the CuS NPs; **b.** 10% (wt) CuS@ In_2S_3 core-shell NPs.

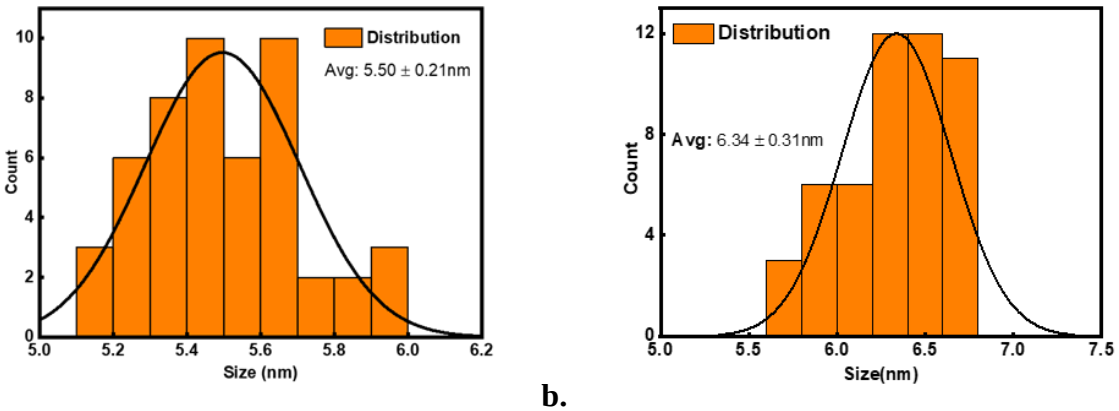

a. **b.**

Table A. S2.1. A comparison of the synthesis of In_2S_3 and its heterojunction structure.

Reference	**Sample characteristics**	**Method**	**Reaction temperature (°C)**	**Reaction time**
(H. Cui et al., 2021)	In_2S_3/Bi_2MoO_6 heterojunction nanoparticles	Hydrothermal	180	24 hrs

(Horani & Lifshitz, 2019)	β/γ-In_2S_3 nanoplatelets	Colloidal procedure	230-250	192 mins
(D. Ma et al., 2020)	Cu doped In_2S_3 nanorod	Solvothermal	110-240	4 hrs
(X. Zhang et al., 2021)	$Mo_2C/MoS_2/In_2S_3$ heterostructure	Hydrothermal	240	24 hrs
(M. Liu et al., 2021)	In_2S_3/In_2O_3 heterostructures	Solvothermal	150	>12 hrs
(Tan et al., 2021)	MnS/In_2S_3 heterojunctions	Solvothermal	180	3 hrs
(Feng et al., 2018)	Sn doped In_2S_3 microsphere	Hydrothermal	160	16 hrs
(X. Li et al., 2021)	In_2S_3/Au/reduced graphene oxide (rGO) photocatalyst	Hydrothermal	160	12 hrs
(S. Zhao et al., 2021)	In_2S_3/Polymeric carbon nitride heterojunction	Solvothermal	180	8 hrs
This work	CuS/In_2S_3 hybridization	Solvothermal	185	~35 mins

Table A. S2.2. Summary of XRD information of the In_2S_3 and CuS NPs.

β-In_2S_3			**γ-In_2S_3**			**CuS**		
2Θ °	**Plane**	**d (Å)**	**2Θ °**	**Plane**	**d (Å)**	**2Θ °**	**Plane**	**d (Å)**
27.64	(109)	3.22	**27.26**	(110)	3.27	**27.12**	(101)	3.29
28.44	(206)	3.14	**48.50**	(300)	1.88	**28.90**	(102)	3.09
33.28	(00$\underline{1}$2)	2.69	-	-	-	**34.57**	(106)	2.59
41.08	(20$\underline{1}$2)	2.20	-	-	-	**41.36**	(105)	2.18
43.38	(309)	2.08	-	-	-	**45.77**	(110)	1.98
47.97	(22$\underline{1}$2)	1.89	-	-	-	**47.68**	(107)	1.91
85.32	(549)	1.13	-	-	-	**63.24**	(205)	1.47
98.41	(00$\underline{3}$2)	1.02	-	-	-	**81.84**	(00$\underline{1}$4)	1.18
-	-	-	-	-	-	**82.58**	(3-15)	1.17
-	-	-	-	-	-	**87.89**	(2-1$\underline{1}$2)	1.11
						98.50	(306)	1.02

APPENDIX B: PHOTOCATALYTIC PERFORMANCE OF THE MICROWAVE SYNTHESIZED COPPER SULFIDE, INDIUM SULFIDE, AND THE CORE-SHELL INSTALLATION ADD TITLE OF APPENDIX

Figure B. S3.1. UV-vis absorption spectra of MB versus the function of reaction time with **a.** bare In_2S_3; **b.** 5wt% CuS; **c.**10wt% CuS; **d.**15wt% CuS; **e.** pristine CuS NPs.

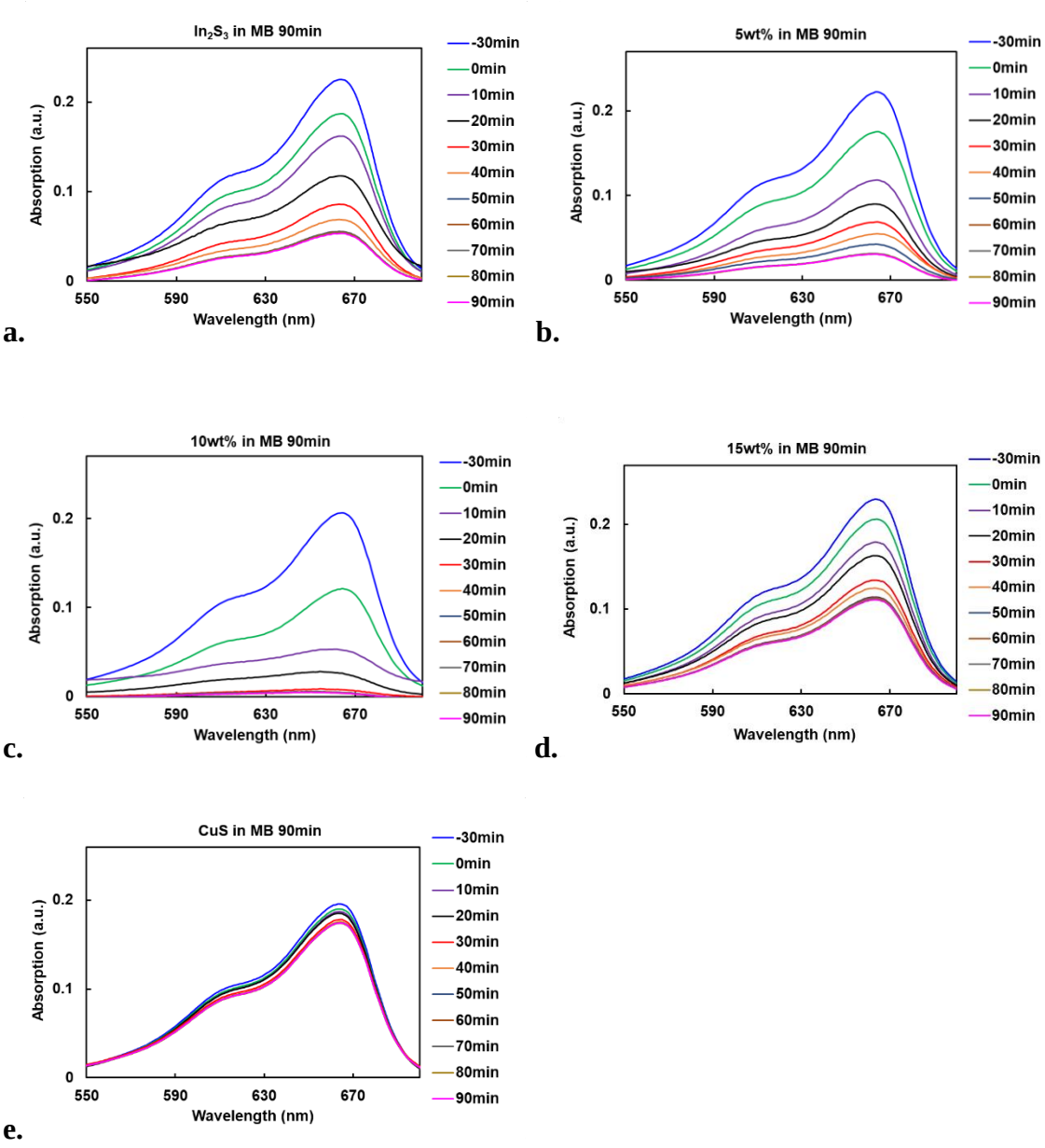

Figure B. S3.2. UV-vis absorption spectra of MO versus the function of reaction time with **a.** bare In_2S_3; **b.** 5wt% CuS; **c.**10wt% CuS; **d.**15wt% CuS; **e.** pristine CuS NPs.

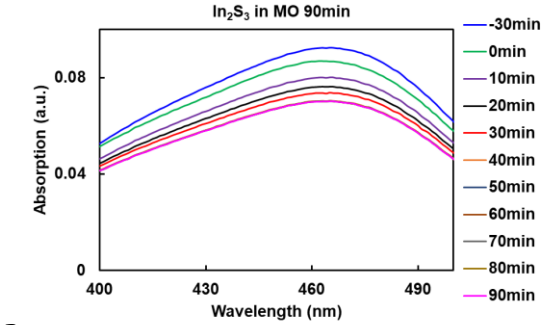

a.

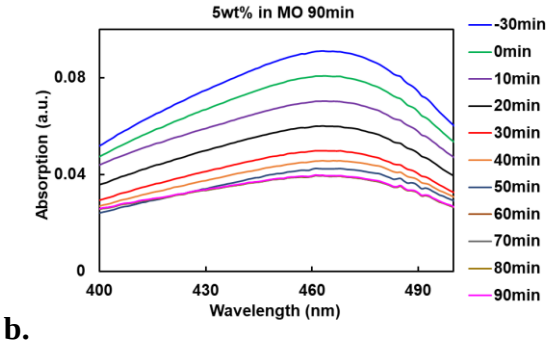

b.

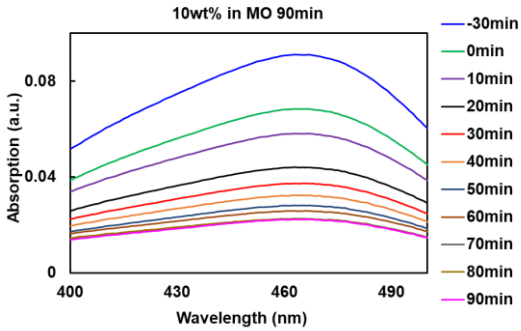

c.

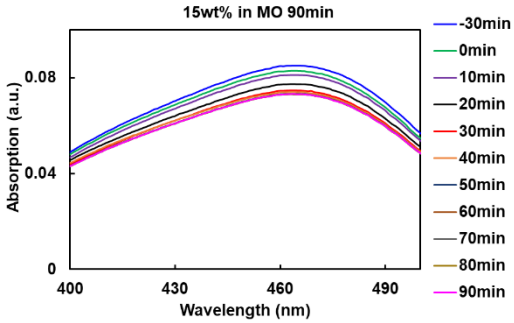

d.

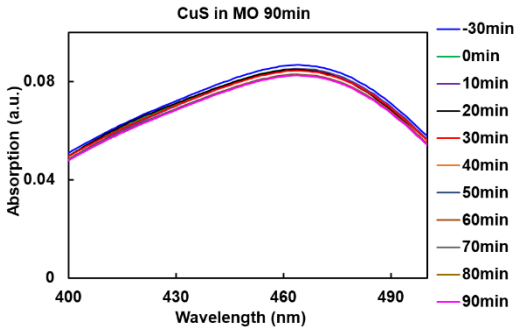

e.

Figure B. S3.3a. UV-vis absorption spectra of MB solution versus the function of time t with 10wt% NPs without light irradiation; **b.** UV-vis absorption spectra of MO solution versus the function of time t with 10wt% NPs without light irradiation.

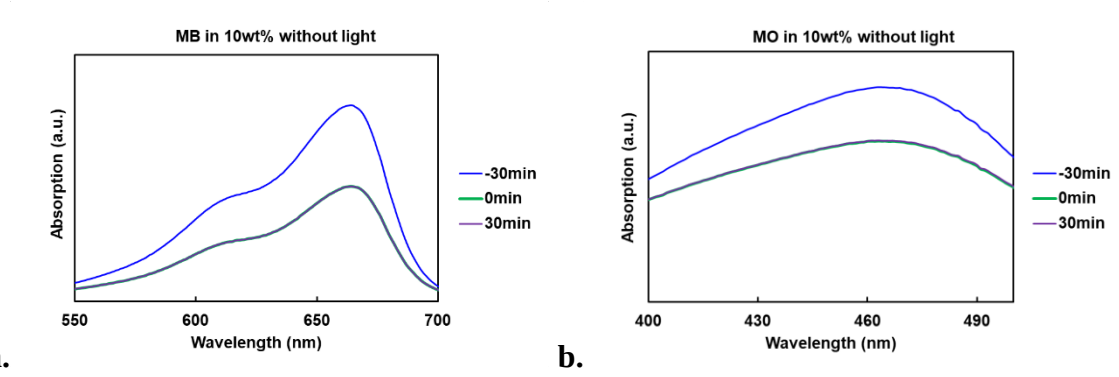

Figure B. S3.4a. UV-vis absorption spectra of MB solution versus the function of reaction time under light irradiation without NPs; **b.** UV-vis absorption spectra of MO solution versus the function of reaction time under the light irradiation without NPs.

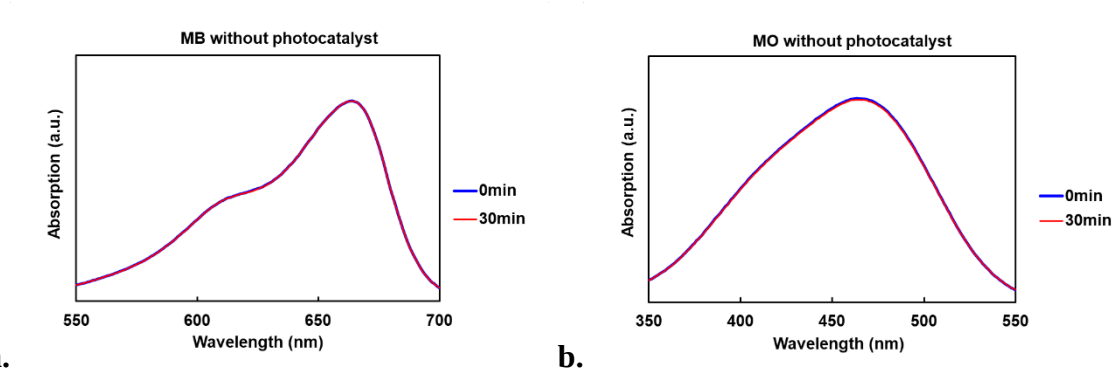

Figure B. S3.5. Photodegradation efficiency of the selected NPs versus irradiation time. Normalized concentration of MB **a**) and MO **b**) vs. time up to 90 min.

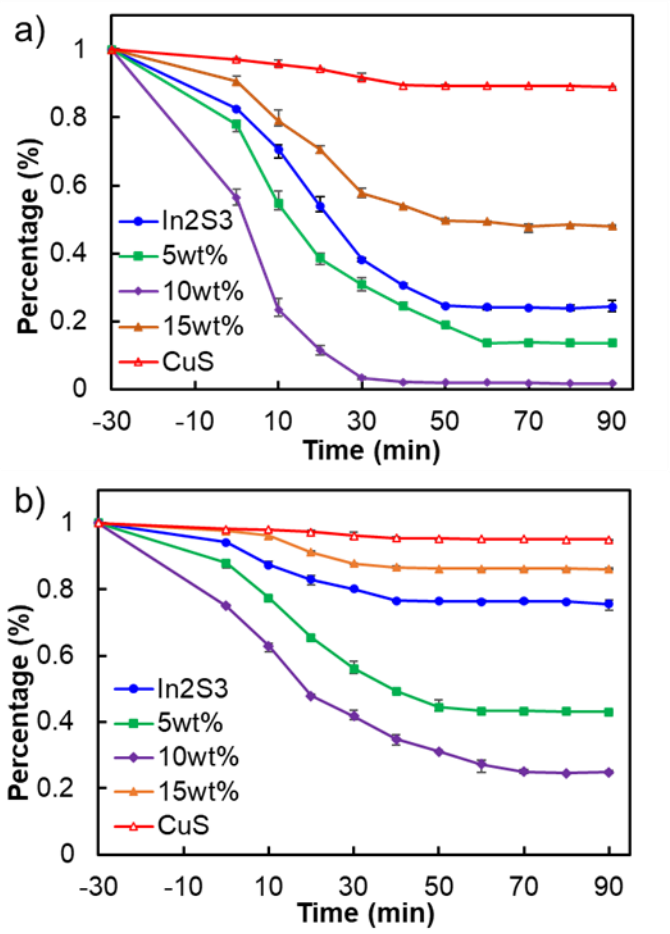

Figure B. S3.6. Zeta potential of **a.** bare In_2S_3; **b.** 5wt% CuS; **c.**10wt% CuS; **d.**15wt% CuS; **e.** pristine CuS NPs.

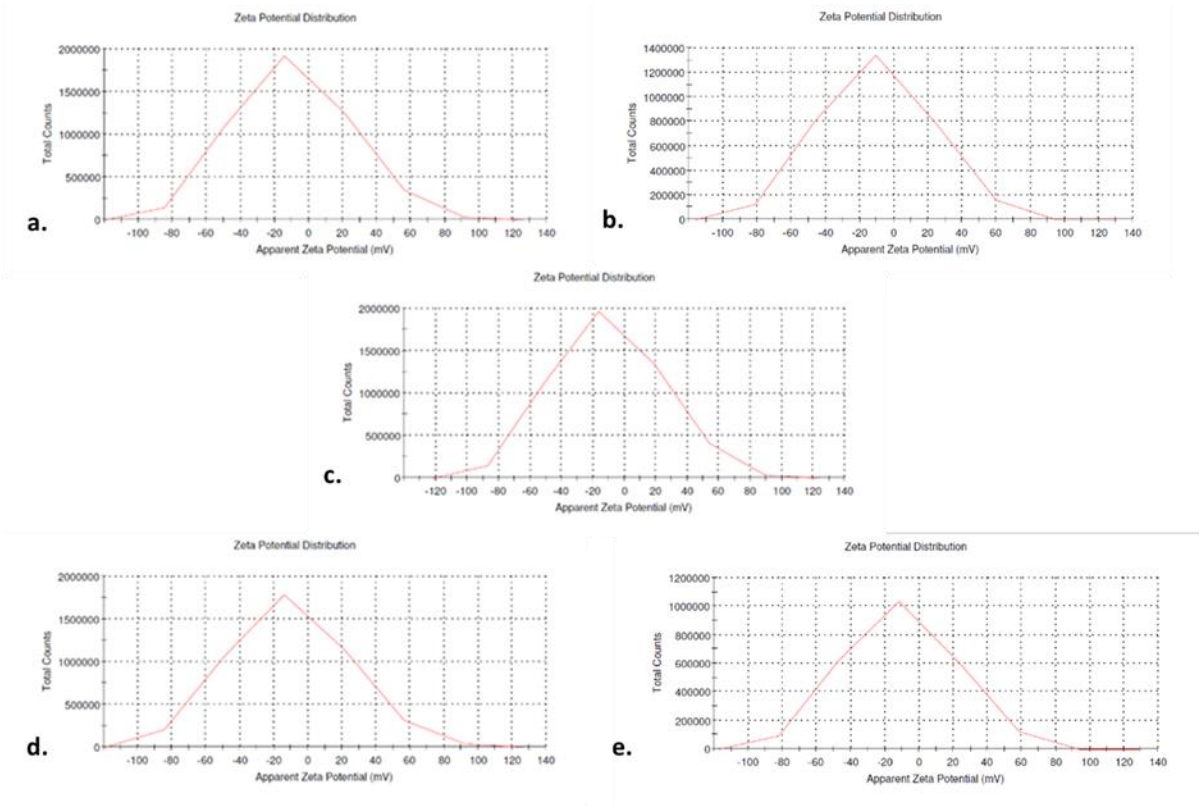

APPENDIX C: THE OXYGEN EVOLUTION PERFORMANCE OF ALPHA-MANGNESESE OXIDE ELECTRODEPOSITED SUPER-ALIGNED CARBON NANO FIBERS UNDER AN INFLUENCE OF EXTERNAL MAGNETIC FIELD

Figure C. S5.1. SEM images (38600×) **(a)** bare SA-CNFs; **(b)** 5-MnO_2@SA-CNFs; **(c)** 10-MnO_2@SA-CNFs; **(d)** 15-MnO_2@SA-CNFs.

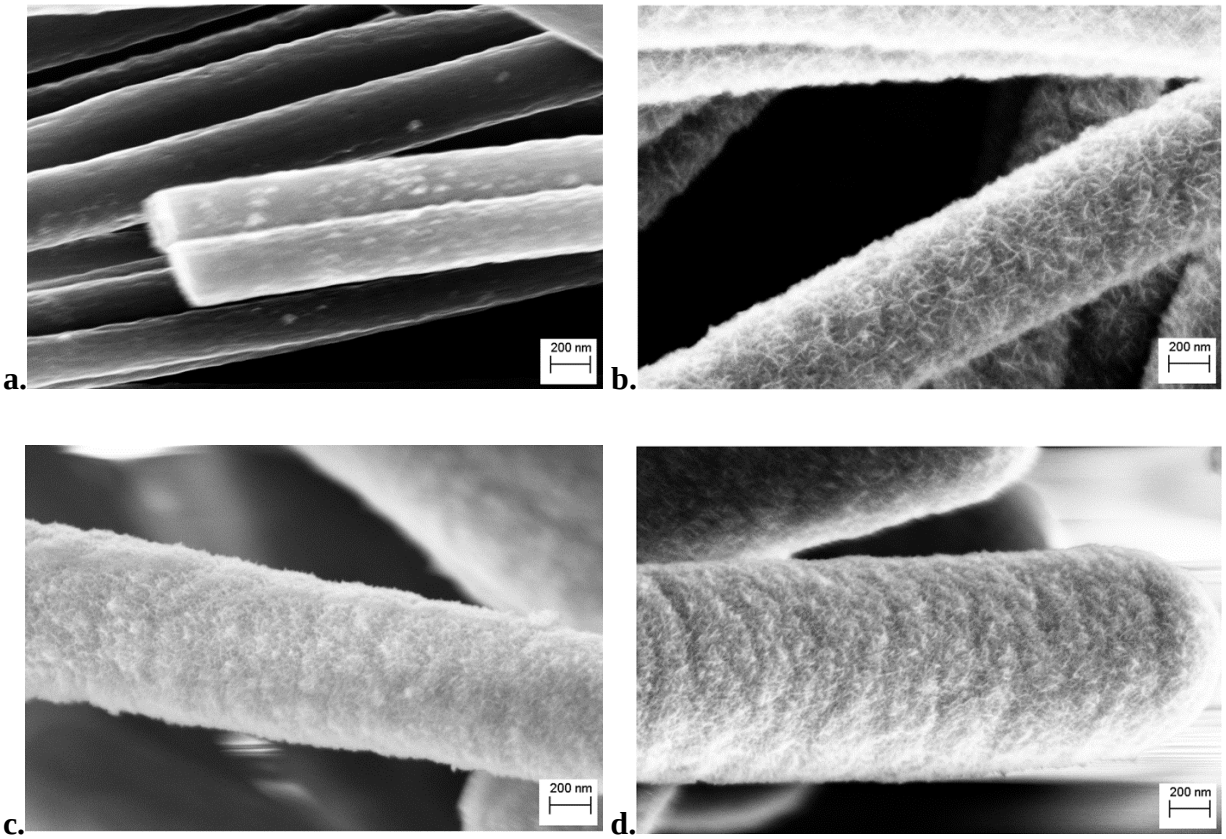

Table C. S5.1. Thickness summary of different samples.

Sample	Thickness (µm)	Increase % (Vs. Bare CNFs)
SA-CNFs	25.82 ± 0.53	-
5-MnO_2@SA-CNFs	62.95 ± 0.81	143.8
10-MnO_2@SA-CNFs	95.18 ± 0.69	268.6
15-MnO_2@SA-CNFs	162.80 ± 1.02	530.5

Figure C. S5.2. Thickness distribution of SA-CNFs **(a)**, 5-MnO_2@SA-CNFs **(b)**, 10-MnO_2@SA-CNFs **(c)**, 15-MnO_2@SA-CNFs **(d)**.

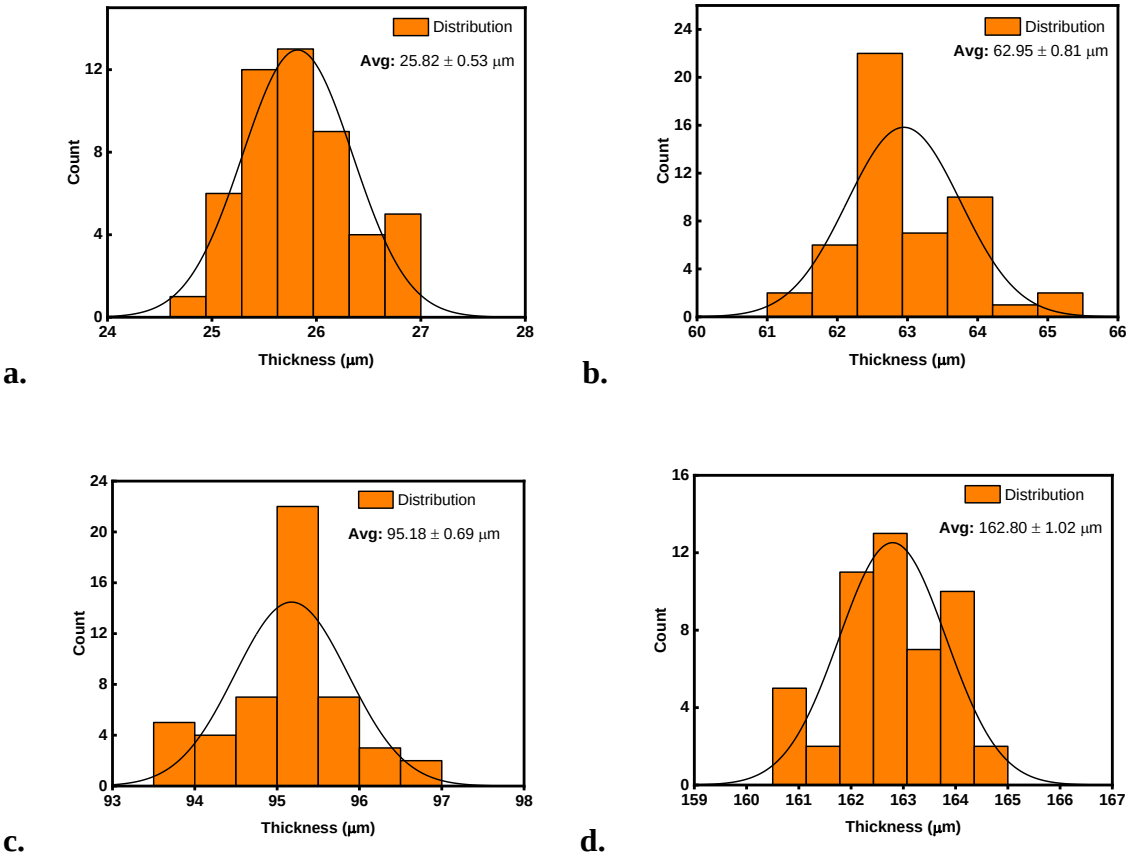

Figure C. S5.3. EDX elemental distribution maps of SA-CNFs **(a)**, 5-MnO_2@SA-CNFs **(b)**, 10-MnO_2@SA-CNFs **(c)**, 15-MnO_2@SA-CNFs **(d)**.

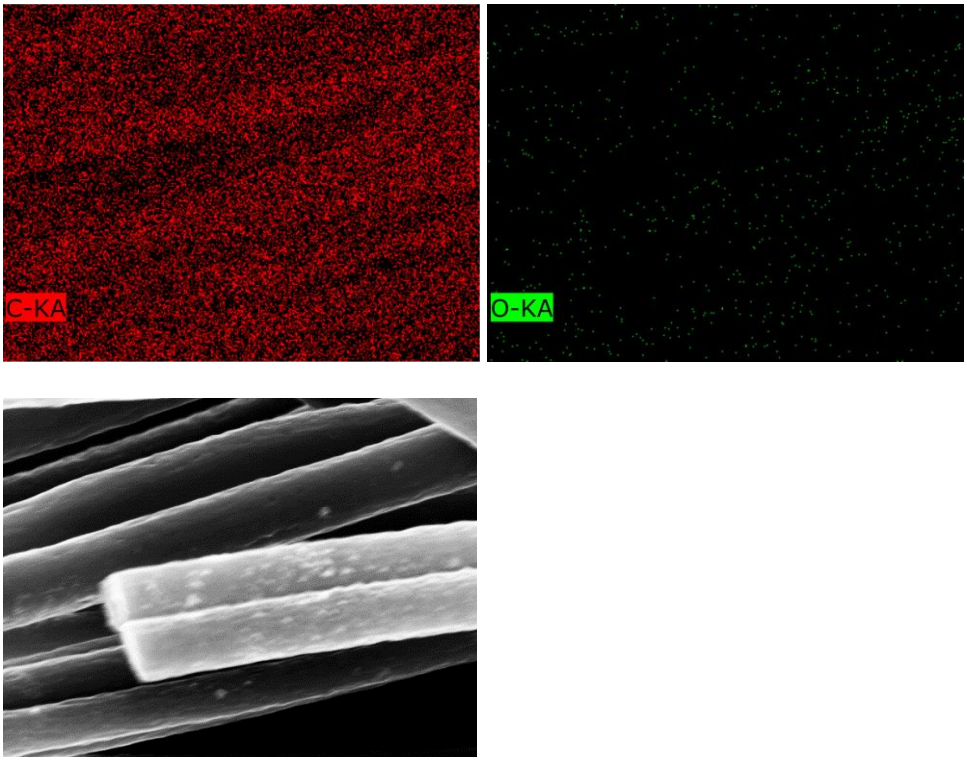

a.

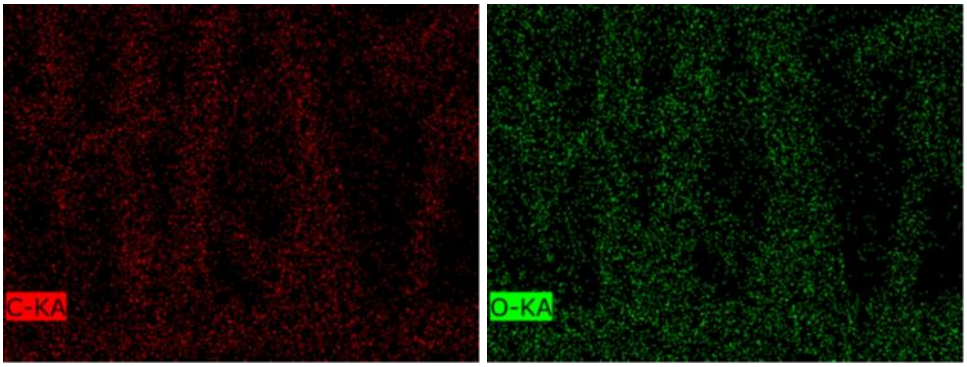

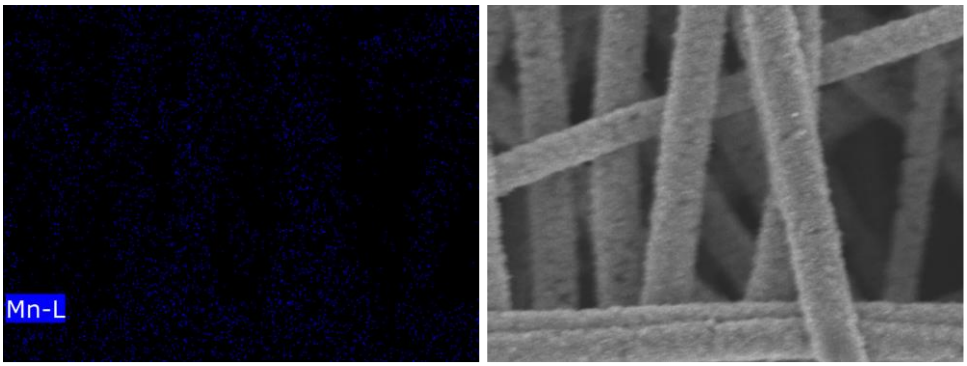

b.

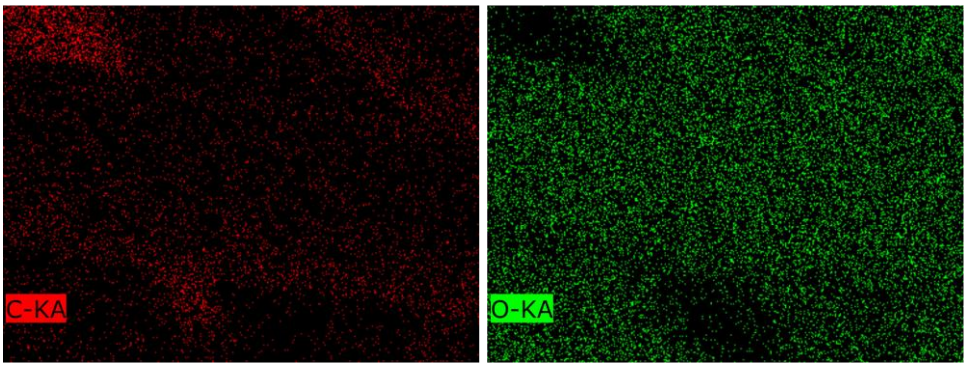

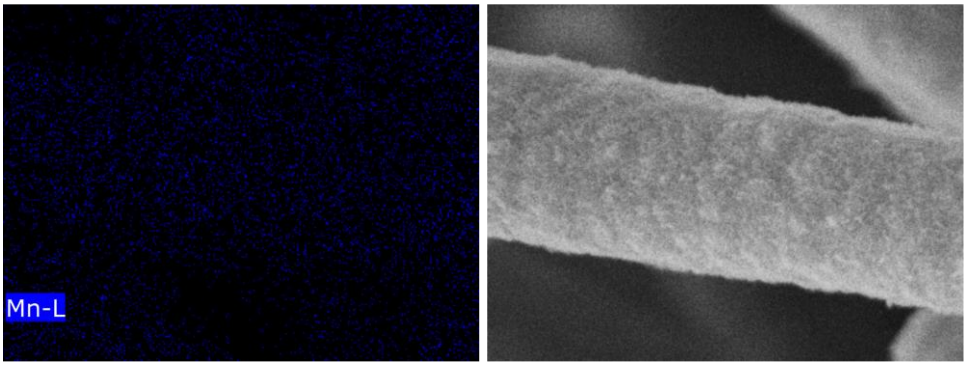

c.

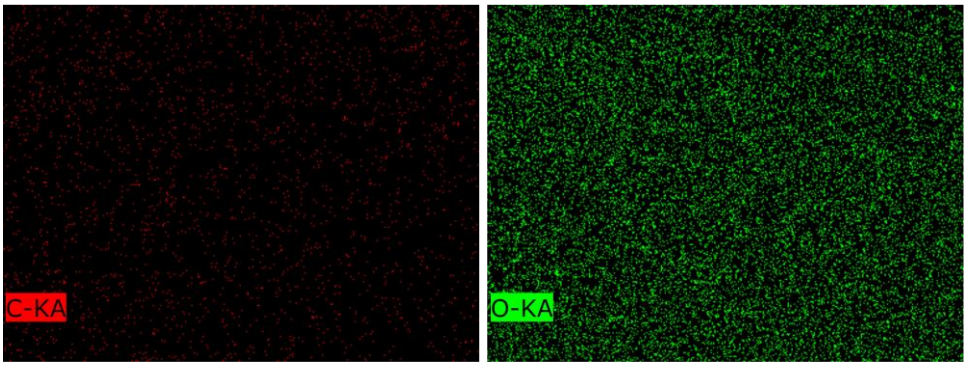

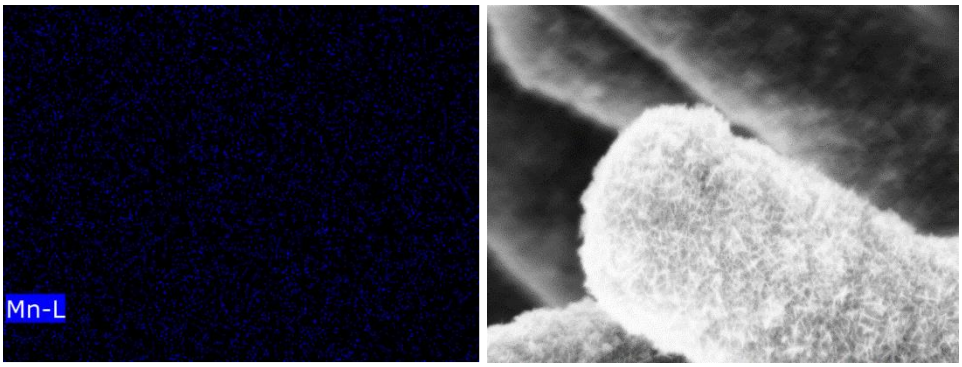

d.

Table C. S5.2. Elemental composition of the NPs from EDX data (Atomic %)

Sample	**C at. %**	**O at. %**	**Mn at. %**
SA-CNFs	98.81	1.19	-
5-MnO_2@SA-CNFs	45.10	38.81	16.09
10-MnO_2@SA-CNFs	13.42	58.58	28.00
15-MnO_2@SA-CNFs	1.85	65.99	32.16

Figure C. S5.4. (a) C1s, **(b)** O1s, and **(c)** Mn2p XPS spectrum of different samples.

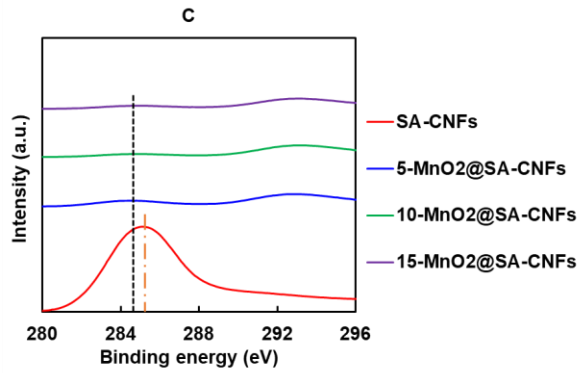

a.

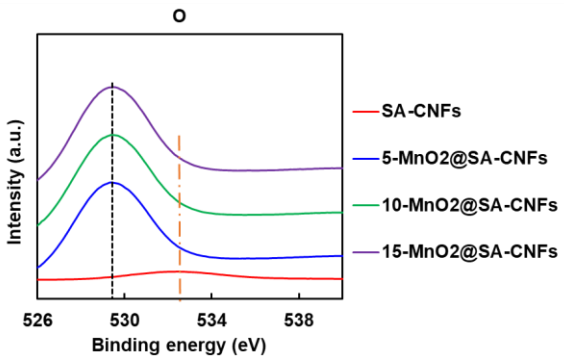

b.

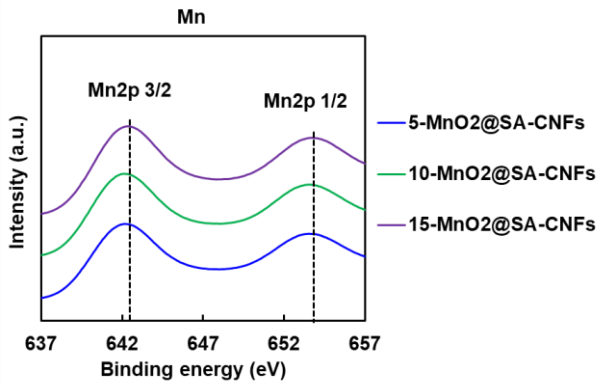

c.

Figure C. S5.5. LSV scan on the 15-MnO2@SA-CNFs without magnetic field.